Synthesis and Characterization of Physical Property of Metal Halide Perovskite ABX_3 Single Crystal as Well as the Effect of Alloyed X-site on Their Photoexcited Carrier Dynamics

Liu Dong

Doctor of Philosophy

THE UNIVERSITY OF ELECTRO-COMMUNICATIONS

GRADUATE SCHOOL OF INFORMATICS AND ENGINEERING

March 2024

Synthesis and Characterization of Physical Property of Metal Halide Perovskite ABX_3 Single Crystal as Well as the Effect of Alloyed X-site on Their Photoexcited Carrier Dynamics

THESIS FOR THE DEGREE OF DOCTOR OF PHILOSOPHY

Liu Dong

APPROVED BY THE DOCTORAL DISSERTATION REVIEW COMMITTEE:

沈　青	(Qing Shen)	教授
奥野　剛史	(Tsuyoshi Okuno)	教授
平野　誉	(Takashi Hiran)	教授
曽我部 東馬	(Tomah Sogabe)	准教授
早瀬　修二	(Shuzi Hayase)	特任教授

PhD SUPERVISOR

PROFESSOR Qing Shen

和文要旨

ハロゲン化金属ペロブスカイト ABX_3（A:有機メチルアミン($CH_3NH_3^+$ (MA^+))、ホルムアミジン($CH(NH_2)_2^+$ (FA^+))、無機セシウム(Cs^+)カチオン；B: Pb^{2+}、Sn^{2+}などの 2 価金属カチオン;X: ハロゲンアニオン(Cl-、Br-、I-)）材料は、その優れた光電子特性のため、太陽電池、光検出器、発光ダイオード（LED）に至る幅広い用途において重要な材料である。結晶粒界がなく、欠陥濃度が低い単結晶材料は、デバイス製造と基本特性研究などの方面によく使われている。一般的に、ペロブスカイトにおいて、ハロゲンを混晶することが材料の光学特性を簡単に変更できる。また、光物性、電子物性、熱特物性など、ペロブスカイトの基本物性に関する研究は、その材料の本質を解明でき、相応のデバイスの開発に対して非常に重要である。現在、X サイト混晶のペロブスカイトの基礎物性の解明はまだ不十分である。さらに、ペロブスカイト材料のキャリア拡散係数や表面再結合速度などの基本物性のパラメータを効率的かつ正確に得ることが難しいである。本論文の目的は、①光音響分光（PA）法をペロブスカイト分野における新しい評価法として提案し、ペロブスカイト単結晶の光物性、電子物性、熱物性を非破壊かつ同時に評価できることを実証すること、②典型的な臭素（Br）とヨウ素（I）を混晶したペロブスカイト単結晶における光励起キャリアダイナミクスと欠陥密度の混晶比（Br/I）の依存性及びそれらの相関性について明らかにすることである。

第 1 章では、太陽電池の背景、ペロブスカイトの優れた特性について紹介し、A、B、X サイトにおける混晶がペロブスカイト結晶構造と基本物性に与える影響を比較した。その後、単結晶の成長原理と、いくつの単結晶の作製方法、およびペロブスカイト単結晶の応用について簡単に説明した。

第 2 章では、主に論文に関連するさまざまな測定方法と装置について説明した。X 線回折測定、ロッキングカーブ、光吸収、蛍光測定（PL)、時間応答蛍光測定（TRPL)、光音響分光法（PA)、プロファイリング、空間電荷制限電流（SCLC）測定、インピーダンス測定、フラッシュ法を含めた。

第 3 章では、MAPbBr3 および MAPbI3 単結晶を研究対象として合成し、PA 法を用いて試料の基礎物性を評価した。PA 法は、光熱変換現象に基づく技術で、非破壊かつ非接触的に材料の評価が可能である。反射モードおよび透過モードの測定を通して、サンプルの光吸収、表面再結合速度、キャリア寿命、拡散係数、および熱拡散係数を同時に得た。PA 法から得られたパラメータの正しさを確かめるために、先行研究を参照し、他の方法を使用してパラメータを取得して比較した。例えば、SCLC およびアインシュタイン方程式を用いて結晶の拡散係数を計算して、インピーダンス法を用いてキャリア寿命を得て、フラッシュ法を用いて試料の熱拡散係数を直接取得した。比較により、結果は一致し、PA 法はペロブスカイト材料に適用し、基本物性を効率的かつ正確に評価

できることを確かめた。この方法が他のペロブスカイト材料の評価に使用され、相応の基礎データを提供することを期待している。

第 4 章では、I をドーピングした $MAPb(Br_{1-x}I_x)_3$ ペロブスカイト単結晶を合成し、PL と TRPL 測定法を用いてその光励起キャリアダイナミクスを研究した。励起光強度依存の PL 測定により、結晶の中、フリーキャリア再結合過程を明確した。その後、TRPL と関連の測定を通して、ヨウ素ドーピングにより PL の緩和過程が初めは速くなり、その後遅くなり、最終的に再び速くなること現象が観測された。この原因は浅いトラップ状態によって引き起こされる電子の detrap プロセスだと考えられる。上述の現象と一致しないのは、結晶の PL 有効寿命がヨウ素のドーピングによって最初短くなるが、さらなるドーピングすると徐々に長くなることが観察された。これは電荷トラップアシスト再結合の影響によるものと考えられる。シミュレーションから、電子の monomolecular recombination 係数の変化が上述の有効寿命の変化と一致し、bimolecular recombination 係数の変化が先に述べた PL kinetics の変化と対応することが判明した。この結果は PL kinetics の変化についての解釈を確かめた。最終的に、少量のヨウ素ドーピングはトラップ状態を顕著に増加させるが、継続的なドーピングによりこれらのトラップ状態が徐々に減少すると結論を出した。これらの結果はハロゲン混晶のペロブスカイト材料の理解を深め、実用化への指針を与えた。

第 5 章では、この論文の結論をまとめて、ペロブスカイト単結晶の将来の展望について述べた。

Abstract

Perovskite materials show great potential for applications in field such as solar cells, photodetectors, light-emitting diodes (LED), due to their excellent optoelectronic properties. Single crystal materials, with their absence of grain boundaries and lower defect concentrations, are providing a platform of device fabrication and fundamental properties research. It is well known that in the basic structure of perovskites ABX_3, the mixing or substitution of halogens at the X site is often used as a method to change the optical properties of the material. Meanwhile, fundamental research into the basic physical properties of perovskites, such as optical, electronic, and thermal properties, is very important as it guides the development of perovskite-based devices. Currently, research on the intrinsic properties of mixed-halide perovskite is still lacking. Moreover, the existing measurement techniques are not efficient and accurate in obtaining some intrinsic parameters of perovskite material, such as carrier diffusion constant and surface recombination velocity. In our thesis, we first introduce a new measurement method in the field of perovskites, the photoacoustic (PA) technique. This method allows for non-destructive and simultaneous characterization of the optical, electrical, and thermal properties of the sample. Subsequently, we focus on the photoexcited carrier dynamics of mixed-halide perovskites.

Chapter 1 introduces the background of solar cells, the outstanding properties of perovskites, and compares the effects of doping or substituting at the A, B, and X sites on the perovskite crystal structure and physical properties. Subsequently, we briefly explain the nucleation principles of single crystals and some common-used methods for growing single crystals, as well as the applications of perovskite single crystals.

Chapter 2 primarily discusses various characterization and instruments related to the thesis. These include X-ray diffraction, X-ray rocking curves, optical absorption, PL, and time-resolved PL. Afterward, we provide a detailed description of the PA technique used in Work 1. We also

introduce the profilometer, Space Charge Limited Current (SCLC) measurements, impedance measurement, and the Flash method.

In **Chapter 3**, based on the previous discussion, we synthesized typical $MAPbBr_3$ and $MAPbI_3$ single crystals as research subjects and characterized them using the PA technique. The PA method is a technique based on photothermal conversion that allows for non-destructive, non-contact characterization. Through measurements with the PA reflection and transmission modes, we obtained the optical absorption curves of the samples, as well as the surface recombination velocity, carrier lifetime, diffusion coefficient, and thermal diffusion coefficient simultaneously. To verify the accuracy of the parameters obtained from the PA technique, on one hand, we referred to previous literatures, and on the other hand, we used other methods to obtain corresponding parameters for comparison. For instance, we employed Space-Charge Limited Current (SCLC) and the Einstein equation to calculate the diffusion coefficient of the crystal, used the impedance method to achieve the carrier lifetime, and applied the Flash method to directly obtain the thermal diffusion coefficient of the sample. By comparison, we can conclude that the Photoacoustic (PA) method can be well applied in perovskite materials and can effectively and accurately obtain these parameters. We are looking forward to this method being used for the characterization of other perovskite materials and providing corresponding fundamental data for them.

In **Chapter 4**, We synthesized iodine-doping $MAPb(Br_{1-x}I_x)_3$ perovskite single crystals and studied their carrier recombination dynamics utilizing steady-state PL and the time-resolved PL technique. We ascertained that in our crystals, free carrier recombination is the prevailing process, as indicated by excitation intensity-dependent PL measurements. Following, through TRPL and related measurements, we found that the PL kinetics became rapid, then slowed down, and finally get rapid again with the iodine doping, which can be attributed to the electron detrap process induced by shallow trap states. Interestingly, we have also observed that the PL effective lifetime

of the crystal get shorter when iodine is introduced, but gradually becomes longer with further doping, which is attributed to the impact of trap-assisted recombination. According to the numerical simulations, we found that the changes in the electron monomolecular recombination coefficient match the changes in the effective lifetime mentioned above, while the changes in the bimolecular recombination coefficient correspond with the changes in the PL kinetics described earlier. This to some extent substantiates our viewpoint. Eventually, we concluded that a few iodine doping leads to a significant increase in trap states, while continued doping results in a gradual decrease of these trap states. Our results have deepened the understanding of mixed-halide perovskite materials and provided guidance for their practical applications.

Chapter 5 offers a summary of this thesis and presents the future outlook for the development of perovskite single crystals.

Table of Contents

Chapter 1. Introduction

1.1 Energy development

Global warming refers to the rise in atmospheric or oceanic temperatures over a period of time. The increased temperatures have adverse effects on the Earth's climate, such as intense storms or extreme weather. Human activities are considered the primary cause of global warming, and greenhouse gases released into the environment, such as carbon dioxide (CO_2) and methane

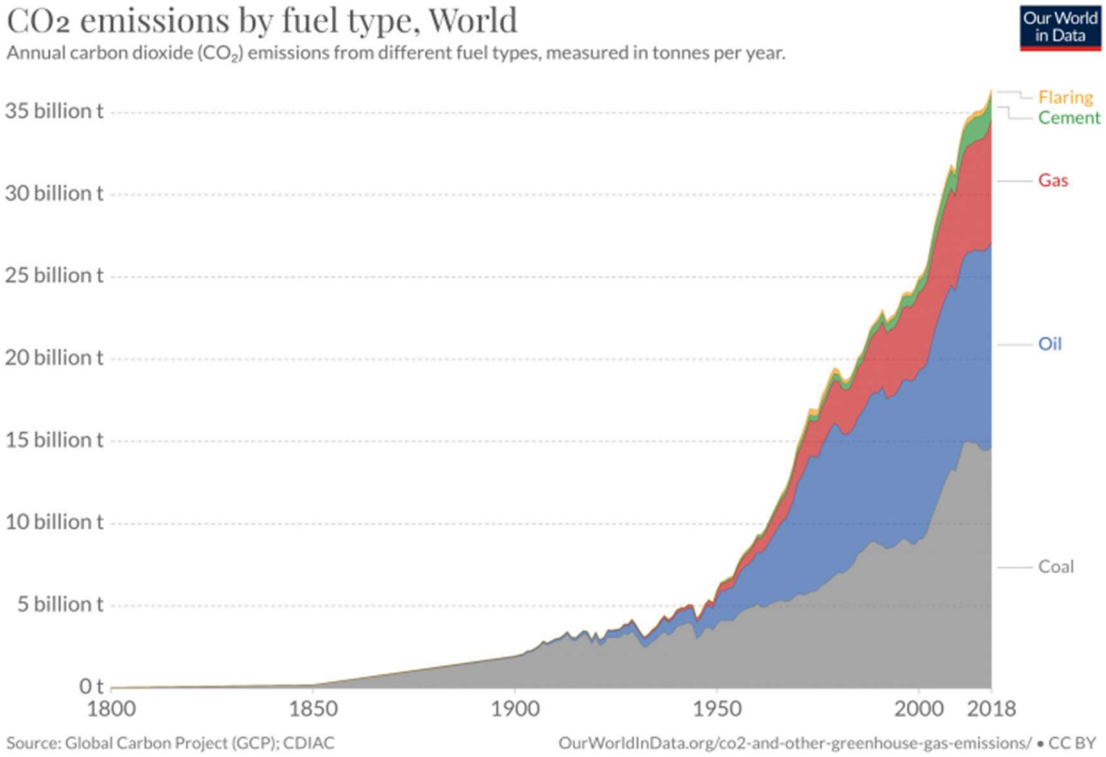

Figure1-1. CO_2 emissions by fuel type in world from 1800 to 2018 [1].

(CH_4), are the major drivers of rising temperatures. Fig.1-1 shows the evolution of CO_2 emissions from fossil fuels from 1800 to 2018 [1], which indicated that burning traditional fossil fuels generates significant emissions of carbon dioxide, thereby impacting the global climate. However, with the increasing population, the demand for and consumption of energy have become

more extreme. Fossil fuels are also gradually falling short in supply, despite the usage of which will intense the environmental burden. Thus, people are eager for the development of new energy sources. So far, energy can be divided into two categories: renewable energy and non-renewable energy sources. Non-renewable energy sources include the aforementioned fossil fuels such as coal, natural gas, oil, and nuclear power. Renewable energy sources include the solar energy, geothermal energy, wind energy and so on. Among them, solar energy, as one of the most abundant energy sources, has attracted widespread attention. When discussing the efficient utilization of solar energy, solar cells are often mentioned. Solar cells can directly convert solar energy into electricity for immediately use or storage.

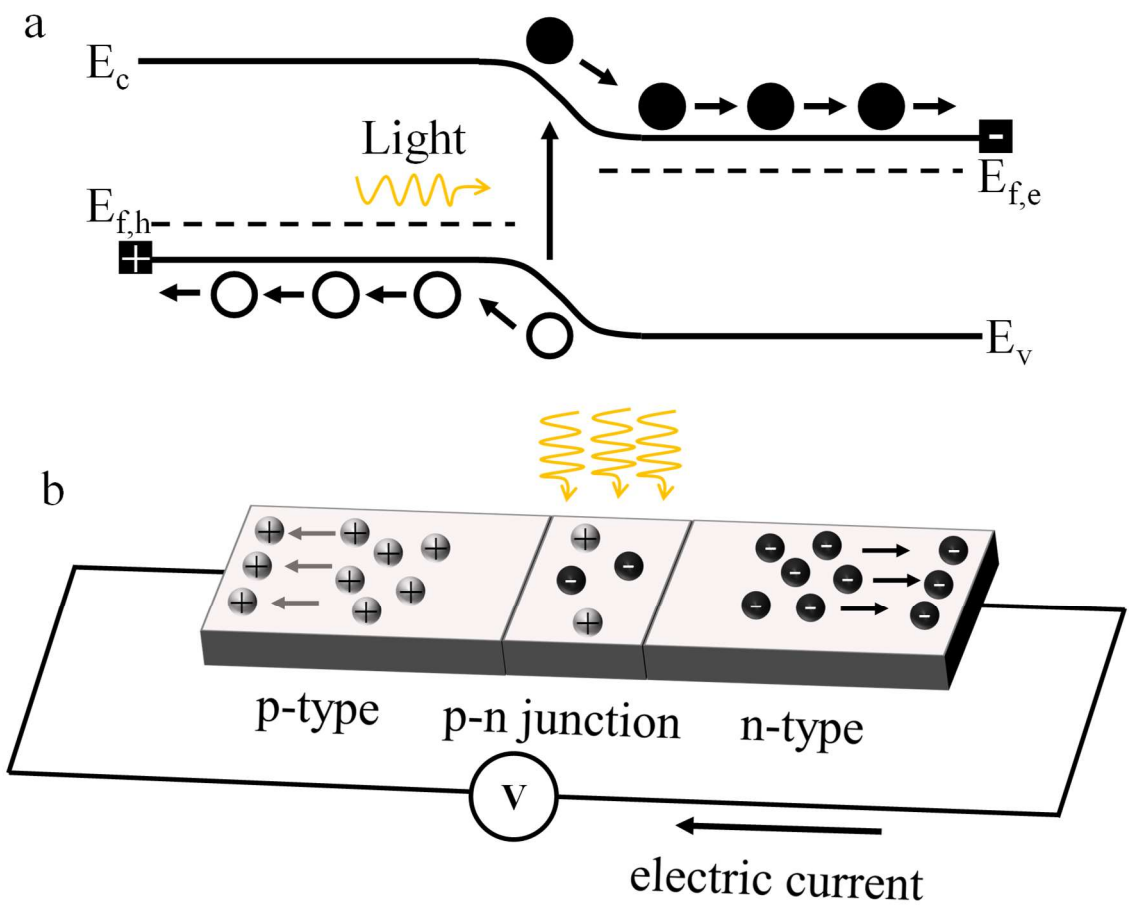

Figure 1-2. (a) Charge carrier separation in a p-n junction; (b) Schematic diagram of p-n junction solar cell.

1.2 Types of solar cells

The process of photovoltaic conversion in solar cells include absorption of the sunlight to generate the photoexcited electron-hole pairs, and charge carrier separation process. Thus, the way to efficiently absorb sunlight and convert it into charge carriers, as well as the separation of charge carriers, has become a critical issue in improving the performance of solar cells. In common, a p-n junction is used to deal with the charge carrier separation [2]. Fig.1-2a illustrates the schematic diagram of charge carrier separation in p-n junction. In Fig.1-2b, the typical structure of p-n junction solar cell has been shown. Further, the selection of material for absorption layer in solar cell is quite important. As is well known, in most cases, semiconductor materials are utilized as absorption layer due to their special electrical properties. To date, solar cells have undergone multiple innovations. Initially, solar cells were primarily produced using silicon material as the base, including monocrystalline silicon, polycrystalline silicon, and amorphous silicon solar cells. Among them, monocrystalline silicon solar cells have a high photovoltaic conversion efficiency, but due to material and manufacturing complexity, their produce cost is relatively high. On the contrary, while polycrystalline silicon and amorphous silicon have lower costs compared to monocrystalline silicon, their photovoltaic conversion efficiency is not as high as that of monocrystalline silicon solar cells. With the advancement of research, attention has been increasingly focused on thin film solar cells due to their lower cost and the advantage of being able to be manufactured on a large scale. Therefore, thin film solar cells are also referred to as second-generation solar cells, including cadmium telluride (CdTe), gallium arsenide (GaAs), copper indium gallium selenide (CIGS), and various other thin-film solar cells. However, these solar cells also have their respective drawbacks. For example, cadmium-containing cells like CdTe, despite their high photovoltaic conversion efficiency and relatively low cost, have detrimental effects on natural environment due to the toxicity of cadmium. GaAs cells indeed

have very high photovoltaic efficiency and are known for their radiation resistance and thermal stability, making them suitable for various aerospace applications. However, their high cost is a significant drawback. Due to the reasons mentioned above, people are still exploring new types of solar cells. To date, multi-junction techniques to enhance light absorption and methods for extracting hot carriers are both employed in the development of third-generation solar cells. Some new materials are also being applied as light-absorbing layers in solar cells such as some organic materials and perovskite materials. Among them, perovskite materials have been attracted significant attention from many researchers due to their excellent optoelectronic properties. So far, the power conversion efficiency (PCE) of perovskite-based single junction solar cell have been achieved over 26%, as shown in Fig.1-3 [3].

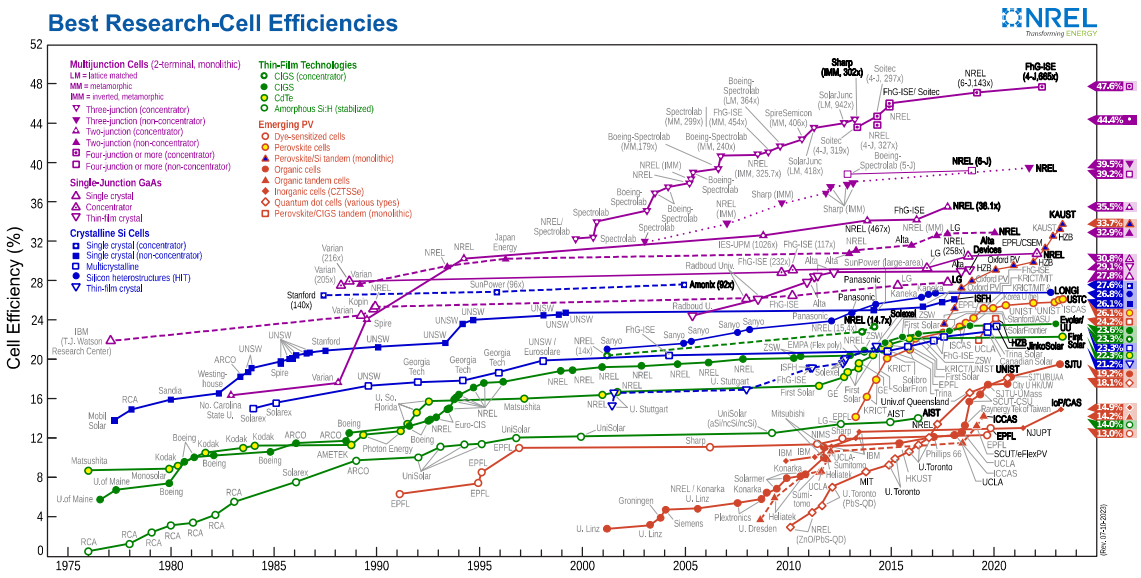

Figure 1-3. Best research cell efficiencies produced by National Renewable Energy Laboratory [3].

1.3 Perovskite

Perovskite refers to the compound of calcium titanium oxide mineral ($CaTiO_3$), named after the Russian scientist Lev Perovski. Currently, in a general sense, the class of compounds possessing this crystal structure are referred to as perovskite materials. The crystal structure of

perovskite is generally represented as ABX_3, where A is cation (MA^+ (methylamine), FA^+ (formamidine), Cs^+), B is metal cation (Pb^{2+}, Sn^{2+}) and X site is the halogen ions (Cl^-, Br^-, I^-). It can be seen that the stacking arrangement of BX_6 octahedra includes the A-site cations, forming the perovskite structure. There are many factors that can affect the stability of this structure, and the crystal-structure transitions is an important one [4]. Tolerance factor (t) and octahedral factor (δ) are important parameters for evaluating the crystal structure of perovskites [5]. According to,

$$t = \frac{r_A + r_X}{\sqrt{2}(r_B + r_X)} \quad (1-1)$$

$$\delta = \frac{r_B}{r_X} \quad (1-2)$$

where r_A, r_B, r_X represents the radius of the A-site cation, metal cation, and halogen anion, respectively. Generally, materials with a tolerance factor of 0.9−1.0 lead to an ideal cubic structure. A tolerance factor ranging from 0.71 to 0.9 results in a perovskite structure that is distorted with tilted octahedra. Non-perovskite structures are formed when the tolerance factor exceeds over 1 or falls below 0.71 [6]. The octahedral factor is utilized to ascertain whether the B-site has the appropriate size to accommodate the X_6 octahedron. The stable 3D perovskite structure should have an octahedral factor value falling within the range of 0.442 to 0.895 [7].

1.4 Composition engineering for perovskite

Modifying the composition or introducing component doping into perovskite materials can be an effective approach to tailor the properties of perovskite [8]. For a specific photovoltaic device, it is necessary to adjust the composition at various positions to meet the desired requirements. As a typical ionic semiconductor material, in perovskites, components at the A, B, and X sites can all be modified as long as requirements such as the stability of the perovskite structure and the charge balance are maintained [9]. Next, we will explain the effects of composition engineering at different positions in ABX_3 on perovskite materials.

1.4.1 A-site alloyed perovskite

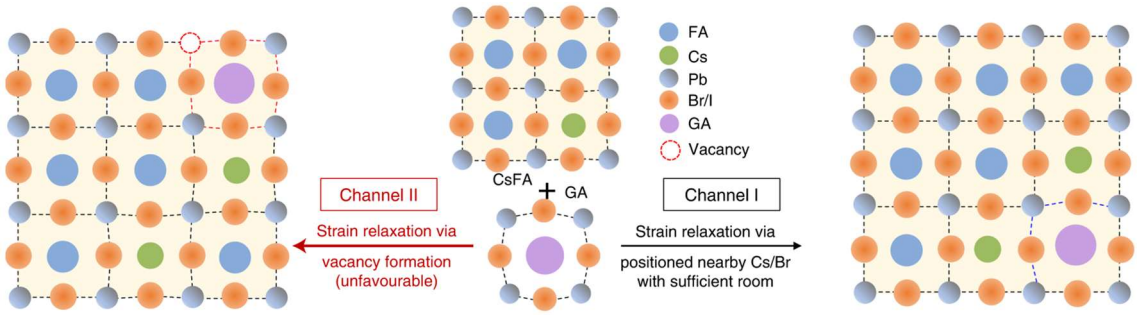

Figure 1-4. Diagram illustrating the local tensile strain in CsFAGA crystal, which can be relieved either through compensation with compressive strain (Channel I) or by the creation of point defects (Channel II) [14]

The commonly used A-site components include FA^+, MA^+, and Cs^+, and they also decrease in size in the mentioned order. The A-site components do not directly affect the overall electronic structure of the material, the influence on optical properties, such as the bandgap, is relatively small. But they still influence the lattice symmetry of perovskite. For example, replacing the MA^+ with FA^+ in the tetragonal lattice of $MAPbI_3$ can lead to a cubic perovskite structure. Each single ion composition has its own advantages in fabrication of device, while each single ion composition also has its own drawbacks. For instance, $MAPbI_3$ experiences a structural phase transition at 54~60 °C [10, 11], as well as the formation of defects and trap states induced by light. Both $FAPbI_3$ and $CsPbI_3$ generate a yellow δ phase at room temperature [12, 13], which possesses poor symmetry. Composition engineering is a well-known approach for addressing structural stability. And it has applications in many cases. In the field of X-ray detectors, due to the lack of long-term reliability in commonly used high-performance devices based on $MAPbI_3$, researchers have developed the Cs-FA alloy system [14, 15]. Furthermore, currently, some studies choose the triple cation system to achieve better fine-tuning of phase formations in perovskite solar cells [16, 17]. In addition to the commonly mentioned A-site components, A-sites can also be doped with cations such as ethylammonium (EA) [18, 19], guanidinium (GA) [20, 21], or dimethylammonium (DMA) [22, 23]. However, the introduction of new doping can also bring about additional challenges. As

Fig.1-4 shows, the doping of GA can make the original Cs-FA system more stable, but the presence of larger-sized GA ions can lead to inhomogeneous stress in the lattice [14]. It has also been reported that in $MAPbBr_3$ single crystals when doping with a small amount of DMA ions, the rapid reorientation of the included DMA cations enhances the interaction between MA cations and the lattice without causing substantial lattice distortion. This, in turn, can dampen lattice fluctuations and consequently enhance photovoltaic performance. However, conversely, a high concentration of doping can lead to severe lattice distortion [24]. The advantages and disadvantages of these A-site dopants can significantly impact the performance of their photovoltaic devices. Studying the mechanisms behind these effects, finding optimal solutions, and balancing these influences will provide significant support for the development of perovskite materials.

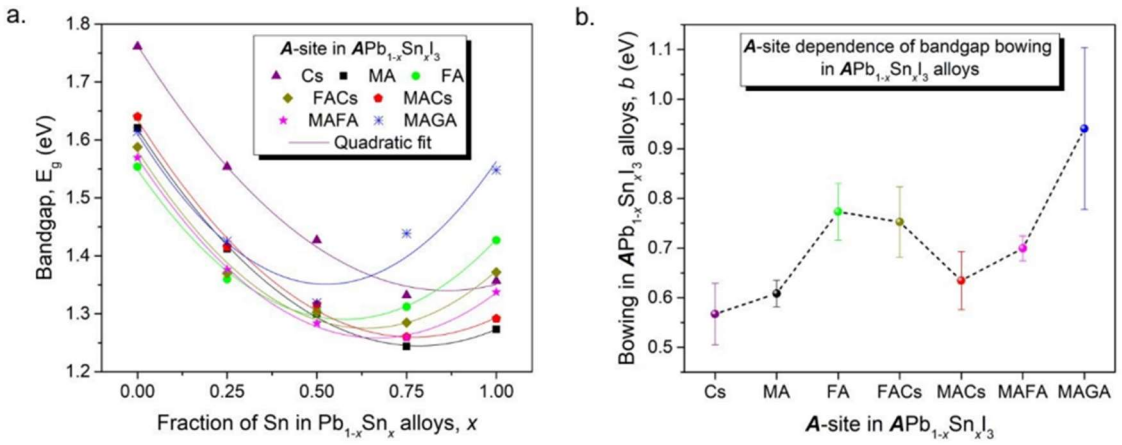

Figure 1-5. (a) Bandgap variation in $APb_{1-x}Sn_xI_3$ alloy compositions ($0 \leq x \leq 1$), (b) A-site dependence of bandgap bowing in $APb_{1-x}Sn_xI_3$ alloys [43].

1.4.2 B-site alloyed perovskite

So far, lead remains the most commonly used B-site material in perovskites. However, due to its toxicity, the widespread use of perovskites has been hindered. Currently, various encapsulation methods have been investigated to inhibit the release of lead from Pb-based solar cells, including capturing lead through functionalized metal-organic frameworks or cation-

exchange resins [25] and Isolating lead by applying a layer of material that absorbs Pb [26]. However, these endeavors have not fundamentally resolved the concerns regarding the toxicity of lead. Therefore, the search for suitable B-site materials other than lead has always been an important topic of research. For this topic, many researchers have proposed solutions, such as the use of metal ions like tin (Sn^{2+}), germanium (Ge^{2+}), manganese (Mn^{2+}), calcium (Ca^{2+}), or rare metals like cerium (Ce^{3+}), terbium (Tb^{3+}), ytterbium (Yb^{3+}) alternatives to lead in the B-site position.

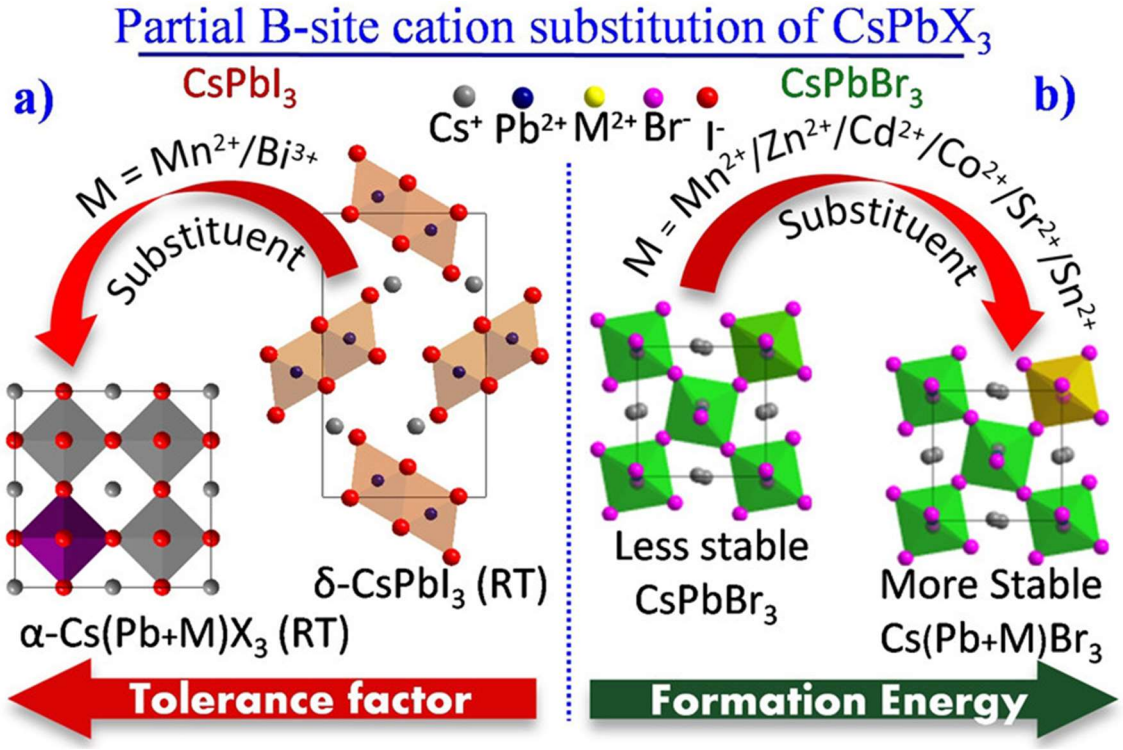

Figure 1-6. Schematic diagram illustrating the partial substitution of Pb^{2+} with different metal ions, which can result in (a) enhancing the stability of α-$CsPbI_3$ at room temperature by raising the tolerance factor and (b) enhancing the thermal stability of orthorhombic $CsPbBr_3$ by increasing the formation energy [48].

Sn and Pb are neighboring elements in the same main group (IVA) on the periodic table, and they share a similar outermost electron configuration and ionic radius. Thus, Sn^{2+} has received a significant amount of attention as an alternative to lead. However, in tin-based perovskites, the notorious oxidation process of tin greatly hinders the development of tin-based perovskites. Sn^{2+} is highly susceptible to oxidation, leading to its transformation into the Sn^{4+} state [27, 28]. This

process significantly deteriorates the tin-based film due to the formation of vacancy-type structures [29]. To address this issue, the direct approach is to incorporate a reducing agent into perovskite precursor. SnF_2 [30, 31], hydroquinones [32, 33], and hydrazine-type compounds (e.g., hydrazine, [28] phenylhydrazine hydrochloride (PHCl) [34]) containing N-NH functional groups have been demonstrated to possess the capability to either inhibit the oxidation of Sn^{2+} or convert Sn^{4+} back into Sn^{2+}. Except the oxidation issue, in Sn-based perovskites, during the nucleation and growth process, the higher Lewis acidity of Sn^{2+} compared to Pb^{2+} leads to excessively rapid crystallization [35]. And the rapid crystallization process leads to a rougher film with many deep level trap states introduced. Therefore, producing high-quality and stable tin-based perovskite still need extensive research. Despite these challenges associated with tin, it still remains a crucial material in the B-site, because it can further narrow the bandgap of perovskites. As mentioned in our introduction to the A-site, changes or alloying at the A-site have a relatively minor impact on the electronic structure of the perovskite material. In perovskite materials, the conduction band minimum (CBM) and valence band maximum (VBM) are primarily composed of B-site metal ions and X-site halide ions. For example, the VBM of $MASnI_3$ primarily consists of the antibonding interactions between Sn 5s and I 5p orbitals, with the main contribution coming from the I 5p orbitals. On the other hand, the CBM is mainly influenced by the Sn 5p orbitals [35, 36]. Therefore, replacing or alloying B-site metal ions can have a significant impact on the overall electronic structure of the material. As far as we know, the optical bandgap of tin-based perovskites is approximately in the range of 1.2 eV to 1.4 eV [37], which is very close to the optimal bandgap 1.34eV for the Shockley–Queisser (SQ) limit under the condition of AM 1.5 solar spectrum [38]. Although the addition of tin components can reduce the bandgap, it doesn't decrease linearly. Instead, it forms a curve as the Sn content increases. And this phenomenon is not limited to a specific A-site cation, it occurs with MA, FA, Cs, or their alloys (FAMA, FACs) as well [39-42].

This non-linear and odd characteristic is also referred to as the bowing effect, as shown in Fig.1-5 [43]. The bandgap after alloying can be described using the following formula:

$$E_g(A_{1-x}B_x) = (1-x)E_g(A) + xE_g(B) + b(x)(1-x) \qquad (1-3)$$

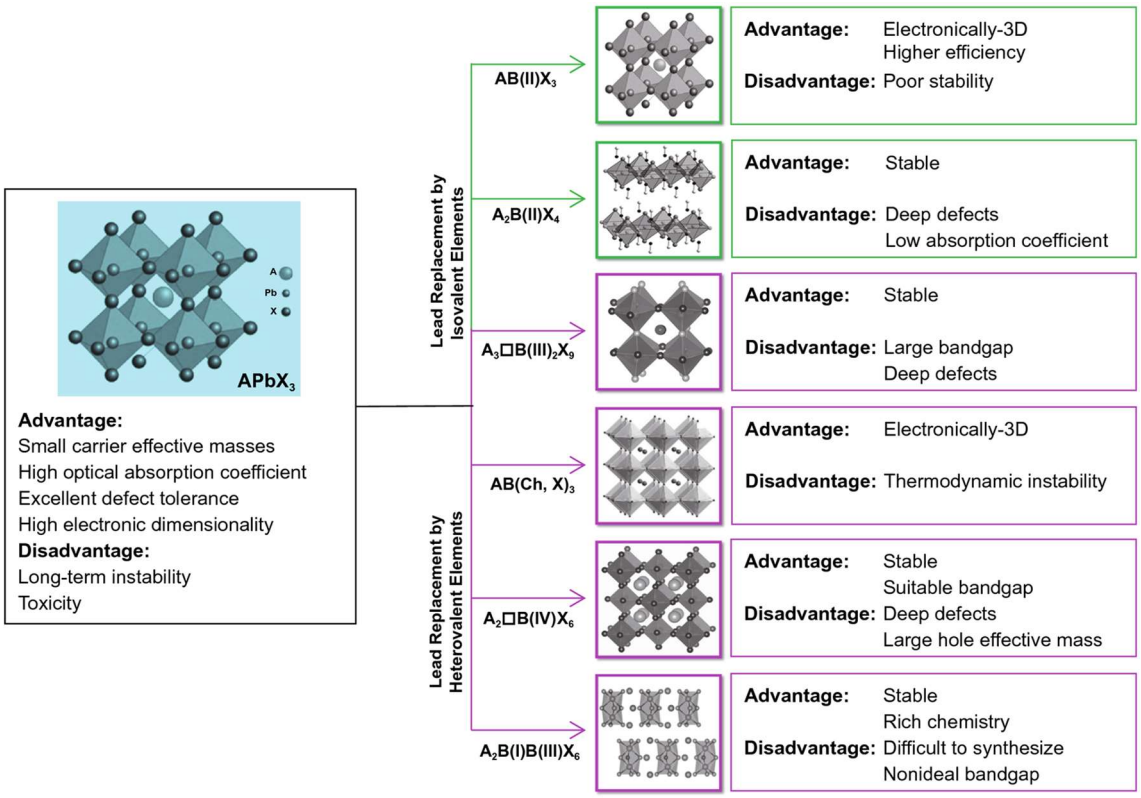

Figure 1-7. Schematic illustration of the methods and consequences of possible substitution for Pb [53].

where, b is the bowing parameter, which assess the magnitude of the non-linear component. Several explanations were proposed to understand the underlying mechanism of bowing effect. Khatun et al. suggested that gap bowing results from a combination of composition-induced alterations in spin-orbit coupling (SOC) and structural distortion [44]. Nonetheless, according to more comprehensive first-principles calculations, several studies excluded the involvement of SOC [40, 45]. Eperon et al. proposed that the primary source of the bowing is the short-range arrangement of Sn/Pb atoms [40]. Conversely, Goyal et al. contended that the bowing primarily results from a chemical mismatch between Sn and Pb, with negligible structural impact [45]. Valadares et al. determined that the configuration of atomic orbitals plays a crucial role in this

issue [46]. Rajagopal et al. stated that local structural relaxation (SR) effects are accountable for the bowing effect [43]. In conclusion, the origin of the bowing effect is not yet fully understood [47]. Apart

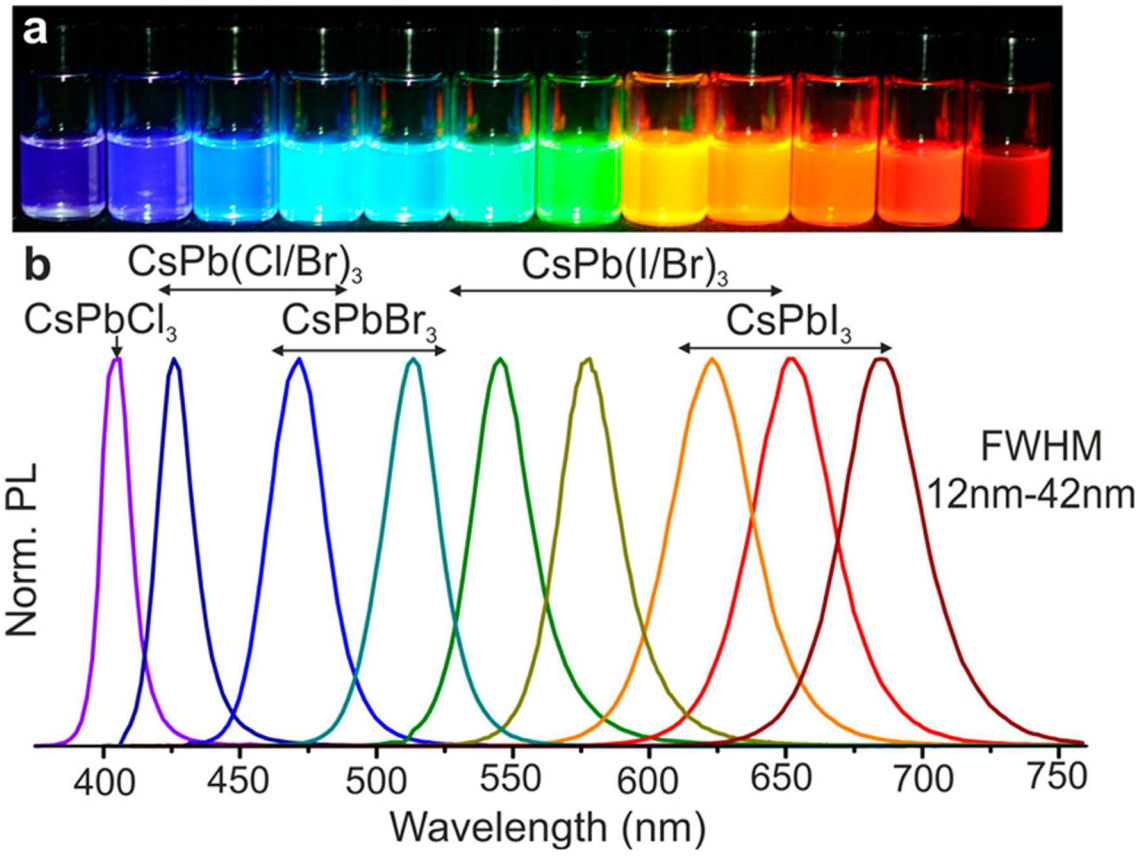

Figure 1-8(a). colloidal solutions of $CsPbX_3$ nanocrystals (X = Cl, Br, I) in toluene under UV lamp, (b). representative Photoluminescence spectra of these samples [54].

from tuning the bandgap, partial substitution of Pb^{2+} with other metal ions can also serve to adjust the lattice structure and enhance stability [48]. As shown in Fig.1-6(a), partial B-site metal ions substitution of $CsPbI_3$ can help improve the lattice stability by increasing the structural tolerance factor. In Fig.1-6(b), it can enhance the thermal stability of $CsPbBr_3$ by increasing the formation energy. Due to its excellent optical properties, tin-based perovskites are also shining as absorbers in solar cells. The initial demonstration of tin-halide perovskite solar cells occurred in 2014, with Hao et al. and Noel et al. reporting power conversion efficiencies (PCE) of 5.7% and 6.4%, respectively, using methylammonium tin halides as the absorber layers [49, 50]. Currently, the highest-performing tin-halide perovskite solar cells have achieved PCEs exceeding 14%. Yu et al.

documented 2D/3D perovskite solar cells with a certified efficiency of 14.03% [51], while Jiang et al. achieved a certified PCE of 14.6% through an innovative film fabrication approach using SnI_2 adducts [52]. In addition to tin, as mentioned earlier, researchers have also developed numerous alternative materials on B-site. Fig.1-7 summarized the methods and consequences of possible substitution for Pb, and explain their advantages and disadvantages [53]. In summary, the B-site is a position that influences the overall electronic structure of perovskite materials. While most devices traditionally use lead as their common material, research on non-lead materials or alloy materials is also crucial.

1.4.3 X-site alloyed perovskite

Modifying the X-site ions in perovskite materials is an effective approach to adjust the bandgap and control the conduction properties. In general, people use the method of alloying with halide ions to adjust the bandgap of perovskite materials to satisfy the requirements. The halide ions at the X-site include Cl^-, Br^-, and I^-, and in this order, the bandgap becomes progressively smaller. As shown in Fig.1-8, colloidal perovskite $CsPbX_3$ nanocrystals (X = Cl, Br, I) present composition-dependent tunable bandgap within entire visible spectrum and bright emissions [54]. Due to the wide bandgap of Cl-based perovskites, their absorption spectra typically extend only into the ultraviolet (UV) range, making them well-suited for use as Ultraviolet detectors [55]. On the contrary, I-based perovskites have a smaller bandgap and a broader absorption spectrum, making them suitable as the light-absorbing layer in solar cells [56]. The initial perovskite-based solar cell that utilized $CH_3NH_3PbI_3$ achieved an efficiency of 3.81% in 2009 [57], which is rapidly escalated to a validated peak PCE of 26.1% [3]. Lee, Michael M. et al. successfully fabricated the first perovskite solar cell with mixed halide composition of $MAPbI_2Cl$, achieving an efficiency of 10.9% [58], which demonstrated that the chloride incorporation is beneficial for enhancing the device's performance. The accumulative efforts led to the demonstration that the chloride doping

played a pivotal role in shaping the morphology and crystallinity of the polycrystalline perovskite, consequently enhancing the performance of the photovoltaic applications [59, 60]. This conclusion also can apply for single-crystal materials. Lian, Zhipeng, et al. studied $MAPbI_3(Cl)$ single crystals and found that the chloride additive could shorten the growth period of single crystals and result in higher-quality crystals with fewer trap state density [61]. Mixed halide strategy marked a significant breakthrough, and following this, perovskite solar cells and other photovoltaic devices have mostly adopted the use of mixed halide structures to enhance their performance. Not only the mixed halide strategy used in the aforementioned single-junction cells, but it also finds significant applications in multi-junction devices. In general, perovskites that combine organic and inorganic components with mixed halides, particularly those with a bandgap (E_g) exceeding 1.65 eV, are classified as wide-bandgap (WBG) perovskites. When contrasted with perovskites possessing narrower bandgaps, WBG perovskites show significant promise in various photovoltaic applications. Multi-junction photovoltaic devices serve as the stage for the application of these materials. WBG perovskite solar cells (PSCs) are the favored choice as the top cells in perovskite-on-silicon and perovskite-on-perovskite tandem solar cells. These tandem devices surpass the efficiency limits of single-junction cells, reaching approximately 33%, and push the theoretical PCE even higher, up to approximately 46% [62]. To achieve current matching between both junctions, the top cell material needs to have a bandgap of approximately 1.75 eV, considering the crystalline silicon bandgap of 1.1 eV [63]. Typically, adding bromine to iodine-based perovskites allows for the adjustment of the bandgap to create suitable top cells. However, the bromine-iodine system in perovskites is prone to severe photo-induced phase separation, which can result in a loss of open-circuit voltage and impact its applications [64]. Many researchers have conducted extensive studies on the emergence, variations, and solutions to this phenomenon.

Further details will be mentioned later chapter. Furthermore, the oxidation of halide iodine ion is another significant factor affecting its performance due to its lower oxidation potential (0.53V) [65].

So far, we have discussed the advantages and applications of single ions or alloy materials at the A, B, and X sites. Next, we will approach the description and explanation of various forms of perovskite materials from a different perspective.

1.5 Perovskite materials with different forms

Perovskite materials can be synthesized in different forms, such as nanocrystalline [66], bulk [67], thin films [68], nanowires [69], nanotubes [70], nanocubes [71], nanorods [72], and so on, depending on their intended applications. We know that perovskite materials exhibit high photoluminescence quantum yield (PLQY) and adjustable emission spectra from visible to near-infrared, among other characteristics [73]. However, the low exciton binding energy in bulk (3D) perovskites results in more straightforward exciton dissociation, which constrains their radiative recombination [74]. Hence, perovskite polycrystalline thin films with reduced grain size have been employed to confine excitons spatially and enhance the rate of radiative recombination. In the case of conventional semiconductors, efforts have been made to reduce grain size and confine excitons, leading to the emergence and development of quantum dot materials, which are materials with close-to-zero dimensions, including PbS, ZnS, CdS, and CdSe [75, 76]. Similarly, perovskites can also be fabricated into quantum dot materials, which exhibit a narrow full-width at half-maximum (FWHM) of photoluminescence at around 10 nm and a high PL quantum yield (PLQY) of approximately 80% [77, 78]. These properties are a result of their quantum confinement effect, allowing for both high color purity and brightness, which have significant potential for application in light-emitting diodes (LED). In addition to the common zero-dimensional quantum dots, nanocrystal materials also include one-dimensional structures like nanotubes, nanorods, and nanowires, as well as two-dimensional structures like nanoplates and nanosheets [79]. These

nanocrystals have important applications in optoelectronic devices. Regarding the bulk materials, this is currently the most widely used form of material. The combination of excellent optoelectronic properties and ease of fabrication has made the preparation of high-quality thin-film optoelectronic devices an essential component in the field of organic-inorganic electronics [80]. In both device applications and scientific research, it is crucial to precisely fabricate these films to fulfill the particular requirements of a given device type and structure. Additionally, this ensures the precision and quality of measurements related to microstructure-sensitive physical properties, like carrier mobility. In summary, the deposition method of perovskite thin films is of utmost importance. The deposition methods for halide-perovskite thin films are commonly categorized into two main approaches: one-step, in which all the precursors are deposited simultaneously onto the substrate, or two-step, where each precursor is deposited separately or sequentially onto the

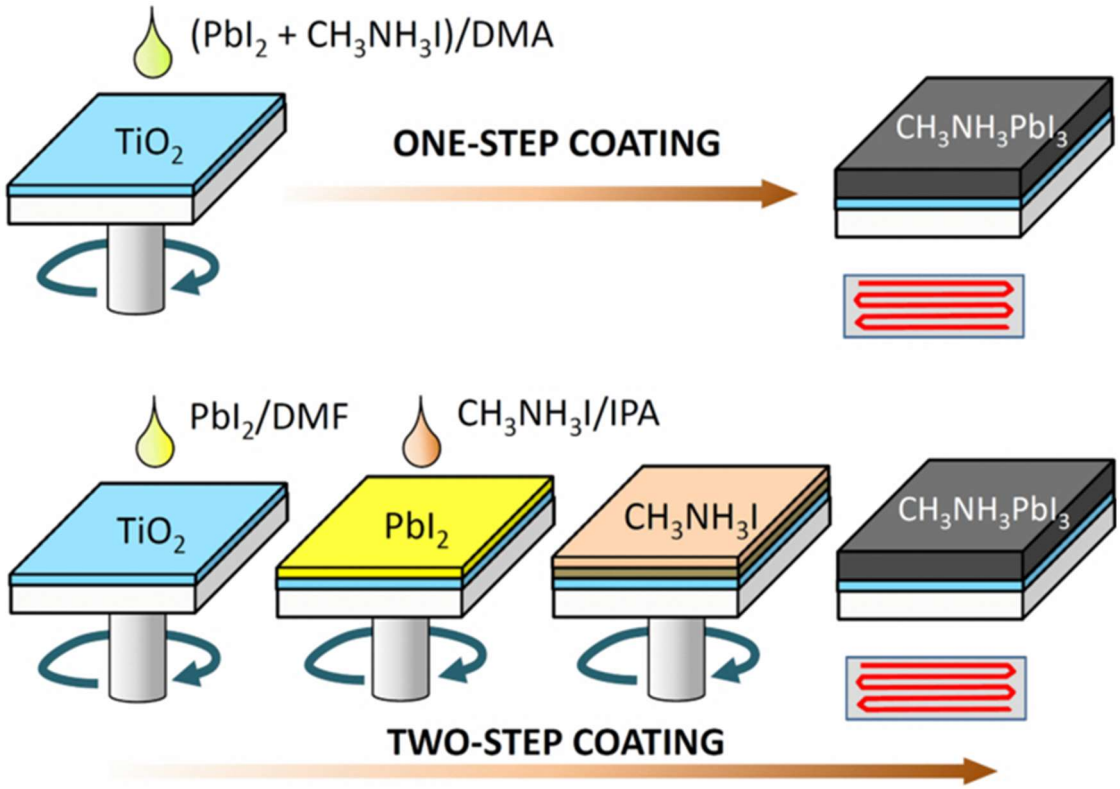

Figure 1-9. Spin-coating procedures for $CH_3NH_3PbI_3$ formation in one-step and two-step methods [81].

substrate. Next, we will briefly introduce the specific procedures for one-step and two-step methods. As shown in Fig.1-9, whether it's a one-step or two-step process, spin-coating is the most fundamental method for film deposition [81]. In a one-step method, for example, you would need to dissolve CH_3NH_3I and PbI_2 in a polar solvent (dimethylformamide (DMF), dimethyl sulfoxide (DMSO), gamma-butyrolactone (GBL), N-methyl-2-pyrrolidone (NMP)) or a mixture of polar solvents. Then, the dissolved precursor solution is dropped onto a prepared substrate. In a vacuum environment, as the substrate rotates, the solution gradually spreads and is flung out. As the solvent evaporates and the solution becomes more concentrated, crystallization begins. The as-grown thin film that has been spin-coated is typically placed on a hotplate for annealing. The purposes of annealing are usually: 1) to remove excess solvent; 2) to assist in the nucleation and growth of perovskite, and 3) to enlarge the grain size. Indeed, while the two-step method increases the complexity of the reaction, it also offers various synthesis possibilities, enabling precise control over the deposition process [82]. Most of its steps are similar to the one-step method, but it involves dissolving the Pb source and organic source separately before depositing them onto the substrate for crystallization through reaction with each other. Next, we would like to introduce another commonly used material form, single crystals. According to reports, single crystals of perovskite exhibit enhanced characteristics in comparison to their polycrystalline thin-film counterparts, including extended carrier diffusion distances, reduced trap-state densities, and increased stability [83, 84]. Similarly, these exceptional characteristics have stimulated the utilization of perovskite single crystals across a diverse array of applications.

1.6 Principles of nucleation and growth of perovskite single crystals

It is well-known that the growth of single-crystal materials typically involves two main steps: nucleation and growth. Next, we will briefly describe the differences between the traditional growth mechanisms and the current growth mechanism of perovskite materials.

1.6.1 Classical nucleation

The nucleation process of crystals involves both thermodynamic and kinetic factors, and based on an understanding of these conditions, certain preparatory factors need to be considered. The classical nucleation theory is founded on phase transitions and does not take into account the interaction between solute and solvent. Traditional nucleation theory is divided into homogeneous nucleation and heterogeneous nucleation. In the case of homogeneous nucleation, supposing a fresh spherical phase having a radius denoted as r, the overall change in free energy (ΔG_t) of the system can be formulated as [85]:

$$\Delta G_t = \Delta G_s + \Delta G_v = \pi r^2 \gamma_{GB} - \frac{4}{3}\pi r^3 \Delta G_v \qquad (1-4)$$

where, ΔG_v means the free energy per unit volume converted into a volumetric measure,

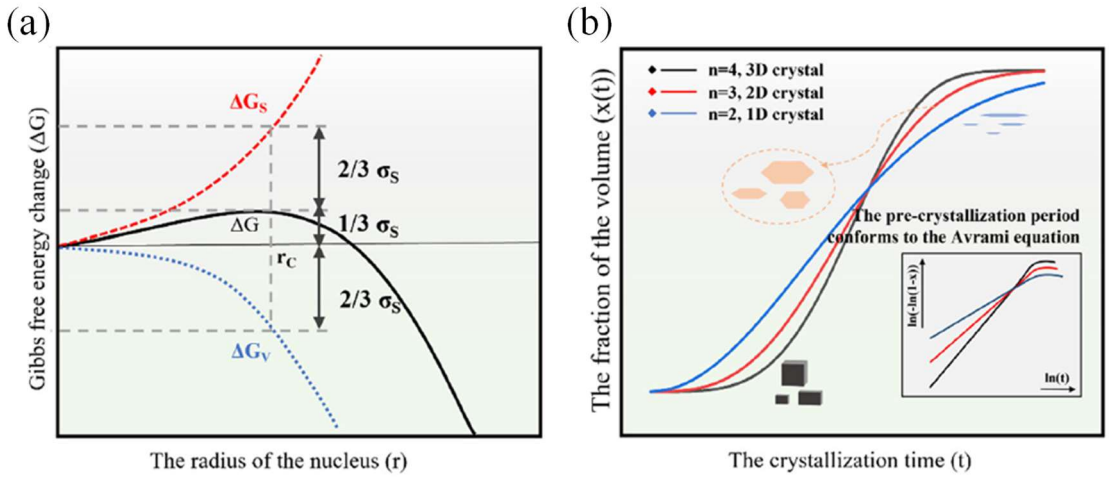

Figure 1-10(a). The change in free energy during the nucleation and growth process; (b). Growth models of 1D, 2D, and 3D crystals, respectively. The inset is a graphical representation with ln(t) [85].

γ_{GB} is the surface energy per unit area that exists between the nucleus and the liquid. Due to the quadratic and cubic relationships between surface and volume entropy and the radius r, we can obtain a nucleation curve that relates the free energy to the radius r through their mutual influence, as shown in Fig.1-10a [85]. From the curve, we can observe that it initially increases and then decreases as r increases, with the critical point being r_c. When r is smaller than rc, the surface energy becomes the dominant factor.

Within this interval, increasing the crystal nucleus's radius results in an elevation of the total free energy of the system, causing the crystal nucleus to become unstable and prone to dissolution in the solution. However, when r exceeds r_c, the volume free energy takes precedence. In this range, the system's free energy is inversely related to the crystal nucleus's radius, enabling the crystal nucleus to remain stable and grow within the solution [85]. In the case of heterogeneous nucleation, as the name implies, it involves nucleation at the interface between different phases. In this scenario, the interfaces between liquid-solid, liquid-nucleus, and solid-nucleus need to be considered. Assuming that the generated nucleus is a sphere with a radius of r, and the interface area between liquid crystal nucleus is A_{LC}, and the contact angle between solid and liquid is θ, the system's entropy ΔG_h can be described as [86]:

$$\Delta G_h = V\Delta G_V + \gamma_{LC}A_{LC} - \pi r^2\gamma_{LS}cos\theta \qquad (1-5)$$

where V represents the nucleus volume, γ_{LC} means the interface energy between liquid and crystal nucleus, and γ_{LS} is the interface energy between liquid and substrate. From the above equation, we can understand that the contact angle affects the overall entropy of the system. Moreover, the better the substrate's hydrophilicity, the more suitable it is for nucleation. Both forms of nucleation modes can be referenced nucleation process in Fig.1-11 [85].

1.6.2 Classical growth

After nucleation, the subsequent step is the growth of crystals. The growth process is closely related to solute diffusion and interface transition processes. When the area around the crystal nucleus consists of the same material, the interface phase transition becomes crucial. However, when the surrounding material around the crystal nucleus is different, solute diffusion to the interface is necessary. Then, through interface transition, it contributes to the growth of the crystal nucleus. In this scenario, solute diffusion plays a pivotal role. To more intuitively characterize the

growth rate of crystals, researchers typically use the relationship between the fraction (x) of the

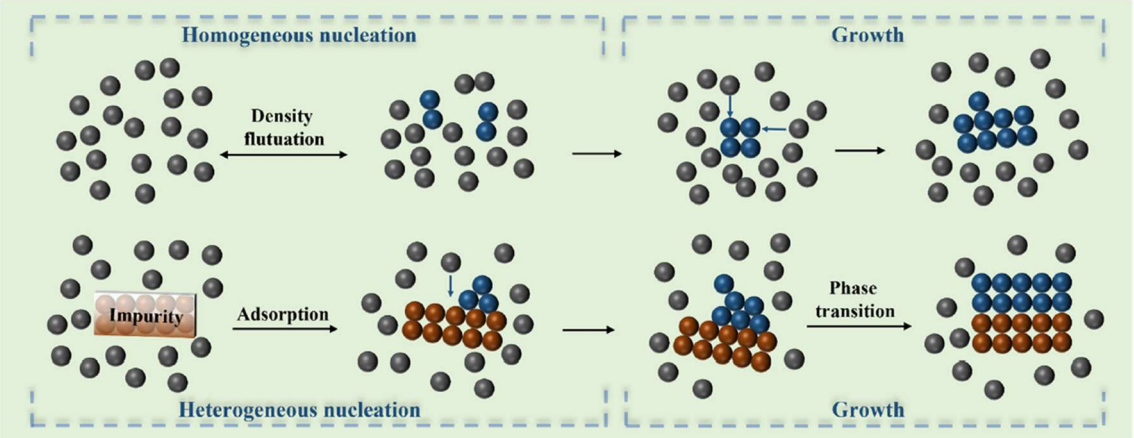

Figure 1-11. Mechanisms of nucleation and growth in traditional systems [85].

precipitated crystal volume relative to the initial volume of the parent solution and the crystallization time (t). Empirical formulas can express the relationship between the two factors [87]:

$$x = 1 - e^{-\frac{4}{3}IU^3t^4} \qquad (1-6)$$

where U is the crystal growth rate of an individual crystal nucleus's surface, I is the nucleation rate. Considering U and I as constants, the equation can be simplified to:

$$x = 1 - e^{-kt^n} \qquad (1-7)$$

where n is related to the dimensionality of the crystal, as shown in Fig.1-10(b). As observed, nucleation is slow at the beginning, with a relatively flat curve. In the middle stage, a large number of nuclei are formed, leading to a steep curve. In the final stage, when the solute is nearly depleted, the curve becomes flat again.

1.6.3 Perovskite nucleation

Perovskite crystals, as typical ionic crystals, differ from traditional melt-solidification crystallization. The various solutes need to be dissolved in a solution for crystallization, and accordingly, there is an increase in the factors that need to be considered. Most importantly, the

relationship between the solvent and solute is crucial for nucleation and crystallization. There can be various forms of solute-solvent interactions in the solution, such as individual solute X, solute cluster nucleation, or complexation involving solvent molecules A with x solute X molecules, and so on. The presence of these substances can influence the nucleation and growth processes of perovskite single crystals. Similar to traditional nucleation and crystallization, perovskite solutions also need to overcome a nucleation barrier ΔG, and the nucleation rate and number are related to the supersaturation of the solution. In contrast to traditional mechanisms, the nucleation

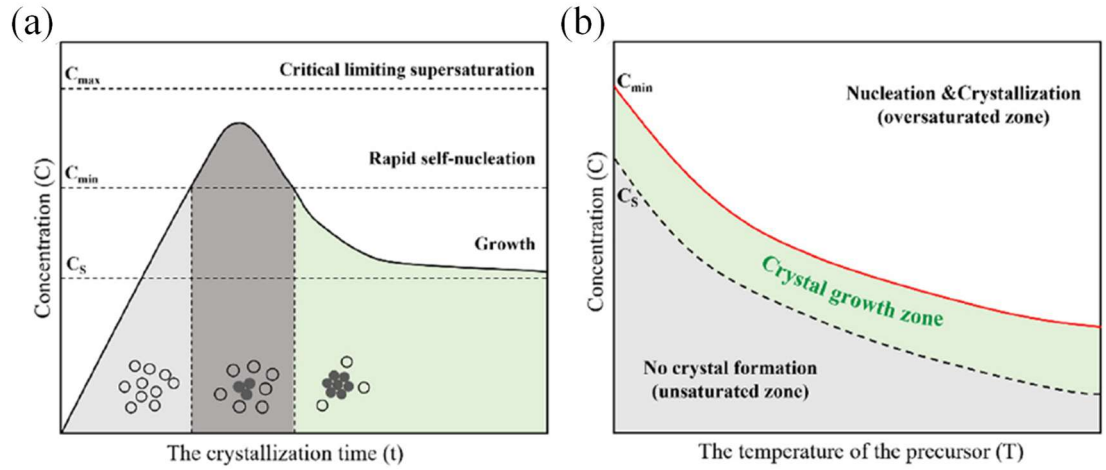

Figure 1-12(a). The LaMer's diagram describes the different stages of nucleation and growth of perovskite single crystals; (b) the different zones versus temperature [85].

and growth of perovskite single crystals can be divided into several steps based on different concentration states of the solution. LaMer's model is used to describe these different states, as shown in Fig.1-12a [88]. It is observed that the solution concentration is divided into the saturated concentration (C_s), the minimum nucleation concentration (C_{min}), and the maximum concentration (C_{max}). Thus, the concentration can also be divided into three regions. When the concentration is below C_s, no crystal nuclei are formed, and the solution remains in a relatively stable state. When the concentration is between C_s and C_{min}, a small number of crystal nuclei are formed, and heterogeneous nucleation can also occur during this stage. And when the concentration exceeds

C_{min}, rapid nucleation leads to the formation of a large number of nuclei, and the solution also enters an unstable state. After nucleation, growth occurs, bringing the solution back to a saturated state between C_s and C_{min}, where it is saturated but not to the extent that it produces a large number of new nuclei affecting growth. The method of adjusting temperature to control the solubility of a solution is very common in experiments. Therefore, temperature control is also a common consideration in nucleation and growth, as shown in Fig.1-12b. The Arrhenius-type equation is often used to describe the nucleation rate in a solution [89]:

$$J = \Lambda e^{-\frac{\Delta G}{k_B T}} \quad (1-8)$$

where Λ represents a parameter related to the supersaturation, ΔG is the nucleus energy barrier, k_B is Boltzmann constant and T is the absolute temperature. ΔG is related to the composition of solutes, solvents, and other substances mentioned above, which can be written as follows after modification by Zhumekenov, Ayan A., et al. [90]:

$$\begin{aligned} \Delta G &= -\frac{4}{3}\pi r^3(\xi - \xi_A + k_B T ln N_A) + \sigma \cdot 4\pi r^2 \\ &= \frac{16\pi}{3} \cdot \frac{\sigma^3}{(\xi - \xi_A + k_B T ln N_A)^2} \end{aligned} \quad (1-9)$$

where ξ represents the energy within the cluster, ξ_A is the energy of the solute X in isolation, N_A is the mole fraction of discrete solvent molecules, and σ is the surface energy of the solute cluster.

1.6.4 Perovskite growth

In the growth of perovskite single crystals, it is generally believed that there are concentration fluctuations around the nucleus, leading to changes between saturation and non-saturation of the solution around the nucleus during growth [90, 91]. This phenomenon is generally believed to be caused by the presence of two boundary layers around the nucleus, called the growth boundary layer and the diffusion boundary layer. As the crystal grows, the solute around

the nucleus is consumed, leading to the transient formation of a solution in a non-saturated state in the vicinity. As the crystal grows, the solute around the nucleus is consumed, and due to the presence of a diffusion layer, solute cannot be replenished quickly, resulting in the transient formation of a non-saturated solution state around the nucleus. Thus, there is an important connection between the growth of crystals, solute diffusion and transport, and the deposition on the nucleus to complete crystallization upon reaching the interface. The growth rate ψ can be expressed by the following equation [92]:

$$\psi = \Gamma\nu\frac{\Delta G_c}{k_B T}e^{-\frac{\Delta G'}{k_B T}} \qquad (1-10)$$

where Γ and ν denote geometric factor and trail frequency, respectively. ΔG_c represents the energy difference between the initial state and crystalline state, and $\Delta G'$ means the energy difference between the initial state and the activated state.

1.7 Synthesis of perovskite single crystals

We have already introduced the principles of traditional and current crystal growth of perovskites. Here, several commonly used methods for growing perovskite single crystals will be introduced. In general, single crystals can be grown using methods such as melt growth, solution growth, and vapor phase growth. However, due to the chemical and thermal instability of perovskite materials, the use of melt growth is relatively less common. Therefore, the solution growth method has become the mainstream approach for growing perovskite single crystals.

1.7.1 Solution temperature lowering (STL)

The STL method is a traditional approach for growing perovskite single crystals. It involves controlling the solubility of the solution by lowering the temperature to regulate the growth of single crystals. Hydrohalic acids serve as solvents in the STL method, allowing them to dissolve perovskite precursors while meeting the requirement of lowering solubility when the temperature

is decreased. Poglitsch, Albrecht, and Daniel Weber were the first to use this method to produce millimeter-sized single crystals of $MAPbI_3$ in 1987 [93]. This method, although feasible, is not very efficient, and it is both time-consuming and hard to grow larger, high-quality single crystals. As a result, on the basis of this traditional method, seed-assisted growth methods were derived. Bottom-seeded solution growth (BSSG) and top-seeded solution growth (TSSG) are common crystallization methods that utilize seed crystals. In the BSSG method, seed crystals are placed at

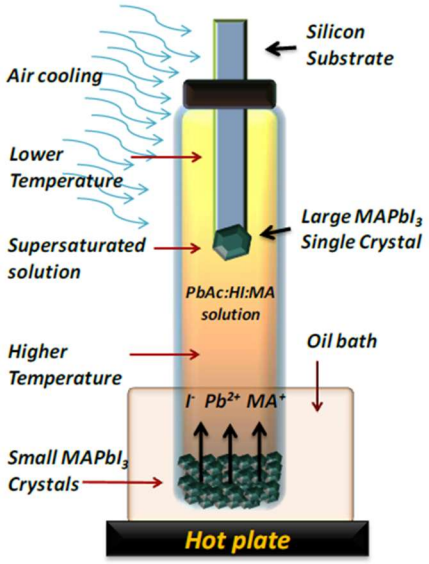

Figure 1-13. The set up of top-seeded solution growth method [95].

the bottom of the container, and crystalline growth is induced by cooling. According to the report by Lian et al. [94], nucleation at the bottom of the container during the cooling process can affect the growth of seed crystals, thereby influencing the formation of large single crystals. Therefore, they chose to use a platinum wire to secure the seed crystals, keeping them away from the bottom of the container to reduce the impact of bottom nucleation. A large single crystal measuring 12mm x 12mm x 7mm has been achieved using 15 days. The diagram of TSSG method has been shown in Fig.1-13. We can observe that the seed crystal is securely fixed to the silicon substrate at the top of the solution. Meanwhile, the entire solution at the bottom is heated by a hot plate while cold air is blown onto the top, creating a temperature gradient. At the same time,

numerous small crystals are kept at the bottom of the solution to maintain a continuously supersaturated state. In this way, the solubility above the solution is low, making it conducive to crystal growth, while the bottom continuously provides the solute necessary for crystal growth. This method is employed to grow large-sized, high-quality single crystals [95]. The above-mentioned cooling methods are generally common techniques for single crystal growth, but it is true that these methods can be time-consuming and difficult to control.

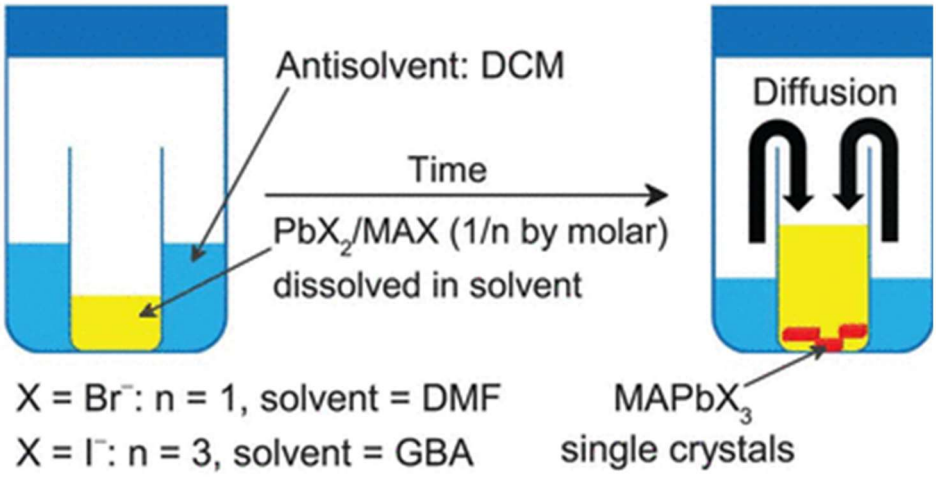

Figure 1-14. The set up of anti-solvent vapor-assisted crystallization method [96].

1.7.2 Anti-solvent vapor-assisted crystallization (AVC)

As is well-known, perovskite materials dissolve well in organic solvents such as DMF, DMSO, and GBL, but conversely, they have poor solubility in solvents like chlorobenzene, benzene, and diethyl ether. The AVC method utilizes this process by diffusing a solvent with low solubility into the precursor solution to induce the precipitation of perovskite crystals. As shown in Fig.1-14, there is a large container containing an open-top smaller container. The large container is filled with an antisolvent, while the small container contains a precursor solution prepared with an organic solvent. As dichloromethane (DCM) diffuses from the outside of the small container into its interior, perovskite crystals gradually precipitate [96]. The quality of single

crystal growth using this method is related to the choice of antisolvent. For example, in 2014, Tidhar, Yaron, et al. demonstrated that the results obtained using alcohol as an antisolvent were far inferior to those achieved with DCM [97]. Regarding antisolvents, besides DCM, solvents such as toluene, methanol, and mixtures solvent (DMF/DCM) have been verified as relatively effective antisolvents [98-100]. Additionally, factors such as the volume ratio of solvent to antisolvent and the rate of antisolvent diffusion can also influence the growth of crystals. In summary, the AVC method can yield high-quality single crystals with characteristics like smooth surfaces and high transparency. Crystal growth can be somewhat controlled by adjusting the antisolvent type and precursor concentration. However, it is worth noting that the process can still be time-consuming.

1.7.3 Inverse temperature crystallization (ITC)

ITC is currently one of the commonly used methods for growing perovskite single crystals, known for its ease of operation and fast crystallization rate. This method is based on the unusual solubility changes of perovskites in certain specific organic solvents. For example, in Fig.1-15, $PbBr_2$ and CH_3NH_3Br dissolve in DMF solvent, and as the temperature increases, their solubility decreases in 2015 [101]. M. Saidaminov et al. reported the synthesis of single crystals of $CH_3NH_3PbBr_3$ and $CH_3NH_3PbI_3$ using this method [102]. As shown in Fig.1-16, With the increase in temperature, perovskite single crystals can grow to sizes larger than 5mm within 3 hours, highlighting the rapid growth of single crystals using this method. Liu, Yucheng, et al.

successfully grew single crystals up to 2 inches in size using this method through multiple same

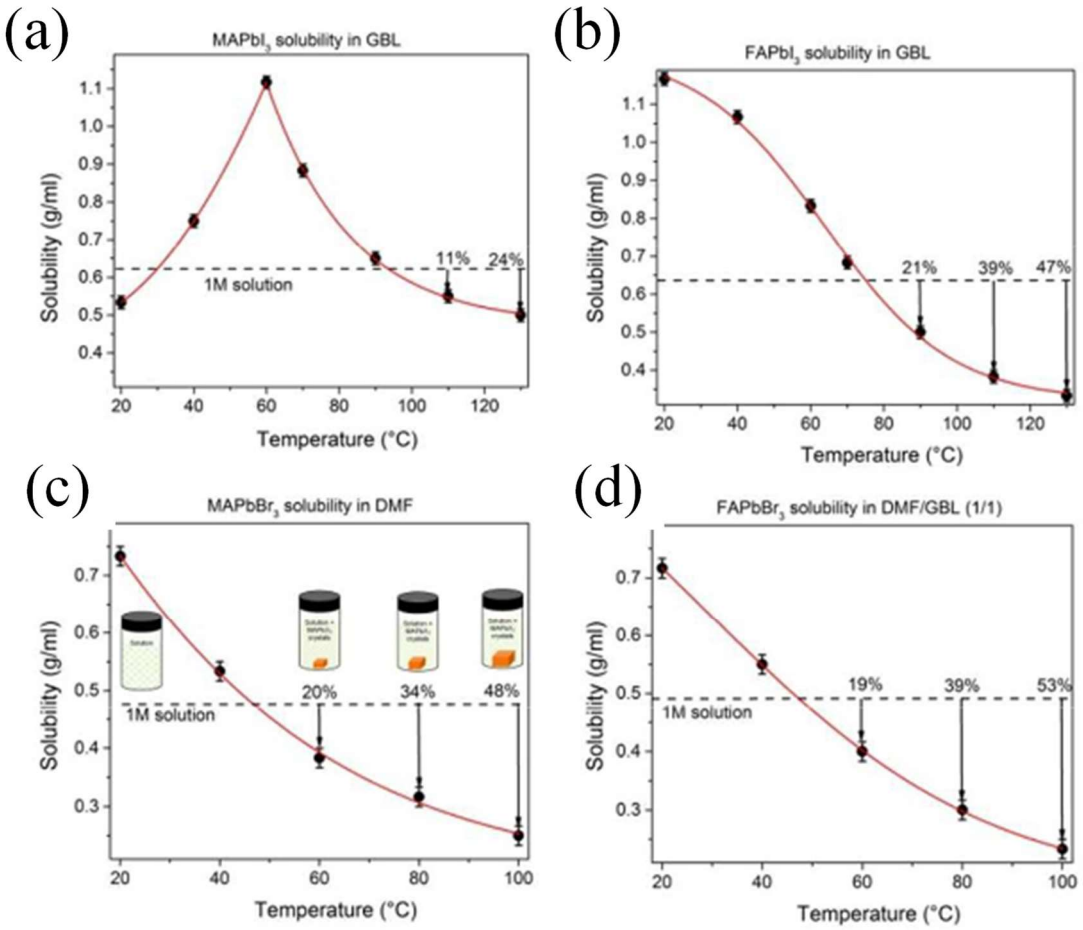

Figure 1-15. The anomalous solubility phenomenon of various perovskite materials in different solvents, (a). $MAPbI_3$ in GBL; (b). $FAPbI_3$ in GBL; (c). $MAPbBr_3$ in DMF; (d). $FAPbBr_3$ in DMF/GBL mixed solvent [101].

operations [103]. Liu, Xin, et al. provided a phase diagram that excluded the formation of the secondary phase $NH_4Pb_2Br_5$ and grew $FAPbBr_3$ single crystals using an improved ITC method [104]. However, this method, due to the high temperature and rapid crystallization, generally results in lower crystal quality compared to the two methods mentioned above. Therefore, there have been some studies aimed at further optimizing this method.

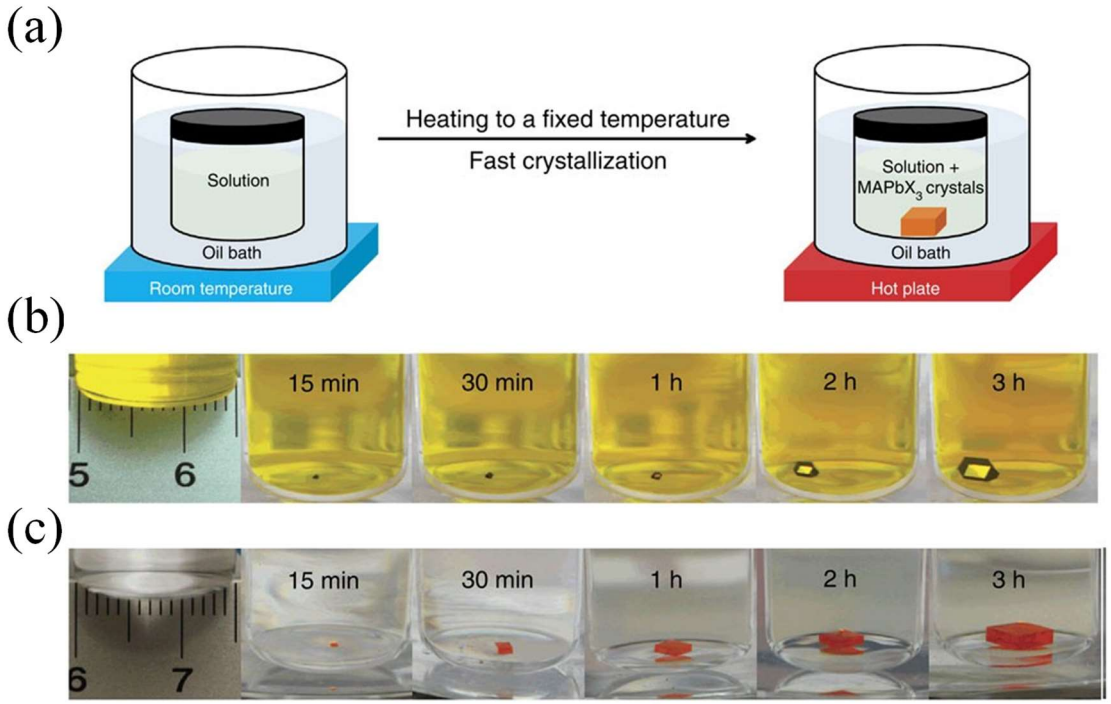

Figure 1-16(a). The set up of inverse temperature crystallization method; (b). Synthesis process of $CH_3NH_3PbI_3$ single crystals in 3 hours; (c). Synthesis process of $CH_3NH_3PbBr_3$ single crystal in 3 hours [102].

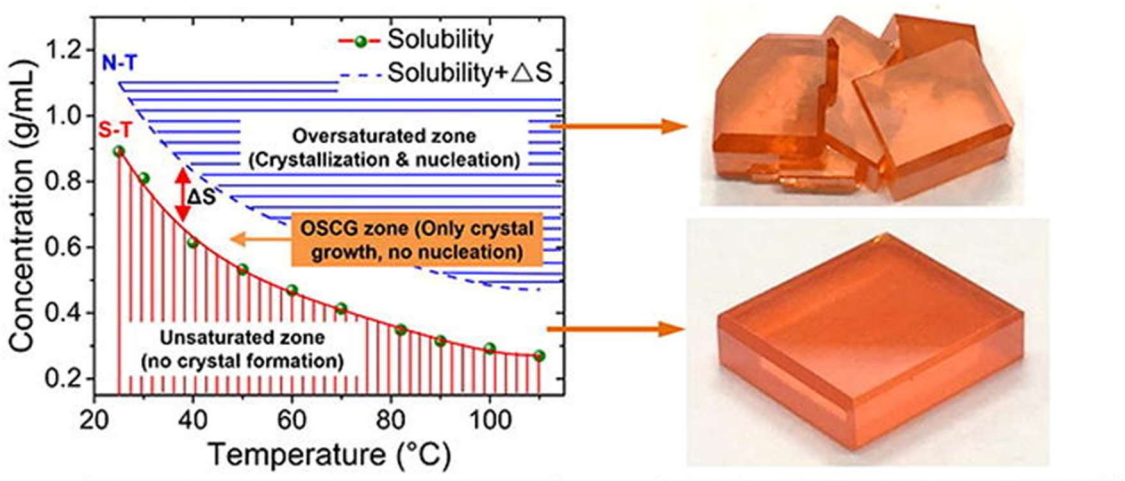

Figure 1-17. The solubility curves in different regions during the growth of perovskite single crystals, and the condition of single crystals grown in different regions [105].

1.7.4 Low-temperature-gradient crystallization (LTGC)

To address the issue of high temperatures in the ITC method, Liu, Yucheng, et al. proposed the LTGC method in 2019 [105]. As described in Fig.1-17, the relationship between solution concentration and temperature in the ITC method can be divided into three parts by two solubility curves. Similar to the perovskite nucleation and crystallization theory described earlier in the article, when the solution is below the solubility curve (S-T curve), it remains stable without nucleation or crystallization occurring. While above the S-T curve but below the nucleation curve (N-T curve), crystal growth can occur without nucleation, as the system has not overcome the

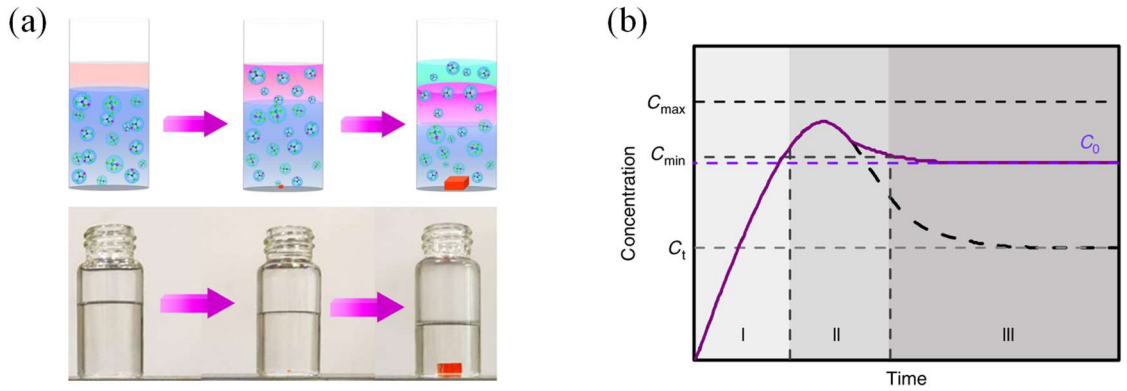

Figure 1-18(a). The single crystal growth mode in the Liquid diffusion separation-induced crystallization; (b). The change in solution concentration over time during the growth process [107].

nucleation barrier (ΔG). Once above the N-T curve, the solution enters a supersaturated state, leading to the generation of a large number of nuclei. Thus, crystalline growth must be controlled within the region between the S-T curve and the N-T curve to ensure the growth of high-quality single crystals. According to the supersaturation model [106], the growth rate of crystals is directly proportional to the first derivative of solution concentration with respect to temperature and the temperature ramp rate.

$$\frac{dm}{dt} = -\frac{1}{2}V \cdot M_P \frac{dC(T)}{dT}\frac{dT}{dt} \qquad (1-11)$$

where m represents the mass of crystal, C is the solution concentration, M_p means the molar weight of target perovskite, and V is the volume of the solution. The temperature ramp rate can

be controlled as a constant, so the main factors affecting crystal growth are related to the first derivative of concentration with respect to temperature. From the report of Liu, Yucheng, et al. [105], a curve of dC/dt is plotted, and it can be observed that in the low-temperature range (<60°C), dC/dt decreases almost linearly, while beyond 60°C, the dC/dt values become very small and nearly constant. Thus, in the low-temperature range, a significant quantity of high-quality crystals can be obtained with a rapid temperature increase, whereas the opposite holds true in the high-temperature range. Based on this, it can help address the drawbacks of high-temperature growth in the ITC method.

1.7.5 Liquid diffusion separation-induced crystallization (LDSC)

The method mentioned above controls the solution concentration by guiding solute precipitation through temperature control, whereas the LDSC method controls the overall solution concentration by manipulating the quantity of solvent. As shown in Fig.1-18, Yao, Fang, et al. added silicone oil to the precursor solution to guide solvent diffusion [107]. Once the solvent has diffused through the silicone oil, the precursor solution becomes more concentrated, leading to the precipitation of single crystals in the supersaturated solution. This method controls the solution concentration to grow single crystals by managing the accumulation and consumption of precursors, maintaining the solution in a metastable state between supersaturation (C_{min}) and saturation (C_t). Furthermore, this method has been validated to grow high-quality single crystals, providing further confirmation of the correctness of the growth theory of perovskite described earlier.

1.7.6 Additive modification growth

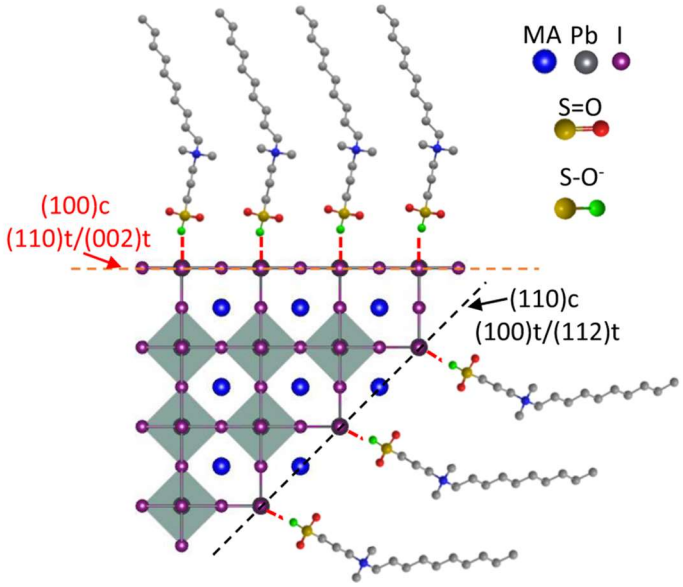

Figure 1-19. Coordination modes of DPSI with different crystal facets in $MAPbI_3$ [15].

In addition to controlling the solubility of a solution through temperature or solvent diffusion for crystal growth, another method to regulate crystal growth is by controlling solute binding. Liu, Ye, et al. controlled crystal orientation by introducing 3-(Decyldimethylammonio)-propane-sulfonate inner salt (DPSI), achieving the desired crystal growth control, which is called ligand-assisted solution growth (LSG) [15]. As shown in Fig.1-19, the $S\text{-}O^-$ bond in DPSI forms an ionic bond with the Pb^{2+} in the $MAPbI_3$ lattice, preventing iodine coordination, thereby inhibiting the growth of perovskite single crystals. Due to the varying Pb densities on different crystal facets, one can control the shape of single crystals by manipulating the growth orientation based on this principle. This method, by controlling the crystal growth rate, has been proven to be a way to grow high-quality single crystals. In addition to sulfate ligand additives, Ma, Lin, et al. reported a method of adding polymers to control nucleation [108]. Polyethylene glycol (PEG), polypropylene glycol (PPG), polyacrylic acid (PAA), and polyvinyl alcohol (PVA) are polymers containing

oxygen functional groups that are used as additives to control crystal growth. In the original ITC

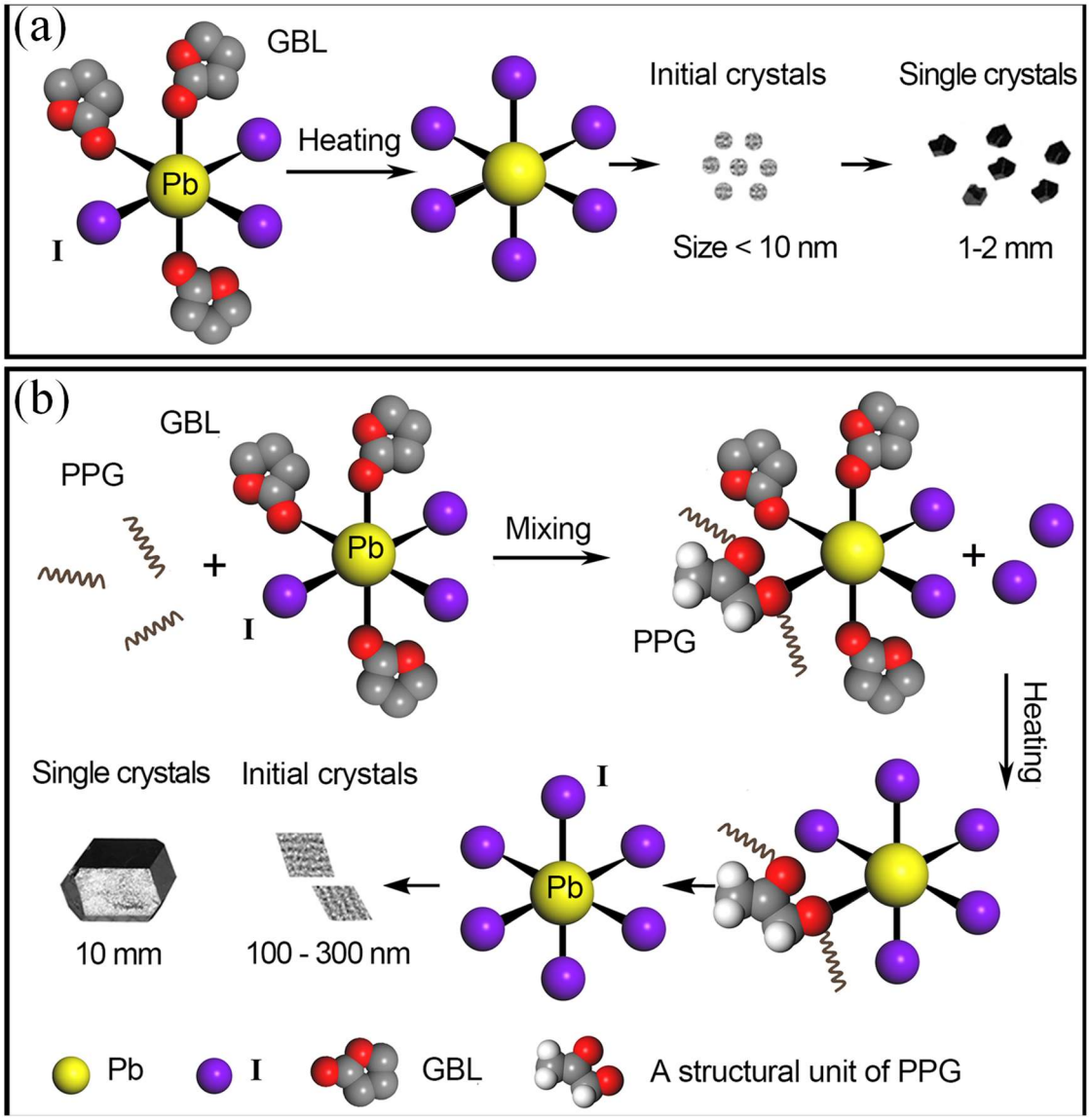

Figure 1-20(a). Schematic diagram of the original ITC crystallization method;(b). Schematic diagram of polymer-assisted ITC crystallization [108].

method shown in Fig.1-20a, solvent molecules in the solution would coordinate with Pb, forming complexes of Pb-solvent molecules. However, as the temperature rises, solvent molecules rapidly detach, resulting in the formation of PbX_6 octahedron. These PbX_6 octahedron aggregate rapidly, leading to the formation of numerous nuclei and rapid growth. Adding polymers, as shown in Fig.1-20b, the oxygen groups in the polymers coordinate with Pb ions,

forming new complexes. As the temperature increases to supersaturation, they gradually detach, leading to the formation of nuclei. The addition of an appropriate amount of polymer can effectively reduce the number of single crystals, maintain the growth equilibrium of the solution, enhance stability, and thus grow higher-quality single crystals. The above-mentioned method, by adding ligand additives to control the coordination of Pb ions and thereby regulate crystal growth, is an important improvement to the ITC method.

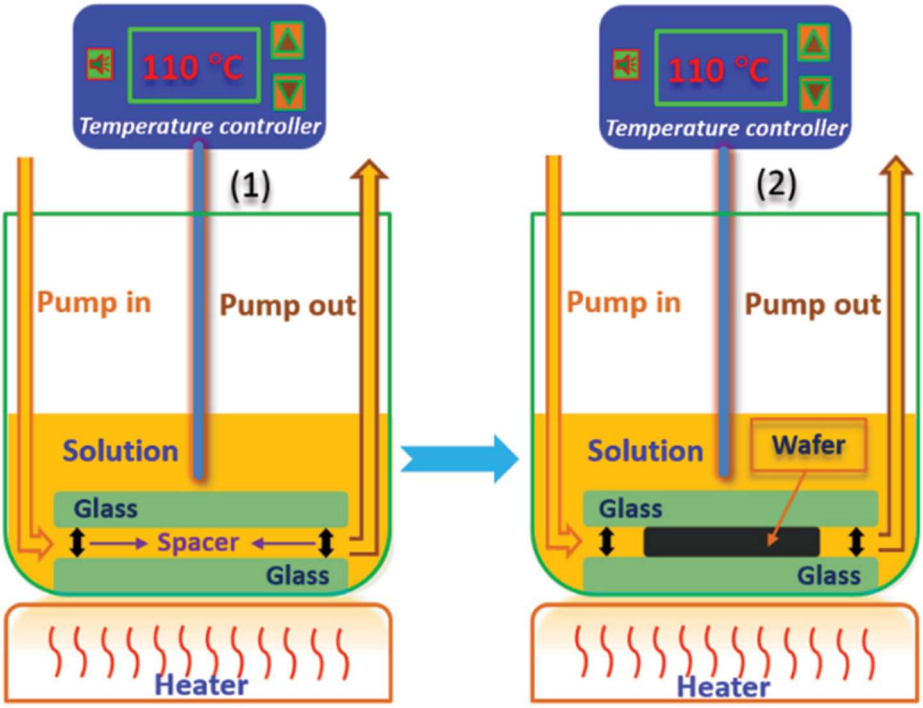

Figure 1-21. Schematic diagram of the spatial confinement method for growing perovskite single crystal thin films [109].

1.8 Synthesis of single crystal thin film

The above description is about the methods for growing three-dimensional perovskite single crystals. However, the single crystals grown by these methods are often large and thick, which is not conducive to the application in optoelectronic devices. In contrast, polycrystalline thin-film materials, despite having many grain boundaries and defects, are still widely used in the field of optoelectronics. This is because single crystals are thick, and in the case of solar cells, the

thickness of single crystals can even exceed the diffusion length of their own charge carriers, making it difficult to efficiently collect photogenerated charge carriers. Therefore, thinning down single crystal materials not only improves the crystalline quality of thin films but also enhances the performance of devices. Producing single crystal thin films has also become an important research topic.

1.8.1 Space-confined method

The space-confinement method, as a more straightforward approach, involves restricting crystal growth in one direction, allowing the crystal to grow to a fixed thickness. In 2016, Liu, Yucheng, et al. successfully grew single crystal thin films of $MAPbI_3$ using this method with thicknesses ranging from 150μm to 1440μm [109]. As shown in Fig.1-21, the authors controlled the crystal growth in the vertical direction by sandwiching the selected spacer between two glass slides. Furthermore, to maintain the solution in a state of continuous supersaturation, the authors used a peristaltic pump inside the growth container to ensure dynamic flow of the solution. Subsequently, using the spatial confinement apparatus, Rao, Hua-Shang, et al. successfully produced large-area 120 cm^2 $MAPbBr_3$ perovskite single crystal thin films with thicknesses ranging from 100 to 800 μm [110]. In this setup, two sheets of fluorine-doped tin oxide (FTO) glass were positioned together with a U-shaped polytetrafluoroethylene (PTFE) film, and the thickness of the PTFE film was used to control the thickness of the films. Chen, Zhaolai, et al. further developed this method by placing two hydrophobically treated glass slides together on a hotplate and then dripping the precursor solution onto the overlapping sections of the two glass slides. Due to capillary action, the solution would flow into the gaps between the two glass pieces. With the heating of the hotplate, the space between the two glass slides became the site for single crystal growth. This approach also allowed for further reduction in the thickness of the thin films to

approximately a few tens of micrometers [111]. Alsalloum, Abdullah Y., et al. employed this approach to fabricate solar cells using $FA_{0.6}MA_{0.4}PbI_3$ as the material, achieving an efficiency of up to 22.8% [112]. The specific fabrication process, as depicted in Fig.1-22, involves placing an ITO glass coated with poly (triaryl amine) (PTAA) on a hotplate. PTAA serves a dual purpose as both a charge transport layer and a hydrophobic coating. Subsequently, the precursor solution is dripped onto the PTAA-coated ITO glass, and another PTAA-coated ITO glass is placed on top. As the hotplate heats up, after the completion of single crystal growth, a blade is used to cut it into the desired shape, resulting in the fabrication of perovskite single crystal thin films. As described in the previous reports, while this method allows for the growth of single-crystal thin films, it is challenging to achieve both thinness and a large size simultaneously. Some researchers were able to produce large thin films, but due to the limitations of the spacer, they couldn't reduce the thickness to a few micrometers or smaller, making it still challenging for applications in devices such as batteries. On the other hand, some researchers were able to create relatively thin single-crystal thin films, but the size of the crystals obtained was very small (2-3 mm^2).

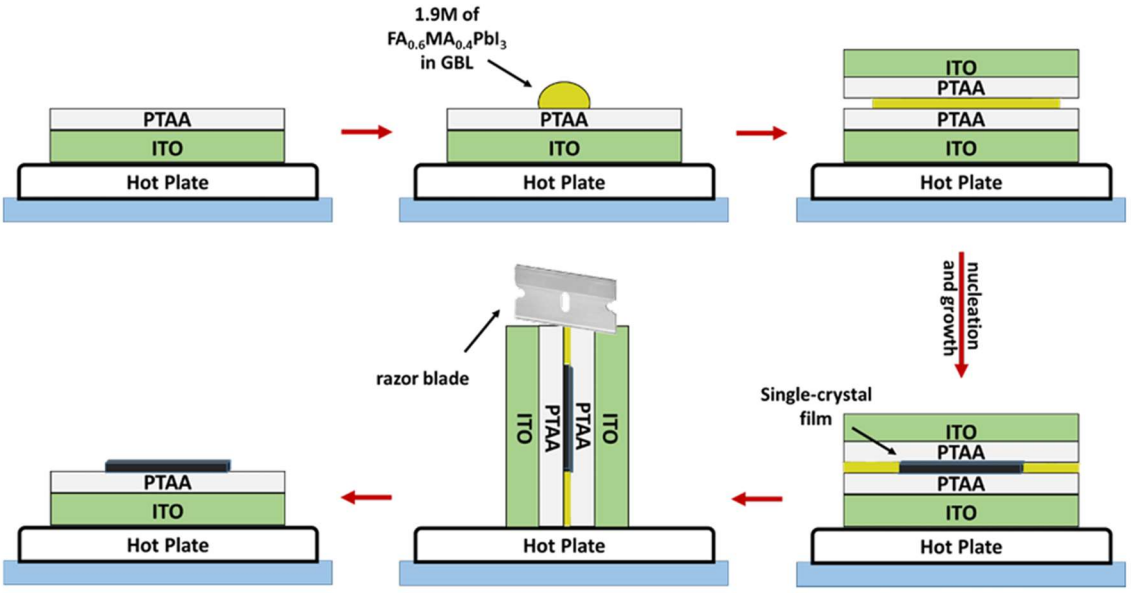

Figure 1-22. Fabrication process for the growth of single crystal thin films [112].

1.8.2 Top-down method

A different approach commonly used to produce perovskite single crystal thin films is the top-down method, which begins with perovskite bulk single crystals and then reduces their dimensions through cutting or etching processes [113]. Liu, Yucheng, et al. used this approach to

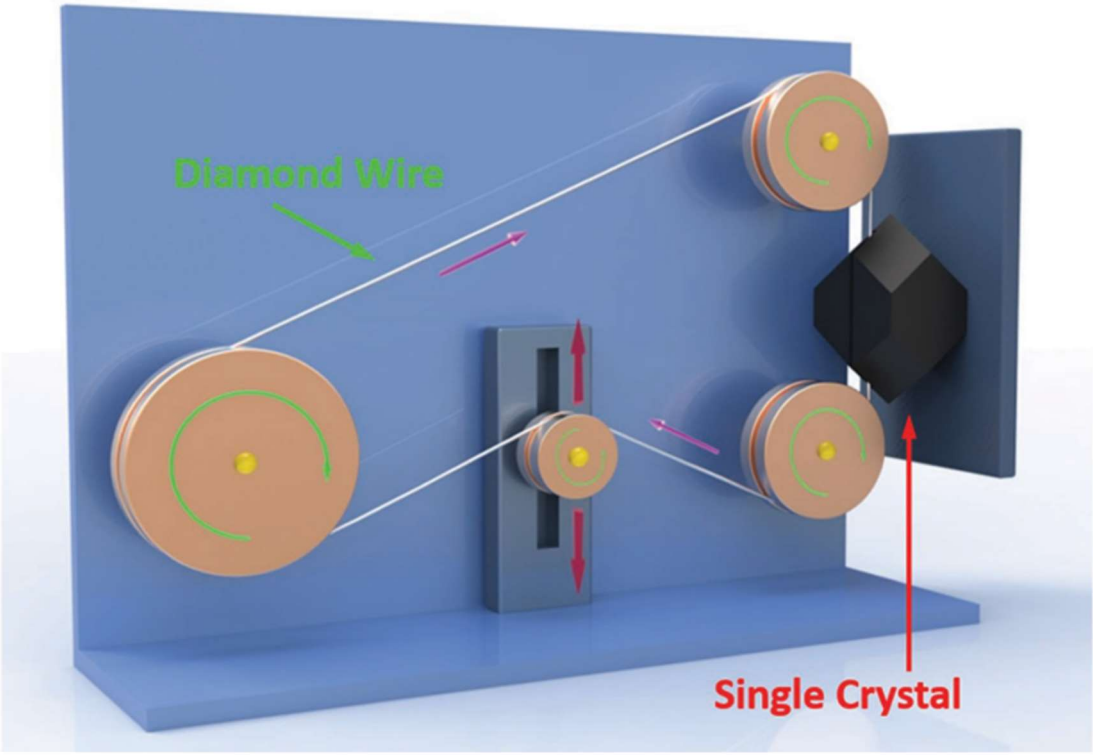

Figure 1-23. The diagram depicting the process of slicing a single-crystalline wafer [114].

create inch-sized $FAPbI_3$ single crystal thin films with a thickness of 100 micrometers [114]. They employed a diamond wire slicing machine to cut a large single crystal into thin slices, as shown in Fig.1-23. The sliced single-crystal wafers retain the same properties as the original single crystal. Soon, researchers applied this method to various perovskite single crystals, including $MAPbI_3$, $MAPbBr_3$, and $MAPbCl_3$. The thickness of the single crystal thin film could be regulated by adjusting the immersion time, temperature, and the concentration of the etching solution. Using this method, single crystals with centimeter-scale dimensions and a thickness of 15μm can be produced. Compared to the space-confined method, the top-down approach is more

suitable for manufacturing large-sized single crystal thin films. However, for the fabrication of single crystal thin film devices, this method may not be as practical.

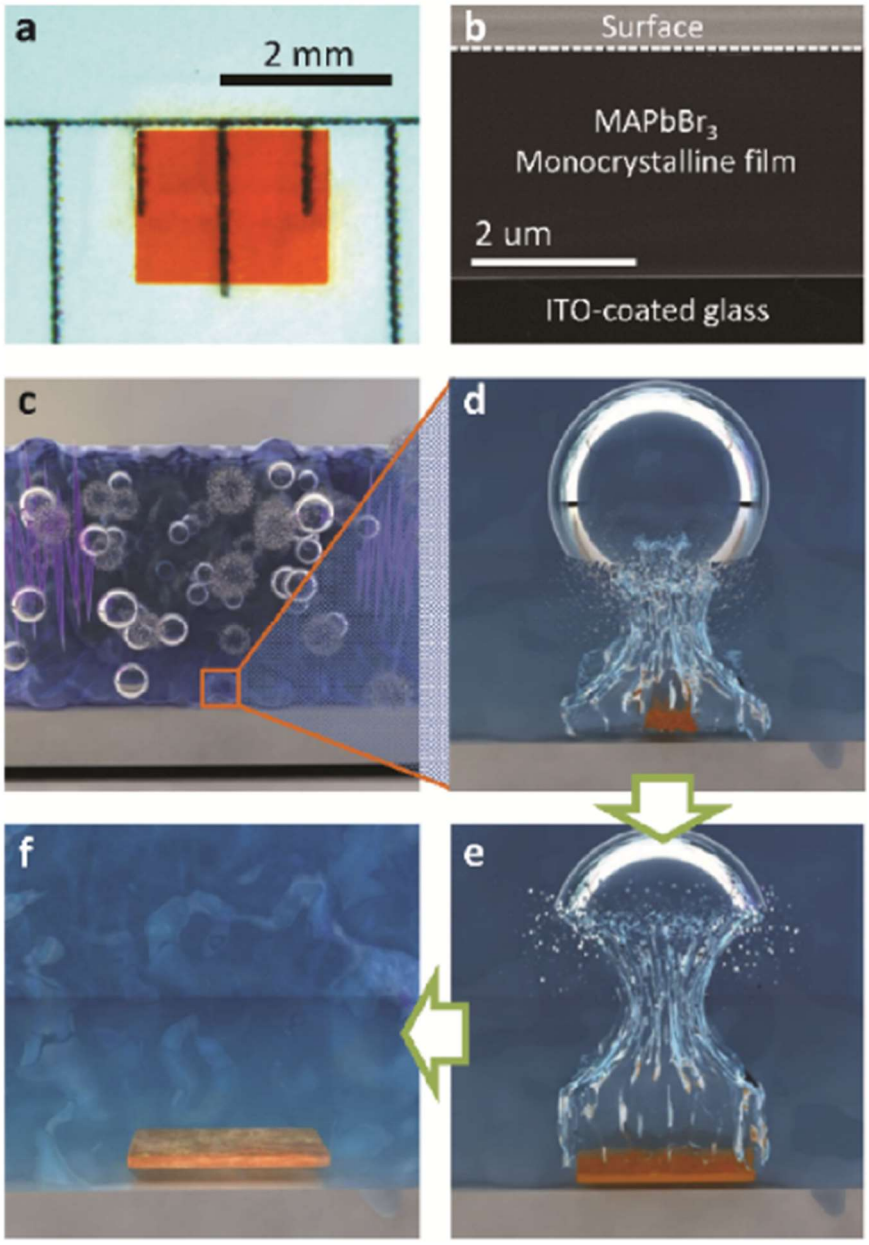

Figure 1-24(a). Picture of $MAPbBr_3$ single crystal thin film; (b). Cross-sectional SEM image of the $MAPbBr_3$ single crystal thin film; (c)-(e). Schematic Diagram of Cavitation-Triggered Asymmetrical Crystallization [115].

1.8.3 Cavitation-triggered asymmetrical crystallization (CTAC)

The CTAC method induces nucleation through ultrasonic waves. As shown in Fig.1-24, ultrasonic waves lead to the generation and collapse of cavities, releasing transient high energy that can overcome the nucleation barrier to form nuclei, which reported by Peng, Wei, et al. [115]. The cavities' collapse exhibits asymmetry near the substrate and produces high-velocity fluid jets directed toward the substrate, thereby contributing to the asymmetric growth of crystals. This method allows for the adjustment of single crystal thickness by varying the growth time and precursor concentration. The advantage of this method is that it enables the growth of single crystal thin films on various substrates, including FTO, ITO, and silicon wafers.

1.8.4 Surface tension assisted growth

The surface tension-assisted crystallization method involves the use of the principle where the surface nucleation barrier in the solution is small, and the nucleation rate is high, to grow single crystal thin films. Zhumekenov, Ayan A., et al. were the first to employ this method, obtaining perovskite single-crystal thin films with an approximate thickness equivalent to the carrier diffusion length (~5-10μm), measuring 1 cm^2 [89]. According to the aforementioned perovskite crystallization principle, the nucleation rate at the solution surface can be expressed as follows:

$$\Delta_s = \frac{16\pi}{3} \frac{\gamma^3}{\left(\varepsilon + \varepsilon_{surf} - \varepsilon_A + k_B T \cdot \ln(N_A)\right)^2} \qquad (1-12)$$

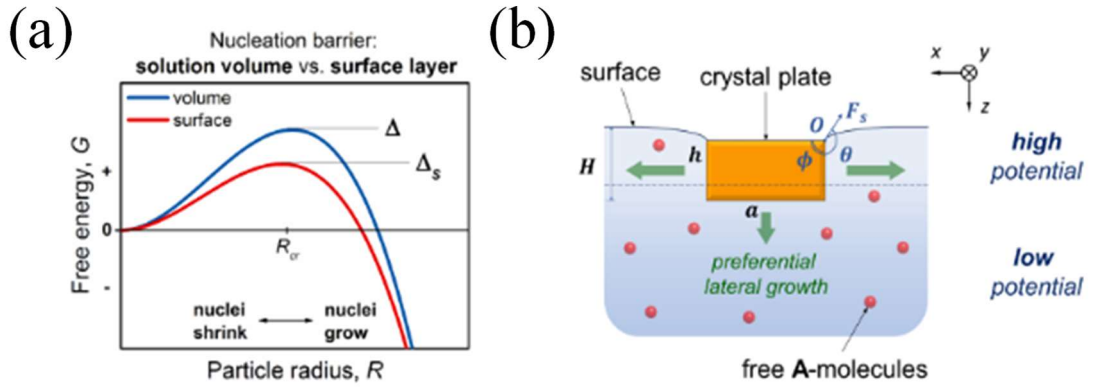

Figure 1-25(a). The relationship between nucleation radius in a solution and at the surface and the change in system free energy; (b). Surface tension-assisted growth mode diagram [89].

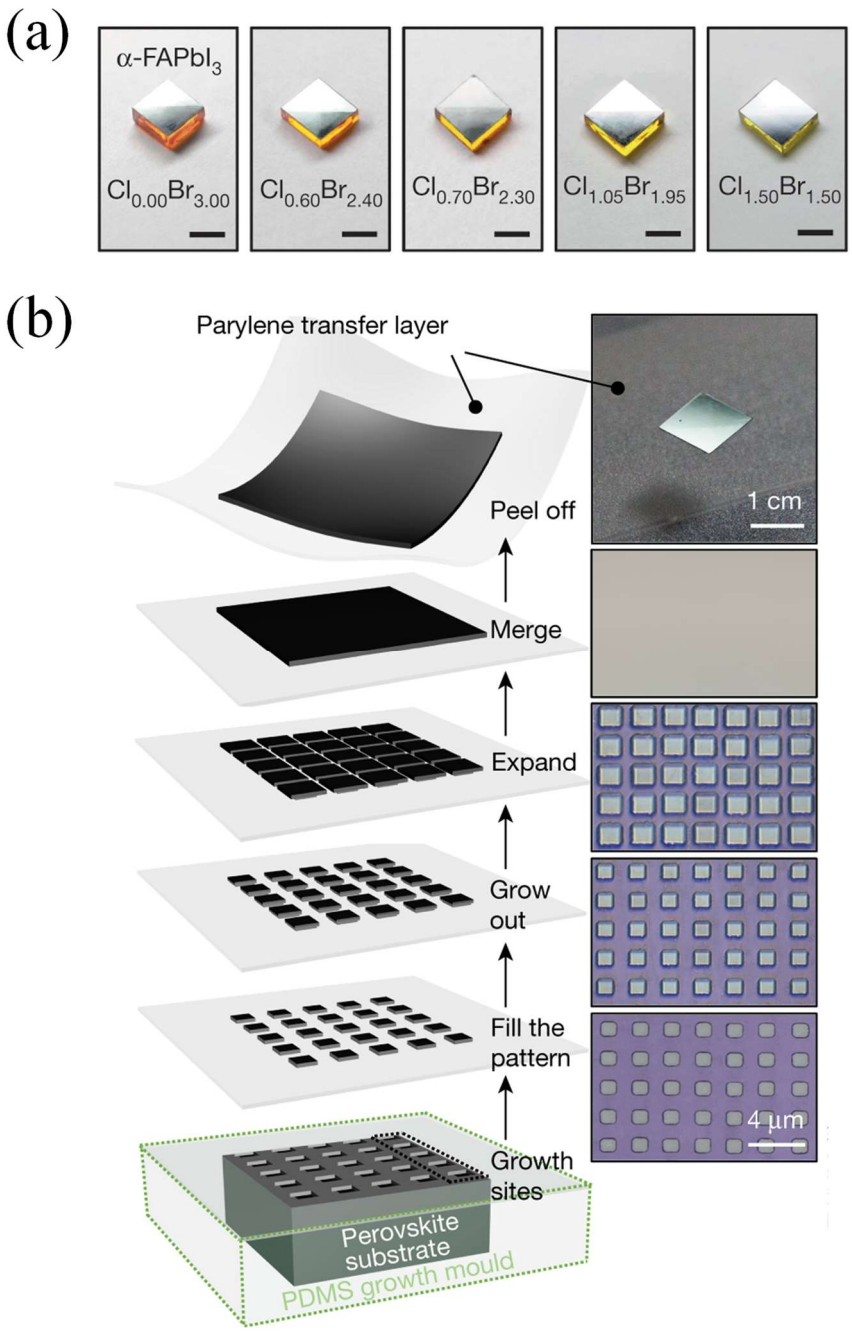

Figure 1-26(a). Epitaxial growth of α-$FAPbI_3$ single crystals based on $MAPbBr_xCl_{3-x}$ single crystal substrates [116]; (b). Diagram of solution-based lithography-assisted epitaxial growth method [117].

where ε_{surf} is the elastic energy per A-molecule in the surface layer associated with surface tension. Due to the presence of ε_{surf}, the nucleation barrier is smaller compared to that in the

solution. As shown in Fig.1-25, it is easier to achieve lateral growth after surface nucleation. To maintain a large area of single crystal on the solution surface, the coordination of various factors is required, with surface tension being the most important among them. Assuming a crystal with density ρ and dimensions of a × a × h is floating on the surface of a solution with a density ρ_{sol}, the net forces balance on the solution surface can be represented by the following formula:

$$ah \approx \frac{4\sigma_{sol}\sin(\theta - 90^{\circ})}{(\rho - \rho_{sol})g} \qquad (1-13)$$

where σ_{sol} is the surface tension coefficient, θ is the contact angle with the liquid, and g is the gravitational constant. According to Equation 13, we can understand that in order to create an environment conducive to surface tension-assisted growth, it is necessary to use solvent with high density and surface tension coefficients, as well as solutions with larger contact angle. While this method can produce very thin single-crystal films, on the contrary, due to the extreme fragility of perovskite, it is challenging to guarantee the successful retrieval of fully grown perovskite single-crystal films from the solution.

1.8.5 Epitaxial growth

Epitaxial growth is also a commonly used method in crystal growth, as the name suggests, it involves growing single crystals on a selected substrate along a predetermined pattern. Due to the various modes of epitaxial growth, we will focus here on solution-phase growth on lattice matched substrates. The issue of lattice matching with the substrate has always been a significant issue in epitaxial growth. Chen, Yimu, et al. used a series of $MAPbBr_xCl_{3-x}$ single crystal substrates for the epitaxial growth of α-$FAPbI_3$ single crystals as shown in Fig.1-26a [116]. Achieving lattice variation in the substrate is accomplished by regulating the halogen composition of the substrate. Through this approach, the authors adjusted the mismatch between the thin film and the substrate to apply strain to the α-$FAPbI_3$ film, thereby enhancing the phase stability of α-

$FAPbI_3$ and a range of optoelectronic properties. In 2020, Lei, Yusheng, et al. proposed a solution-based lithography-assisted epitaxial growth method, which effectively enables the production of high-quality single crystal thin films [117]. As shown in Fig.1-26b, a layer of polymer mask is patterned on the substrate (e.g., $MAPbI_3$ single crystal) for epitaxial growth. Due to the constraints of the mold, single crystals grown epitaxially may penetrate through the holes in the mask. After filling the entire mask, the epitaxially grown single crystals will laterally grow along the upper edge of the mask and eventually connect together to form a thin film. Subsequently, the thin film can be peeled off and transferred to create high-performance single-crystal devices. The thickness of the thin film can be controlled by the size of the mask's apertures.

1.9 The properties of perovskite single crystals and their applications

Perovskite single crystals exhibit superior physical properties compared to their thin-film counterparts, including optical, electrical, and thermal characteristics. The optoelectronic properties among these characteristics are widely studied because their parameters directly affect the performance of devices. For instance, it has been reported that perovskite single crystals have lower trap state densities [118], longer carrier diffusion lengths [95], higher optical absorption coefficients[119], and so on. Among these properties, trap sate density is a key parameter that affects the motion of charge carriers within the material. To our knowledge, trap state density can be characterized using various methods, such as PL technique, I-V characteristic curves and capacitance-frequency (C-f) measurements, etc., and the trap state density in perovskite polycrystalline thin films is mostly estimated to be in the range of 10^{15} to 10^{17} [120]. Reportedly, the trap state density in single crystals can be lower by 5-7 orders of magnitude compared to their counterpart thin film materials. Therefore, in some optoelectronic devices where carrier diffusion length is crucial, a lower trap state density can reduce non-radiative recombination, leading to improved device performance. For example, the electronic traps clustered at grain boundaries in

polycrystalline thin films can lead to non-radiative recombination which can impact the fill factor (FF) and result in open-circuit voltage (V_{oc}) losses in perovskite-based solar cells [121]. In single crystals, the lower defect density further reduces such non-radiative recombination, thus extending the lifetime of charge carriers and enhancing the quantum yield.

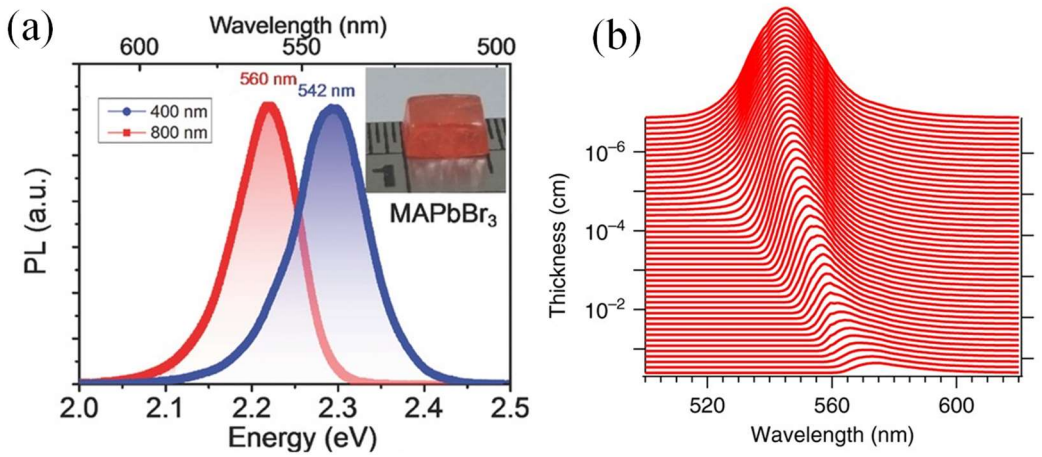

Figure 1-27(a). The photoluminescence spectra of $MAPbBr_3$ single crystals were obtained using both 400nm (single-photon) and 800nm (two-photon) excitation [122]; (b). Calculated PL emission as it passes through the thickness of a 2 mm thick crystal due to reabsorption [123].

Furthermore, the optical properties of perovskite single crystals have also been extensively researched. In addition to the tunable absorption spectra mentioned earlier, the emission properties of perovskite single crystals are also worth mentioning. We can observe that the most typical difference between conventional single crystals and thin films is their thickness. Three-dimensional single crystals can have thicknesses on the order of millimeters, while typical thin films are in the range of a few hundred nanometers. This substantial difference in thickness results in significant disparities in their emission properties as well. In 2016, Wu, Bo, et al. reported different emission properties at the surface and in the interior of $MAPbBr_3$ and $MAPbI_3$ single crystals, using both single-photon and two-photon excitation [122]. As shown in the Fig. 1-27a, it can be observed that the PL peak at the surface is blue shifted compared to the interior. The authors attributed this phenomenon to lattice deformation near the surface. Wenger, Bernard, et al. also

observed a similar phenomenon in $MAPbBr_3$ single crystal. Considering the thickness, they believed that self-absorption within the crystal itself caused this effect. They conducted simulations using the Beer-Lambert law and verified this hypothesis as shown in Fig.1-27b [123]. In addition to these explanations, there are also other interpretations, such as the coexistence of different crystal phases [124], the coexistence of direct and indirect bandgaps [125], and defect-induced bound excitons emission [126], etc.

Perovskite single crystals have a wide range of potential applications, such as the perovskite single crystal solar cells mentioned earlier. However, single crystal solar cells still face challenges in terms of processing, making them large and thin while achieving the best commercial prospects remains quite difficult. The previously mentioned growth methods for single crystal thin films represent an approach to addressing these challenges in some extent. Researchers have proposed another solution, which is to abandon the vertical-structural device and opt for a lateral-structural device. This can effectively reduce the impact of single crystal thickness on charge carrier transport. In 2019, Liu, Ye, et al. introduced C_{60} as an electron transport layer and fabricated lateral solar cells based on $MAPbI_3$ single crystal, achieving a PCE of 5.9% [127]. Similar to this, research on optimizing device structures and interfaces is ongoing, and perovskite single crystal solar cells still need to overcome many challenges. Indeed, photodetectors are another promising field for the application of perovskite single crystals. While solar cells convert light energy into electrical energy, photodetectors are designed to convert incoming light signals into electrical signals. They serve important roles in various applications such as optical communication, imaging, and sensing. Perovskite single crystals do indeed offer a wide range of light detection capabilities, spanning from near-infrared, visible light, and ultraviolet regions to even the high-energy X-ray domain. This versatility in detecting various wavelengths of light makes perovskite materials attractive for a broad spectrum of applications in optical and X-ray detection technologies. For example, in

visible light detection, perovskite single crystal-based detectors have demonstrated innovative uses in high-speed optical communication and high-resolution imaging, both in scientific research and various industries. This is attributed to their high optical absorption coefficient, tunable optical bandgap, excellent carrier mobility, and extended carrier diffusion length [128].

1.10 Research purpose

From the aforementioned information, it becomes evident that perovskite materials have a wide range of applications in the field of optoelectronic devices. They also possess the potential to replace traditional semiconductor materials in various commercial uses. Indeed, single crystal materials exhibit superior crystallinity and lower defect concentrations, making them excellent choices for both device fabrication and fundamental material property research in the field of perovskite optoelectronics. Therefore, we are focusing our attention on the intrinsic properties of perovskite single crystals, as the material's intrinsic characteristics can provide valuable guidance for its application in devices. For fundamental property research, such as the study of carrier and thermal diffusion in perovskite single crystals, it's important to note that different measurement methods can lead to varying results. Currently, many techniques are relatively specialized, with each method corresponding to a specific parameter. For example, to determine the surface recombination velocity of a single crystal, transient absorption in the reflection mode is often employed to observe the carrier dynamic changes on surface of the material. However, this method demands high-quality samples with smooth surface to effectively collect reflected light for measurement. In some cases, it is necessary to characterize multiple properties of a material, including optical, electrical, and thermal properties, the measurement requirements become more complex. Ensuring the integrity of the material is crucial in obtaining convincing and reliable results. To address this issue, we have developed a method in the field of perovskite materials that has not been widely used before, photoacoustic (PA) technique. This method allows for the

simultaneous testing of the optical, electrical, and thermal properties of the material while also providing effective sample protection in a PA cell. We have applied this method to typical $MAPbBr_3$ and $MAPbI_3$ single crystals and demonstrated the feasibility of PA technique in the perovskite field. We look forward to seeing this method being widely adopted for other perovskite materials, providing reliable foundational data for device fabrication. Next, we will shift our focus to perovskite single crystals in mixed halide systems. Mixed halides, especially bromine-iodine mixtures and halide engineering, as mentioned in previous chapters, play a crucial role in the entire perovskite system. In this system, iodine ions are prone to ionic migration, leading to the accumulation of pure iodine phases, which can degrade the performance of corresponding devices [65]. Hence, extensive research has been conducted to understand the principles behind this phenomenon, the influencing factors, and strategies for its suppression. Despite these efforts, this issue has not been completely resolved. And, due to the significant attention focused on phase separation phenomena, the intrinsic properties such as carrier dynamics which is an intrinsic property of materials, can effectively help in understanding the recombination mechanisms within the material and the relaxation states of carriers under photoexcitation of mixed phases (Br/I) are sometimes overlooked. To address the issue, we conducted a study on the carrier dynamics of iodine-doped $MAPbBr_3$ single crystals using steady-state and time-resolved PL (TRPL) technique. Our study has provided valuable insights into the impact of iodine doping on the carrier dynamics of $MAPbBr_3$ single crystals, further advancing our understanding of these materials. This research contributes to the knowledge base surrounding perovskite materials and can potentially inform future developments in their applications and performance optimization.

1.11 Outline of the thesis

Chapter 1 mainly introduces the properties of perovskite, the principles and methods of single crystal synthesis, and the purpose of the study.

Chapter 2 introduces the instruments used in our experiments and the measurement techniques, detailing their functions and principles.

Chapter 3 studies the practicality of the photoacoustic method in perovskite materials. In this chapter, typical perovskite single crystals $MAPbX_3$ (X= Br, I) are synthesized through the inverse temperature crystallization method. The reflection detection configuration mode and transmission detection configuration mode of the photoacoustic (PA) method are used to measure the synthesized perovskite single crystals. Through multiple PA measurements on different samples, we successfully obtained their optical properties, electronic properties, and thermal properties. Our conclusions were validated by comparison with results from applying other measurement methods on same samples.

Chapter 4 investigates the carrier dynamics in iodine-doped bromine-based perovskite single crystals. Through absorption, PL, X-ray diffraction, and X-ray rocking curve measurements, we verified the doping of iodine in $MAPbBr_3$ single crystals. Subsequently, through PL and time-resolved PL, we summarized the impact of iodine doping on the carrier recombination and trap state density of the single crystals. Our research contributes to a deeper understanding of mixed-halide perovskites.

Chapter 5 gives a summary of this thesis and provides the future development prospects of perovskite single crystals.

1.12 Bibliography

1. Hannah Ritchie, M. R. a. P. R. CO_2 and Greenhouse Gas Emissions.

2. Soga, T., Fundamentals of Solar Cell. *Nanostructured Materials for Solar Energy Conversion* **2006**.

3. Laboratory, N. R. E. Best Research-Cell Efficiency Chart.

4. Li, Z.; Yang, M.; Park, J.-S.; Wei, S.-H.; Berry, J. J.; Zhu, K., Stabilizing Perovskite Structures by Tuning Tolerance Factor: Formation of Formamidinium and Cesium Lead Iodide Solid-State Alloys. *Chem. Mater.* **2015,** *28* (1), 284-292.

5. Di, J.; Chang, J.; Liu, S., Recent progress of two-dimensional lead halide perovskite single crystals: Crystal growth, physical properties, and device applications. *EcoMat* **2020,** *2* (3).

6. Goldschmidt, V. M., Die Gesetze der Krystallochemie. *Naturwissenschaften* **1926,** *14*, 477-485.

7. Li, C.; Lu, X.; Ding, W.; Feng, L.; Gao, Y.; Guo, Z., Formability of ABX3 (X = F, Cl, Br, I) halide perovskites. *Acta Crystallogr B* **2008,** *64* (Pt 6), 702-7.

8. Fang, H. H.; Raissa, R.; Abdu-Aguye, M.; Adjokatse, S.; Blake, G. R.; Even, J.; Loi, M. A., Photophysics of Organic–Inorganic Hybrid Lead Iodide Perovskite Single Crystals. *Adv. Funct. Mater.* **2015,** *25* (16), 2378-2385.

9. Zhang, Y.; Liu, Y.; Liu, S., Composition Engineering of Perovskite Single Crystals for High-Performance Optoelectronics. *Adv. Funct. Mater.* **2022,** *33* (9).

10. Hoque, M. N.; Islam, N.; Li, Z.; Ren, G.; Zhu, K.; Fan, Z., Ionic and Optical Properties of Methylammonium Lead Iodide Perovskite across the Tetragonal-Cubic Structural Phase Transition. *ChemSusChem* **2016,** *9* (18), 2692-2698.

11. Quarti, C.; Mosconi, E.; Ball, J. M.; D'Innocenzo, V.; Tao, C.; Pathak, S.; Snaith, H. J.; Petrozza, A.; De Angelis, F., Structural and optical properties of methylammonium lead iodide across the tetragonal to cubic phase transition: implications for perovskite solar cells. *Energy & Environmental Science* **2016,** *9* (1), 155-163.

12. Han, Q.; Bae, S. H.; Sun, P.; Hsieh, Y. T.; Yang, Y. M.; Rim, Y. S.; Zhao, H.; Chen, Q.; Shi, W.; Li, G.; Yang, Y., Single Crystal Formamidinium Lead Iodide (FAPbI3): Insight into the Structural, Optical, and Electrical Properties. *Adv Mater* **2016,** *28* (11), 2253-8.

13. Rebecca J. Sutton, M. R. F., Amir A. Haghighirad, Nobuya Sakai, Bernard Wenger, Feliciano Giustino, and Henry J. Snaith, Cubic or Orthorhombic? Revealing the Crystal Structure of Metastable Black-Phase CsPbI3 by Theory and Experiment. *ACS Energy Lett.* **2018,** *3* (8), 1787-1794.

14. Jiang, J.; Xiong, M.; Fan, K.; Bao, C.; Xin, D.; Pan, Z.; Fei, L.; Huang, H.; Zhou, L.; Yao, K.; Zheng, X.; Shen, L.; Gao, F., Synergistic strain engineering of perovskite single crystals for highly stable and sensitive X-ray detectors with low-bias imaging and monitoring. *Nat. Photonics* **2022,** *16* (8), 575-581.

15. Liu, Y.; Zheng, X.; Fang, Y.; Zhou, Y.; Ni, Z.; Xiao, X.; Chen, S.; Huang, J., Ligand assisted growth of perovskite single crystals with low defect density. *Nat Commun* **2021,** *12* (1), 1686.

16. Saliba, M.; Matsui, T.; Seo, J. Y.; Domanski, K.; Correa-Baena, J. P.; Nazeeruddin, M. K.; Zakeeruddin, S. M.; Tress, W.; Abate, A.; Hagfeldt, A.; Gratzel, M., Cesium-containing triple cation perovskite solar cells: improved stability, reproducibility and high efficiency. *Energy Environ Sci* **2016,** *9* (6), 1989-1997.

17. Saliba, M.; Orlandi, S.; Matsui, T.; Aghazada, S.; Cavazzini, M.; Correa-Baena, J.-P.; Gao, P.; Scopelliti, R.; Mosconi, E.; Dahmen, K.-H.; De Angelis, F.; Abate, A.; Hagfeldt, A.; Pozzi, G.; Graetzel, M.; Nazeeruddin, M. K., A molecularly engineered hole-transporting material for efficient perovskite solar cells. *Nat. Energy* **2016,** *1* (2).

18. Gholipour, S.; Ali, A. M.; Correa-Baena, J. P.; Turren-Cruz, S. H.; Tajabadi, F.; Tress, W.; Taghavinia, N.; Gratzel, M.; Abate, A.; De Angelis, F.; Gaggioli, C. A.; Mosconi, E.; Hagfeldt, A.; Saliba, M., Globularity-Selected Large Molecules for a New Generation of Multication Perovskites. *Adv Mater* **2017,** *29* (38).

19. Chu, Z.; Zhao, Y.; Ma, F.; Zhang, C. X.; Deng, H.; Gao, F.; Ye, Q.; Meng, J.; Yin, Z.; Zhang, X.; You, J., Large cation ethylammonium incorporated perovskite for efficient and spectra stable blue light-emitting diodes. *Nat Commun* **2020,** *11* (1), 4165.

20. Stoddard, R. J.; Rajagopal, A.; Palmer, R. L.; Braly, I. L.; Jen, A. K. Y.; Hillhouse, H. W., Enhancing Defect Tolerance and Phase Stability of High-Bandgap Perovskites via Guanidinium Alloying. *ACS Energy Lett.* **2018,** *3* (6), 1261-1268.

21. Zhou, Y.; Xue, H.; Jia, Y. H.; Brocks, G.; Tao, S.; Zhao, N., Enhanced Incorporation of Guanidinium in Formamidinium-Based Perovskites for Efficient and Stable Photovoltaics: The Role of Cs and Br. *Adv. Funct. Mater.* **2019,** *29* (48).

22. Eperon, G. E.; Stone, K. H.; Mundt, L. E.; Schloemer, T. H.; Habisreutinger, S. N.; Dunfield, S. P.; Schelhas, L. T.; Berry, J. J.; Moore, D. T., The Role of Dimethylammonium in Bandgap Modulation for Stable Halide Perovskites. *ACS Energy Lett.* **2020,** *5* (6), 1856-1864.

23. Wang, Y.; Liu, X.; Zhang, T.; Wang, X.; Kan, M.; Shi, J.; Zhao, Y., The Role of Dimethylammonium Iodide in CsPbI(3) Perovskite Fabrication: Additive or Dopant? *Angew Chem Int Ed Engl* **2019,** *58* (46), 16691-16696.

24. Qiao, W. C.; Dong, W.; Fu, X. B.; Ma, K.; Liang, J. Q.; Wang, X. L.; Yao, Y. F., A-Site Mixing to Adjust the Photovoltaic Performance of a Double-Cation Perovskite: It Is Not Always the Simple Way. *J Phys Chem Lett* **2021,** *12* (45), 11206-11213.

25. Li, J.; Cao, H. L.; Jiao, W. B.; Wang, Q.; Wei, M.; Cantone, I.; Lu, J.; Abate, A., Biological impact of lead from halide perovskites reveals the risk of introducing a safe threshold. *Nat Commun* **2020,** *11* (1), 310.

26. Li, X.; Zhang, F.; He, H.; Berry, J. J.; Zhu, K.; Xu, T., On-device lead sequestration for perovskite solar cells. *Nature* **2020,** *578* (7796), 555-558.

27. Leijtens, T.; Prasanna, R.; Gold-Parker, A.; Toney, M. F.; McGehee, M. D., Mechanism of Tin Oxidation and Stabilization by Lead Substitution in Tin Halide Perovskites. *ACS Energy Lett.* **2017,** *2* (9), 2159-2165.

28. Tze-Bin Song, T. Y., Constantinos C. Stoumpos, Jenna Logsdon, Duyen H. Cao, Michael R. Wasielewski, Shinji Aramaki, and Mercouri G. Kanatzidis, Importance of Reducing Vapor Atmosphere in the Fabrication of Tin-Based Perovskite Solar Cells. *J. Am. Chem. Soc.* **2017,** *139* (2), 836-842.

29. Lee, B.; Stoumpos, C. C.; Zhou, N.; Hao, F.; Malliakas, C.; Yeh, C. Y.; Marks, T. J.; Kanatzidis, M. G.; Chang, R. P., Air-stable molecular semiconducting iodosalts for solar cell applications: Cs2SnI6 as a hole conductor. *J Am Chem Soc* **2014,** *136* (43), 15379-85.

30. Kumar, M. H.; Dharani, S.; Leong, W. L.; Boix, P. P.; Prabhakar, R. R.; Baikie, T.; Shi, C.; Ding, H.; Ramesh, R.; Asta, M.; Graetzel, M.; Mhaisalkar, S. G.; Mathews, N., Lead-free halide perovskite solar cells with high photocurrents realized through vacancy modulation. *Adv Mater* **2014,** *26* (41), 7122-7.

31. Chung, I.; Lee, B.; He, J.; Chang, R. P.; Kanatzidis, M. G., All-solid-state dye-sensitized solar cells with high efficiency. *Nature* **2012,** *485* (7399), 486-9.

32. Xu, Q.; Yang, D.; Lv, J.; Sun, Y. Y.; Zhang, L., Perovskite Solar Absorbers: Materials by Design. *Small Methods* **2018,** *2* (5).

33. Tai, Q.; Guo, X.; Tang, G.; You, P.; Ng, T. W.; Shen, D.; Cao, J.; Liu, C. K.; Wang, N.; Zhu, Y.; Lee, C. S.; Yan, F., Antioxidant Grain Passivation for Air-Stable Tin-Based Perovskite Solar Cells. *Angew Chem Int Ed Engl* **2019,** *58* (3), 806-810.

34. Wang, C.; Gu, F.; Zhao, Z.; Rao, H.; Qiu, Y.; Cai, Z.; Zhan, G.; Li, X.; Sun, B.; Yu, X.; Zhao, B.; Liu, Z.; Bian, Z.; Huang, C., Self-Repairing Tin-Based Perovskite Solar Cells with a Breakthrough Efficiency Over 11. *Adv Mater* **2020,** *32* (31), e1907623.

35. Hao, F.; Stoumpos, C. C.; Guo, P.; Zhou, N.; Marks, T. J.; Chang, R. P.; Kanatzidis, M. G., Solvent-Mediated Crystallization of CH3NH3SnI3 Films for Heterojunction Depleted Perovskite Solar Cells. *J Am Chem Soc* **2015,** *137* (35), 11445-52.

36. Umari, P.; Mosconi, E.; De Angelis, F., Relativistic GW calculations on CH3NH3PbI3 and CH3NH3SnI3 perovskites for solar cell applications. *Sci Rep* **2014,** *4*, 4467.

37. Stoumpos, C. C.; Malliakas, C. D.; Kanatzidis, M. G., Semiconducting tin and lead iodide perovskites with organic cations: phase transitions, high mobilities, and near-infrared photoluminescent properties. *Inorg Chem* **2013,** *52* (15), 9019-38.

38. Shockley, W.; Queisser, H. J., Detailed Balance Limit of Efficiency of p-n Junction Solar Cells. *J. Appl. Phys.* **1961,** *32* (3), 510-519.

39. Hao, F.; Stoumpos, C. C.; Chang, R. P.; Kanatzidis, M. G., Anomalous band gap behavior in mixed Sn and Pb perovskites enables broadening of absorption spectrum in solar cells. *J Am Chem Soc* **2014,** *136* (22), 8094-9.

40. Giles E. Eperon, T. L., Kevin A. Bush, Rohit Prasanna, Thomas Green, Jacob Tse-Wei Wang, David P. McMeekin, George Volonakis, Rebecca L. Milot, Richard May, Axel Palmstrom, Daniel J. Slotcavage, Rebecca A. Belisle, Jay B. Patel, Elizabeth S. Parrott, Rebecca J. Sutton, Wen Ma, Farhad Moghadam, Bert Conings, Aslihan Babayigit, Hans-Gerd Boyen, Stacey Bent, Feliciano Giustino, Laura M. Herz, Michael B. Johnston, Michael D. McGehee, Henry J. Snaith, Perovskite-perovskite tandem photovoltaics with optimized band gaps. *Science* **2016,** *354* (6314), 861-865.

41. Liao, W.; Zhao, D.; Yu, Y.; Shrestha, N.; Ghimire, K.; Grice, C. R.; Wang, C.; Xiao, Y.; Cimaroli, A. J.; Ellingson, R. J.; Podraza, N. J.; Zhu, K.; Xiong, R. G.; Yan, Y., Fabrication of Efficient Low-Bandgap Perovskite Solar Cells by Combining Formamidinium Tin Iodide with Methylammonium Lead Iodide. *J Am Chem Soc* **2016,** *138* (38), 12360-3.

42. Klug, M. T.; Milot, R. L.; Patel, J. B.; Green, T.; Sansom, H. C.; Farrar, M. D.; Ramadan, A. J.; Martani, S.; Wang, Z.; Wenger, B.; Ball, J. M.; Langshaw, L.; Petrozza, A.; Johnston, M. B.; Herz, L. M.; Snaith, H. J., Metal composition influences optoelectronic quality in mixed-metal lead–tin triiodide perovskite solar absorbers. *Energy & Environmental Science* **2020,** *13* (6), 1776-1787.

43. Rajagopal, A.; Stoddard, R. J.; Hillhouse, H. W.; Jen, A. K. Y., On understanding bandgap bowing and optoelectronic quality in Pb–Sn alloy hybrid perovskites. *J. Mater. Chem. A* **2019,** *7* (27), 16285-16293.

44. Khatun, S.; Maiti, A.; Pal, A. J., Bowing of transport gap in hybrid halide perovskite alloys (CH3NH3Sn1−xPbxI3): Which band is responsible? *Applied Physics Letters* **2020,** *116* (1).

45. Goyal, A.; McKechnie, S.; Pashov, D.; Tumas, W.; van Schilfgaarde, M.; Stevanović, V., Origin of Pronounced Nonlinear Band Gap Behavior in Lead–Tin Hybrid Perovskite Alloys. *Chem. Mater.* **2018,** *30* (11), 3920-3928.

46. Valadares, F.; Guilhon, I.; Teles, L. K.; Marques, M., Atomistic Origins of Enhanced Band Gap, Miscibility, and Oxidation Resistance in α-CsPb1–xSnxI3 Mixed Perovskite. *The Journal of Physical Chemistry C* **2020,** *124* (48), 26124-26133.

47. Gao, Q.; Sahin, H.; Kang, J.; Wei, S.-H., Origin of anomalous band-gap bowing in two-dimensional tin-lead mixed perovskite alloys. *Physical Review B* **2021,** *104* (6).

48. Swarnkar, A.; Mir, W. J.; Nag, A., Can B-Site Doping or Alloying Improve Thermal- and Phase-Stability of All-Inorganic CsPbX3 (X = Cl, Br, I) Perovskites? *ACS Energy Lett.* **2018,** *3* (2), 286-289.

49. Hao, F.; Stoumpos, C. C.; Cao, D. H.; Chang, R. P. H.; Kanatzidis, M. G., Lead-free solid-state organic–inorganic halide perovskite solar cells. *Nat. Photonics* **2014,** *8* (6), 489-494.

50. Noel, N. K.; Stranks, S. D.; Abate, A.; Wehrenfennig, C.; Guarnera, S.; Haghighirad, A.-A.; Sadhanala, A.; Eperon, G. E.; Pathak, S. K.; Johnston, M. B.; Petrozza, A.; Herz, L. M.; Snaith, H. J., Lead-free organic–inorganic tin halide perovskites for photovoltaic applications. *Energy Environ. Sci.* **2014,** *7* (9), 3061-3068.

51. Yu, B. B.; Chen, Z.; Zhu, Y.; Wang, Y.; Han, B.; Chen, G.; Zhang, X.; Du, Z.; He, Z., Heterogeneous 2D/3D Tin-Halides Perovskite Solar Cells with Certified Conversion Efficiency Breaking 14. *Adv Mater* **2021,** *33* (36), e2102055.

52. Jiang, X.; Li, H.; Zhou, Q.; Wei, Q.; Wei, M.; Jiang, L.; Wang, Z.; Peng, Z.; Wang, F.; Zang, Z.; Xu, K.; Hou, Y.; Teale, S.; Zhou, W.; Si, R.; Gao, X.; Sargent, E. H.; Ning, Z., One-Step Synthesis of SnI(2).(DMSO)(x) Adducts for High-Performance Tin Perovskite Solar Cells. *J Am Chem Soc* **2021,** *143* (29), 10970-10976.

53. Wang, M.; Wang, W.; Ma, B.; Shen, W.; Liu, L.; Cao, K.; Chen, S.; Huang, W., Lead-Free Perovskite Materials for Solar Cells. *Nanomicro Lett* **2021,** *13* (1), 62.

54. Protesescu, L.; Yakunin, S.; Bodnarchuk, M. I.; Krieg, F.; Caputo, R.; Hendon, C. H.; Yang, R. X.; Walsh, A.; Kovalenko, M. V., Nanocrystals of Cesium Lead Halide Perovskites (CsPbX(3), X = Cl, Br, and I): Novel Optoelectronic Materials Showing Bright Emission with Wide Color Gamut. *Nano Lett* **2015,** *15* (6), 3692-6.

55. Cheng, Z.; Liu, K.; Yang, J.; Chen, X.; Xie, X.; Li, B.; Zhang, Z.; Liu, L.; Shan, C.; Shen, D., High-Performance Planar-Type Ultraviolet Photodetector Based on High-Quality CH(3)NH(3)PbCl(3) Perovskite Single Crystals. *ACS Appl Mater Interfaces* **2019,** *11* (37), 34144-34150.

56. Chen, Z.; Turedi, B.; Alsalloum, A. Y.; Yang, C.; Zheng, X.; Gereige, I.; AlSaggaf, A.; Mohammed, O. F.; Bakr, O. M., Single-Crystal MAPbI3 Perovskite Solar Cells Exceeding 21% Power Conversion Efficiency. *ACS Energy Lett.* **2019,** *4* (6), 1258-1259.

57. Akihiro Kojima, K. T., Yasuo Shirai, and Tsutomu Miyasaka, Organometal Halide Perovskites as Visible-Light Sensitizers for Photovoltaic Cells. *J. Am. Chem. Soc.* **2009,** *131* (17), 6050–6051.

58. MICHAEL M. LEE, J. T., TSUTOMU MIYASAKA, TAKUROU N. MURAKAMI, AND HENRY J. SNAITH, Efficient Hybrid Solar Cells Based on Meso-Superstructured Organometal Halide Perovskites. *Science* **2012,** *338* (6107), 643-647.

59. Chae, J.; Dong, Q.; Huang, J.; Centrone, A., Chloride Incorporation Process in CH(3)NH(3)PbI(3-x)Cl(x) Perovskites via Nanoscale Bandgap Maps. *Nano Lett* **2015,** *15* (12), 8114-21.

60. Chen, Q.; Zhou, H.; Fang, Y.; Stieg, A. Z.; Song, T. B.; Wang, H. H.; Xu, X.; Liu, Y.; Lu, S.; You, J.; Sun, P.; McKay, J.; Goorsky, M. S.; Yang, Y., The optoelectronic role of chlorine in CH3NH3PbI3(Cl)-based perovskite solar cells. *Nat Commun* **2015,** *6*, 7269.

61. Lian, Z.; Yan, Q.; Gao, T.; Ding, J.; Lv, Q.; Ning, C.; Li, Q.; Sun, J. L., Perovskite CH3NH3PbI3(Cl) Single Crystals: Rapid Solution Growth, Unparalleled Crystalline Quality, and Low Trap Density toward 10(8) cm(-3). *J. Am. Chem. Soc.* **2016,** *138* (30), 9409-12.

62. Liu, N.; Wang, L.; Xu, F.; Wu, J.; Song, T.; Chen, Q., Recent Progress in Developing Monolithic Perovskite/Si Tandem Solar Cells. *Front Chem* **2020,** *8*, 603375.

63. A. SHAH, P. T., R. TSCHARNER, N. WYRSCH, AND H. KEPPNER, Photovoltaic Technology: The Case for Thin-Film Solar Cells. *Science* **1999,** *285* (5428), 692-698.

64. Mahesh, S.; Ball, J. M.; Oliver, R. D. J.; McMeekin, D. P.; Nayak, P. K.; Johnston, M. B.; Snaith, H. J., Revealing the origin of voltage loss in mixed-halide perovskite solar cells. *Energy & Environmental Science* **2020,** *13* (1), 258-267.

65. Zhou, Y.; van Laar, S. C. W.; Meggiolaro, D.; Gregori, L.; Martani, S.; Heng, J. Y.; Datta, K.; Jimenez-Lopez, J.; Wang, F.; Wong, E. L.; Poli, I.; Treglia, A.; Cortecchia, D.; Prato, M.; Kobera, L.; Gao, F.; Zhao, N.; Janssen, R. A. J.; De Angelis, F.; Petrozza, A., How Photogenerated I(2) Induces I-rich Phase Formation in Lead Mixed Halide Perovskites. *Adv Mater* **2023**, e2305567.

66. Khirade, P. P.; Birajdar, S. D.; Raut, A. V.; Jadhav, K. M., Multiferroic iron doped BaTiO3 nanoceramics synthesized by sol-gel auto combustion: Influence of iron on physical properties. *Ceramics International* **2016,** *42* (10), 12441-12451.

67. H. Iwahara, T. Y., T. Hibino, K. Ozaki, H. Suzuki, Protonic conduction in calcium, strontium and barium zirconates. *Solid State Ionics* **1993,** *61*, 65-69.

68. Choi, K. J.; Biegalski, M.; Li, Y. L.; Sharan, A.; Schubert, J.; Uecker, R.; Reiche, P.; Chen, Y. B.; Pan, X. Q.; Gopalan, V.; Chen, L. Q.; Schlom, D. G.; Eom, C. B., Enhancement of ferroelectricity in strained BaTiO3 thin films. *Science* **2004,** *306* (5698), 1005-9.

69. Xing, J.; Liu, X. F.; Zhang, Q.; Ha, S. T.; Yuan, Y. W.; Shen, C.; Sum, T. C.; Xiong, Q., Vapor Phase Synthesis of Organometal Halide Perovskite Nanowires for Tunable Room-Temperature Nanolasers. *Nano Lett* **2015,** *15* (7), 4571-7.

70. Alexe, M.; Hesse, D.; Schmidt, V.; Senz, S.; Fan, H. J.; Zacharias, M.; Gösele, U., Ferroelectric nanotubes fabricated using nanowires as positive templates. *Applied Physics Letters* **2006,** *89* (17).

71. Parizi, S. S.; Mellinger, A.; Caruntu, G., Ferroelectric barium titanate nanocubes as capacitive building blocks for energy storage applications. *ACS Appl Mater Interfaces* **2014,** *6* (20), 17506-17.

72. Morozovska, A. N.; Eliseev, E. A.; Glinchuk, M. D., Ferroelectricity enhancement in confined nanorods: Direct variational method. *Physical Review B* **2006,** *73* (21).

73. Gonzalez-Carrero, S.; Galian, R. E.; Pérez-Prieto, J., Maximizing the emissive properties of CH3NH3PbBr3 perovskite nanoparticles. *J. Mater. Chem. A* **2015,** *3* (17), 9187-9193.

74. Tan, Z. K.; Moghaddam, R. S.; Lai, M. L.; Docampo, P.; Higler, R.; Deschler, F.; Price, M.; Sadhanala, A.; Pazos, L. M.; Credgington, D.; Hanusch, F.; Bein, T.; Snaith, H. J.; Friend, R. H., Bright light-emitting diodes based on organometal halide perovskite. *Nat Nanotechnol* **2014,** *9* (9), 687-92.

75. Shirasaki, Y.; Supran, G. J.; Bawendi, M. G.; Bulović, V., Emergence of colloidal quantum-dot light-emitting technologies. *Nat. Photonics* **2012,** *7* (1), 13-23.

76. Caruge, J. M.; Halpert, J. E.; Wood, V.; Bulović, V.; Bawendi, M. G., Colloidal quantum-dot light-emitting diodes with metal-oxide charge transport layers. *Nat. Photonics* **2008,** *2* (4), 247-250.

77. Seo, H. K.; Kim, H.; Lee, J.; Park, M. H.; Jeong, S. H.; Kim, Y. H.; Kwon, S. J.; Han, T. H.; Yoo, S.; Lee, T. W., Efficient Flexible Organic/Inorganic Hybrid Perovskite Light-Emitting Diodes Based on Graphene Anode. *Adv Mater* **2017,** *29* (12).

78. Peng, L.; Geng, J.; Ai, L.; Zhang, Y.; Xie, R.; Yang, W., Room temperature synthesis of ultra-small, near-unity single-sized lead halide perovskite quantum dots with wide color emission tunability, high color purity and high brightness. *Nanotechnology* **2016,** *27* (33), 335604.

79. Choon, S. L.; Lim, H. N.; Ibrahim, I.; Zainal, Z.; Tan, K. B.; Foo, C. Y.; Ng, C. H., New potential materials in advancement of photovoltaic and optoelectronic applications: Metal halide perovskite nanorods. *Renewable and Sustainable Energy Reviews* **2023,** *171*.

80. D. B. Mitzi, K. C. a. C. R. K., Organic-inorganic electronics. *IBM Journal of Research and Development* **2001,** *45* (1).

81. Im, J.-H.; Kim, H.-S.; Park, N.-G., Morphology-photovoltaic property correlation in perovskite solar cells: One-step versus two-step deposition of CH3NH3PbI3. *APL Mater.* **2014,** *2* (8).

82. Dunlap-Shohl, W. A.; Zhou, Y.; Padture, N. P.; Mitzi, D. B., Synthetic Approaches for Halide Perovskite Thin Films. *Chem Rev* **2019,** *119* (5), 3193-3295.

83. Dai, Q.; Chen, X.; Ding, R.; Peng, Y.; Lv, W.; Zhou, Z.; Xu, S.; Sun, L., Electrode material and modification dependent performances of lateral photodetectors based on MAPbI3 single crystal. *Optical Materials* **2021,** *111*.

84. Wang, K.; Jing, L.; Yao, Q.; Zhang, J.; Cheng, X.; Yuan, Y.; Shang, C.; Ding, J.; Zhou, T.; Sun, H.; Zhang, W.; Li, H., Highly In-Plane Polarization-Sensitive Photodetection in CsPbBr(3) Single Crystal. *J Phys Chem Lett* **2021,** *12* (7), 1904-1910.

85. Liao, M.; Xia, M.; Xu, Y.; Lu, P.; Niu, G., Growth mechanism of metal halide perovskite single crystals in solution. *Chem Commun (Camb)* **2023,** *59* (57), 8758-8768.

86. Binsbergen, F. L., Natural and artificial heterogeneous nucleation in polymer crystallization. *Journal of Polymer Science: Polymer Symposia* **1977,** *59*, 11-29.

87. Avrami, M., Kinetics of Phase Change. II Transformation-Time Relations for Random Distribution of Nuclei. *The Journal of Chemical Physics* **1940,** *8* (2), 212-224.

88. Dinegar, V. K. L. a. R. H., Theory, Production and Mechanism of Formation of Monodispersed Hydrosols. *J. Am. Chem. Soc.* **1950,** *72* (11), 4847-4854.

89. Zhumekenov, A. A.; Burlakov, V. M.; Saidaminov, M. I.; Alofi, A.; Haque, M. A.; Turedi, B.; Davaasuren, B.; Dursun, I.; Cho, N.; El-Zohry, A. M.; De Bastiani, M.; Giugni, A.; Torre, B.; Di Fabrizio, E.; Mohammed, O. F.; Rothenberger, A.; Wu, T.; Goriely, A.; Bakr, O. M., The Role of Surface Tension in the Crystallization of Metal Halide Perovskites. *ACS Energy Lett.* **2017,** *2* (8), 1782-1788.

90. Singh, M. R.; Ramkrishna, D., Dispersions in crystal nucleation and growth rates: Implications of fluctuation in supersaturation. *Chemical Engineering Science* **2014,** *107*, 102-113.

91. Chakraborty, D.; Patey, G. N., Evidence that crystal nucleation in aqueous NaCl solution Occurs by the two-step mechanism. *Chemical Physics Letters* **2013,** *587*, 25-29.

92. Wang, K.; Wu, C.; Yang, D.; Jiang, Y.; Priya, S., Quasi-Two-Dimensional Halide Perovskite Single Crystal Photodetector. *ACS Nano* **2018,** *12* (5), 4919-4929.

93. Poglitsch, A.; Weber, D., Dynamic disorder in methylammoniumtrihalogenoplumbates (II) observed by millimeter-wave spectroscopy. *J. Chem. Phys.* **1987,** *87* (11), 6373-6378.

94. Lian, Z.; Yan, Q.; Lv, Q.; Wang, Y.; Liu, L.; Zhang, L.; Pan, S.; Li, Q.; Wang, L.; Sun, J. L., High-Performance Planar-Type Photodetector on (100) Facet of MAPbI3 Single Crystal. *Sci Rep* **2015,** *5*, 16563.

95. Dong, Q.; Fang, Y.; Shao, Y.; Mulligan, P.; Qiu, J.; Cao, L.; Huang, J., Electron-hole diffusion lengths > 175 mum in solution-grown CH3NH3PbI3 single crystals. *Science* **2015,** *347* (6225), 967-70.

96. Shi, D.; Adinolfi, V.; Comin, R.; Yuan, M.; Alarousu, E.; Buin, A.; Chen, Y.; Hoogland, S.; Rothenberger, A.; Katsiev, K.; Losovyj, Y.; Zhang, X.; Dowben, P. A.; Mohammed, O. F.; Sargent, E. H.; Bakr, O. M., Low trap-state density and long carrier diffusion in organolead trihalide perovskite single crystals. *Science* **2015,** *347* (6221), 519-22.

97. Tidhar, Y.; Edri, E.; Weissman, H.; Zohar, D.; Hodes, G.; Cahen, D.; Rybtchinski, B.; Kirmayer, S., Crystallization of methyl ammonium lead halide perovskites: implications for photovoltaic applications. *J Am Chem Soc* **2014,** *136* (38), 13249-56.

98. Yang, Y.; Yan, Y.; Yang, M.; Choi, S.; Zhu, K.; Luther, J. M.; Beard, M. C., Low surface recombination velocity in solution-grown CH3NH3PbBr3 perovskite single crystal. *Nat. Commun.* **2015,** *6*, 7961.

99. Liu, X.; Zhang, H.; Zhang, B.; Dong, J.; Jie, W.; Xu, Y., Charge Transport Behavior in Solution-Grown Methylammonium Lead Tribromide Perovskite Single Crystal Using α Particles. *The Journal of Physical Chemistry C* **2018,** *122* (26), 14355-14361.

100. Liu, F.; Wang, F.; Hansen, K. R.; Zhu, X. Y., Bimodal Bandgaps in Mixed Cesium Methylammonium Lead Bromide Perovskite Single Crystals. *The Journal of Physical Chemistry C* **2019,** *123* (23), 14865-14870.

101. Saidaminov, M. I.; Abdelhady, A. L.; Maculan, G.; Bakr, O. M., Retrograde solubility of formamidinium and methylammonium lead halide perovskites enabling rapid single crystal growth. *Chem Commun (Camb)* **2015,** *51* (100), 17658-61.

102. Saidaminov, M. I.; Abdelhady, A. L.; Murali, B.; Alarousu, E.; Burlakov, V. M.; Peng, W.; Dursun, I.; Wang, L.; He, Y.; Maculan, G.; Goriely, A.; Wu, T.; Mohammed, O. F.; Bakr, O. M., High-quality bulk hybrid perovskite single crystals within minutes by inverse temperature crystallization. *Nat. Commun.* **2015,** *6*, 7586.

103. Liu, Y.; Yang, Z.; Cui, D.; Ren, X.; Sun, J.; Liu, X.; Zhang, J.; Wei, Q.; Fan, H.; Yu, F.; Zhang, X.; Zhao, C.; Liu, S. F., Two-Inch-Sized Perovskite CH3 NH3 PbX3 (X = Cl, Br, I) Crystals: Growth and Characterization. *Adv Mater* **2015,** *27* (35), 5176-83.

104. Liu, X.; Xu, M.; Hao, Y.; Fu, J.; Wang, F.; Zhang, B.; Bennett, S.; Sellin, P.; Jie, W.; Xu, Y., Solution-Grown Formamidinium Hybrid Perovskite (FAPbBr(3)) Single Crystals for alpha-Particle and gamma-Ray Detection at Room Temperature. *ACS Appl Mater Interfaces* **2021,** *13* (13), 15383-15390.

105. Liu, Y.; Zhang, Y.; Yang, Z.; Feng, J.; Xu, Z.; Li, Q.; Hu, M.; Ye, H.; Zhang, X.; Liu, M.; Zhao, K.; Liu, S., Low-temperature-gradient crystallization for multi-inch high-quality perovskite single crystals for record performance photodetectors. *Mater. Today* **2019,** *22*, 67-75.

106. Min-Hyun Sunga , J.-S. K., Woon-Soo Kimc , Izumi Hirasawac, Woo-Sik Kim, Modification of crystal growth mechanism of yttrium oxalate in metastable solution. *J. Cryst. Growth* **2002,** *235* (1-4), 529-540.

107. Yao, F.; Peng, J.; Li, R.; Li, W.; Gui, P.; Li, B.; Liu, C.; Tao, C.; Lin, Q.; Fang, G., Room-temperature liquid diffused separation induced crystallization for high-quality perovskite single crystals. *Nat Commun* **2020,** *11* (1), 1194.

108. Ma, L.; Yan, Z.; Zhou, X.; Pi, Y.; Du, Y.; Huang, J.; Wang, K.; Wu, K.; Zhuang, C.; Han, X., A polymer controlled nucleation route towards the generalized growth of organic-inorganic perovskite single crystals. *Nat Commun* **2021,** *12* (1), 2023.

109. Liu, Y.; Zhang, Y.; Yang, Z.; Yang, D.; Ren, X.; Pang, L.; Liu, S. F., Thinness- and Shape-Controlled Growth for Ultrathin Single-Crystalline Perovskite Wafers for Mass Production of Superior Photoelectronic Devices. *Adv. Mater.* **2016,** *28* (41), 9204-9209.

110. Rao, H. S.; Li, W. G.; Chen, B. X.; Kuang, D. B.; Su, C. Y., In Situ Growth of 120 cm(2) CH(3) NH(3) PbBr(3) Perovskite Crystal Film on FTO Glass for Narrowband-Photodetectors. *Adv Mater* **2017,** *29* (16).

111. Chen, Z.; Dong, Q.; Liu, Y.; Bao, C.; Fang, Y.; Lin, Y.; Tang, S.; Wang, Q.; Xiao, X.; Bai, Y.; Deng, Y.; Huang, J., Thin single crystal perovskite solar cells to harvest below-bandgap light absorption. *Nat Commun* **2017,** *8* (1), 1890.

112. Alsalloum, A. Y.; Turedi, B.; Almasabi, K.; Zheng, X.; Naphade, R.; Stranks, S. D.; Mohammed, O. F.; Bakr, O. M., 22.8%-Efficient single-crystal mixed-cation inverted perovskite solar cells with a near-optimal bandgap. *Energy & Environmental Science* **2021,** *14* (4), 2263-2268.

113. Schlipf, J.; Askar, A. M.; Pantle, F.; Wiltshire, B. D.; Sura, A.; Schneider, P.; Huber, L.; Shankar, K.; Muller-Buschbaum, P., Top-Down Approaches Towards Single Crystal Perovskite Solar Cells. *Sci Rep* **2018,** *8* (1), 4906.

114. Liu, Y.; Sun, J.; Yang, Z.; Yang, D.; Ren, X.; Xu, H.; Yang, Z.; Liu, S., 20-mm-Large Single-Crystalline Formamidinium-Perovskite Wafer for Mass Production of Integrated Photodetectors. *Advanced Optical Materials* **2016,** *4* (11), 1829-1837.

115. Peng, W.; Wang, L.; Murali, B.; Ho, K. T.; Bera, A.; Cho, N.; Kang, C. F.; Burlakov, V. M.; Pan, J.; Sinatra, L.; Ma, C.; Xu, W.; Shi, D.; Alarousu, E.; Goriely, A.; He, J. H.; Mohammed, O. F.; Wu, T.; Bakr, O. M., Solution-Grown Monocrystalline Hybrid Perovskite Films for Hole-Transporter-Free Solar Cells. *Adv Mater* **2016,** *28* (17), 3383-90.

116. Chen, Y.; Lei, Y.; Li, Y.; Yu, Y.; Cai, J.; Chiu, M. H.; Rao, R.; Gu, Y.; Wang, C.; Choi, W.; Hu, H.; Wang, C.; Li, Y.; Song, J.; Zhang, J.; Qi, B.; Lin, M.; Zhang, Z.; Islam, A. E.; Maruyama, B.; Dayeh, S.; Li, L. J.; Yang, K.; Lo, Y. H.; Xu, S., Strain engineering and epitaxial stabilization of halide perovskites. *Nature* **2020,** *577* (7789), 209-215.

117. Lei, Y.; Chen, Y.; Zhang, R.; Li, Y.; Yan, Q.; Lee, S.; Yu, Y.; Tsai, H.; Choi, W.; Wang, K.; Luo, Y.; Gu, Y.; Zheng, X.; Wang, C.; Wang, C.; Hu, H.; Li, Y.; Qi, B.; Lin, M.; Zhang, Z.; Dayeh, S. A.; Pharr, M.; Fenning, D. P.; Lo, Y. H.; Luo, J.; Yang, K.; Yoo, J.; Nie, W.; Xu, S., A fabrication process for flexible single-crystal perovskite devices. *Nature* **2020,** *583* (7818), 790-795.

118. Murgulov, V.; Daub, M.; Hillebrecht, H.; Fiederle, M.; Franc, J.; Dědič, V., Growth and Characterization of Radiation Sensors Based on Single Crystals of Hybrid Metal–Organic Methylammonium Lead Bromide and Iodide Perovskite. *Crystal Research and Technology* **2020,** *55* (11).

119. Yangyang Dang, Y. L., Youxuan Sun, Dongsheng Yuan, Xiaolong Liu, Weiqun Lu, Guangfeng Liu, Haibing Xia and Xutang Tao, Bulk crystal growth of hybrid perovskite material CH3NH3PbI3. *CrystEngComm* **2015,** *17* (3), 665-670.

120. Huang, J.; Yuan, Y.; Shao, Y.; Yan, Y., Understanding the physical properties of hybrid perovskites for photovoltaic applications. *Nature Reviews Materials* **2017,** *2* (7).

121. Ma, C.; Park, N.-G., A Realistic Methodology for 30% Efficient Perovskite Solar Cells. *Chem* **2020,** *6* (6), 1254-1264.

122. Wu, B.; Nguyen, H. T.; Ku, Z.; Han, G.; Giovanni, D.; Mathews, N.; Fan, H. J.; Sum, T. C., Discerning the Surface and Bulk Recombination Kinetics of Organic-Inorganic Halide Perovskite Single Crystals. *Adv. Energy Mater.* **2016,** *6* (14).

123. Wenger, B.; Nayak, P. K.; Wen, X.; Kesava, S. V.; Noel, N. K.; Snaith, H. J., Consolidation of the optoelectronic properties of CH(3)NH(3)PbBr(3) perovskite single crystals. *Nat Commun* **2017,** *8* (1), 590.

124. Wehrenfennig, C.; Liu, M.; Snaith, H. J.; Johnston, M. B.; Herz, L. M., Charge carrier recombination channels in the low-temperature phase of organic-inorganic lead halide perovskite thin films. *APL Mater.* **2014,** *2* (8).

125. Hutter, E. M.; Gelvez-Rueda, M. C.; Osherov, A.; Bulovic, V.; Grozema, F. C.; Stranks, S. D.; Savenije, T. J., Direct-indirect character of the bandgap in methylammonium lead iodide perovskite. *Nat Mater* **2017,** *16* (1), 115-120.

126. Shi, J.; Zhang, H.; Li, Y.; Jasieniak, J. J.; Li, Y.; Wu, H.; Luo, Y.; Li, D.; Meng, Q., Identification of high-temperature exciton states and their phase-dependent trapping behaviour in lead halide perovskites. *Energy & Environmental Science* **2018,** *11* (6), 1460-1469.

127. Liu, Y.; Dong, Q.; Fang, Y.; Lin, Y.; Deng, Y.; Huang, J., Fast Growth of Thin MAPbI3 Crystal Wafers on Aqueous Solution Surface for Efficient Lateral-Structure Perovskite Solar Cells. *Adv. Funct. Mater.* **2019,** *29* (47).

128. Xie, C.; Liu, C. K.; Loi, H. L.; Yan, F., Perovskite-Based Phototransistors and Hybrid Photodetectors. *Adv. Funct. Mater.* **2019,** *30* (20).

Chapter 2. Measurement and characterization

2.1 X-Ray Diffraction

X-Ray Diffraction (XRD) is a measuring technique for analyzing crystalline materials, through which information such as the phase composition, lattice constants, crystalline orientation, and structural strain of a crystal can be obtained. XRD measurement is a method based on the interaction between X-rays and the crystal lattice. When the spacing between crystal planes is

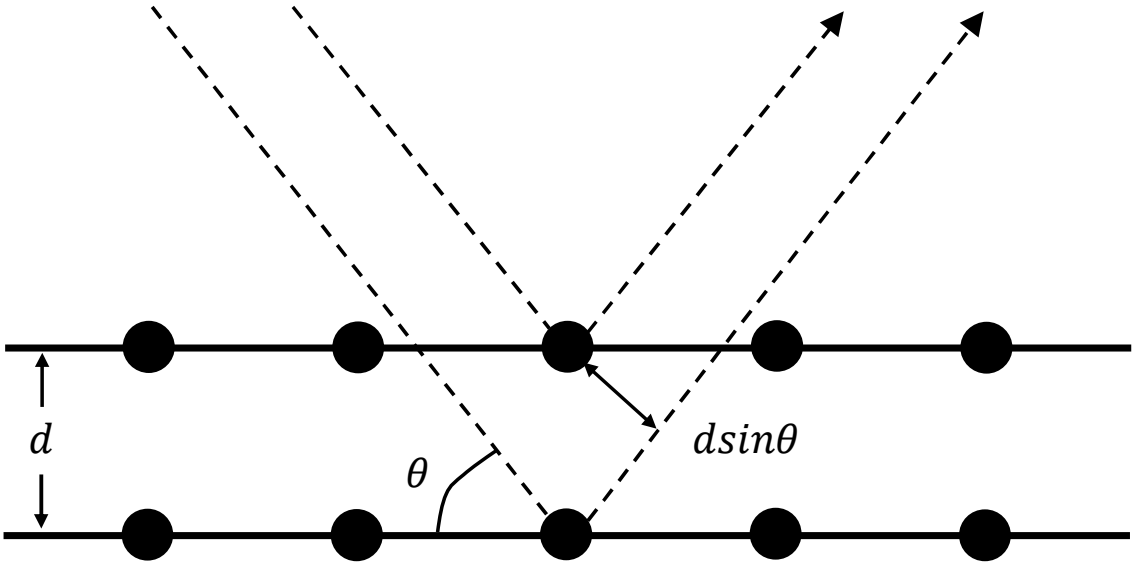

Figure 2-1. The pattern diagram of the Bragg equation.

similar to the wavelength of X-rays, the lattice can act as a diffraction grating for X-rays. When X-rays are irradiated onto the lattice, diffraction waves are formed, with some directions reinforcing each other and others weakening, resulting in the formation of an XRD pattern. In 1913, British scientists, the father and son Bragg, proposed the classic crystal diffraction formula known as the Bragg equation, building upon the discoveries in Laue's experiment. In 1913, the British scientists William Lawrence Bragg and his father William Henry Bragg proposed classic crystal diffraction formula known as the Bragg equation as shown in Fig.2-1:

$$2dsin\theta = n\lambda \qquad (2-1)$$

where d is the lattice constant, θ represents the angle between the incident X-ray and the corresponding crystal plane, λ is the wavelength of the incident X-ray, n is the diffraction order. In this experiment, we utilize powder X-ray diffraction patterns to determine the phase of the crystal. The XRD patterns were obtained by the Rigaku Ultima III X-ray diffractometer with monochromatic Cu Kα irradiation.

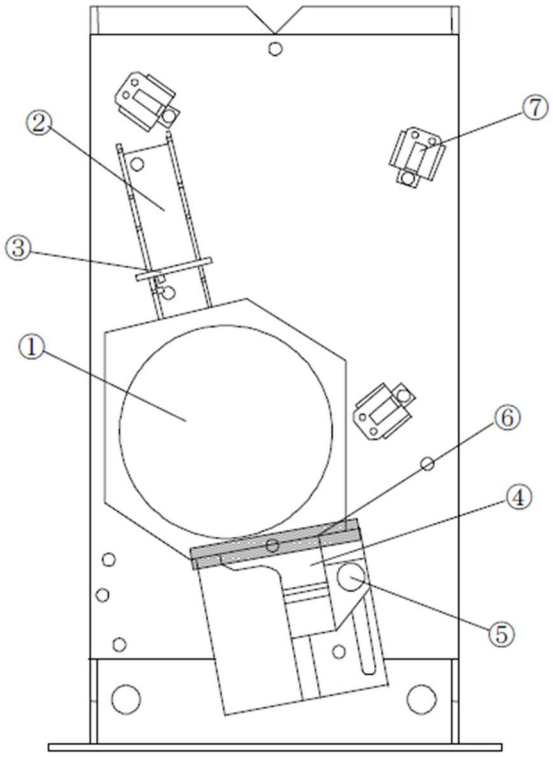

Figure 2-2. Diagram of the interior mode of an integrating sphere. ① Integrating sphere body, ② and ④ cell holders for different modes, ③ baffle for adjusting the optical path, ⑤ screws for fixation, ⑥ adapter position, ⑦ mirror.

2.2 X-Ray rocking curve

X-Ray rocking curve (XRC) is a technique derived from XRD measurement, which is used to describe the angular divergence of a specific crystal plane. In this measurement, a specific angle between crystal planes is selected, and the X-ray incident angle is varied positively and negatively

based on this angle. The graph displays the angle between the crystal plane and the X-ray on the horizontal axis, ranging from positive θ to negative θ. Positive θ represents counterclockwise rotation of the X-ray from the standard angle, while negative θ represents clockwise rotation of the X-ray from the standard angle. So, for an individual crystal plane, the lower the intensity of the corresponding angles around the standard angle, the weaker its angular divergence. This confirms that the arrangement of this crystal plane is very regular, almost growing in the same direction, and also indicates its excellent crystallinity. We also utilized the aforementioned XRD apparatus to compare the crystallinity of single crystals through XRC measurements.

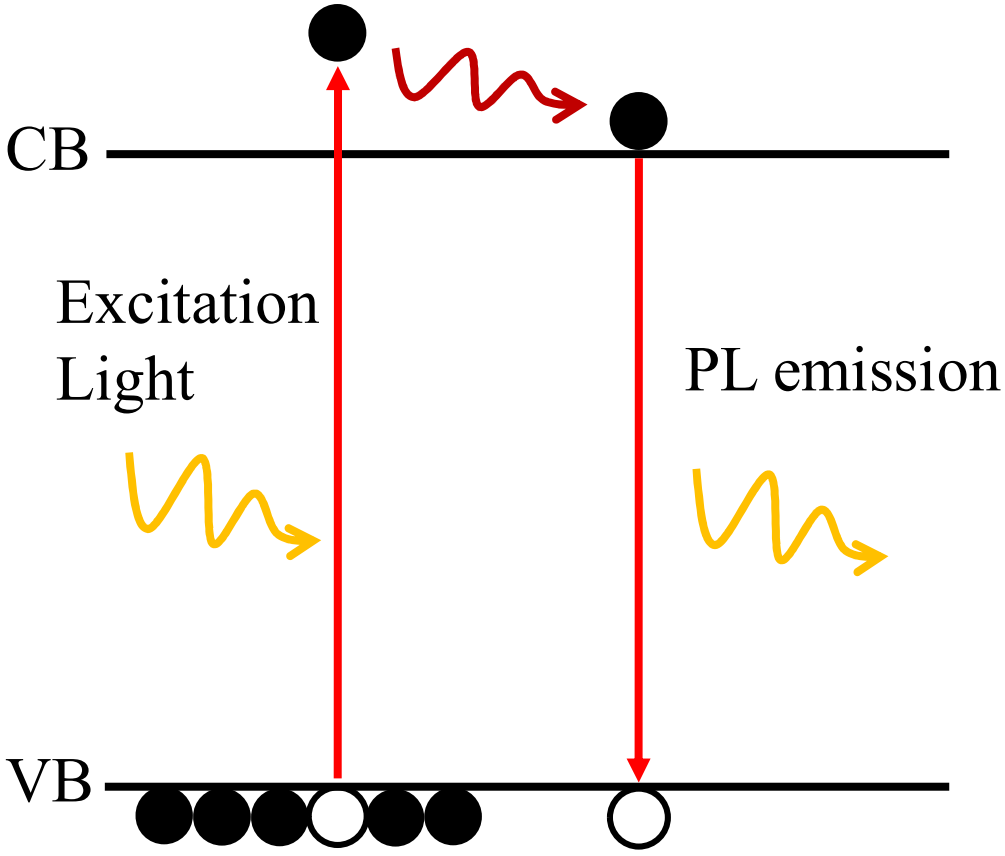

Figure 2-3. PL emission pattern diagram.

2.3 Ultraviolet-visible-near infrared spectroscopy

Ultraviolet-visible-near infrared (UV-Vis-NIR) spectroscopy is employed to record the absorbance or reflectance spectra of a sample. This pertains to the assessment of the internal

electronic structure and the phase composition identification of materials. Generally speaking, measurements for light absorption adhere to the Beer-Lambert law [1]:

$$A = -log_{10}\frac{I_t}{I_0} = log_{10}\frac{1}{T} = K \cdot l \cdot c \qquad (2-2)$$

where A represents absorbance, I_t is the intensity of the transmitted light, and I_0 is the intensity of the incident light, T means the transmittance ratio ($T = I_t/I_0$), K is the absorption coefficient, l is the thickness of the sample, c is the concentration of the sample. As the above formula indicates, when a beam of light passes through an absorbing medium, a portion of the energy is absorbed by the medium, hence the energy of the transmitted light is reduced. On the other hand, the absorption band edge is closely related to the bandgap, therefore, by fitting the band edge, the bandgap width of the material can be determined [2]. In our experiments, due to the thickness (>1mm) of the crystals, the aforementioned transmission method was not able to yield the desired results effectively. Consequently, we utilized an integrating sphere setup with spectrophotometer V760 manufactured by Japan Spectroscopic (JASCO) for the absorption measurement. As shown in Fig.2-2, since the entire interior of the sphere is coated with a highly diffusive layer, when light enters the integrating sphere, apart from the portion absorbed by the crystal, the rest of the light is reflected and received by the detector located at the bottom of the sphere. The absorption spectrum in Work 2 was measured using this method.

2.4 Photoluminescence spectroscopy

Photoluminescence (PL) spectroscopy is a method employed to measure the emission from a semiconductor when it has been excited by a light source whose energy is larger than the bandgap of the semiconductor and subsequently emits PL at a longer wavelength. As shown in Fig.2-3, when the electron at the top of the valence band (VB) is excited by excitation light, depending on the energy of the excitation light, the electron reaches inside the conduction band.

Since this excited state is unstable, the electron will fall back to the bottom of the conduction band (CB) through thermalization, and finally recombine with the hole at the top of the VB, emitting PL. In this thesis, the PL and TRPL data were characterized by a NIR PL lifetime spectrometer (C12132, Hamamatsu Photonics, Hamamatsu, Japan). A 473nm laser is used as the light source, and we regulate the initial carrier density by varying the excitation intensity in order to observe the carrier dynamics in the crystal.

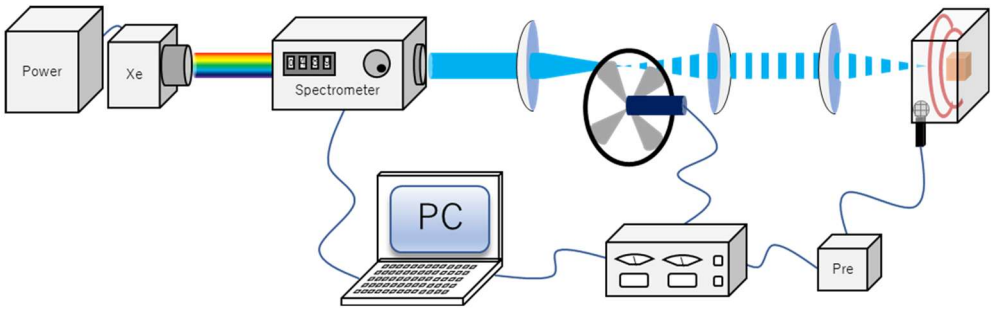

Figure 2-4. Experiment setup for PA measurement.

2.5 Photoacoustic spectroscopy

Photoacoustic spectroscopy (PAS) is a measurement technology based on photothermal conversion. Fig.2-4 showed the experiment setup of photoacoustic spectroscopy measurement. In PA measurement, we used a 300W xenon lamp as a light source. The monochromatic light was obtained by Nikon G250 Monochromator. A chopper connected with Model SR540 Chopper Controller is used to control the frequency of light. The PA signal was detected by a microphone embedded in the PA cell and amplified by a pre-amplifier and NF electronic instruments 5610B two-phase lock-in amplifier. PA cell was produced by processing two pieces of aluminium plates. The plates were hollowed to form a cylinder space where a rubber ring was set to prevent air leakage.

The specific measurement process is as follows. The Xenon light source generates white light that is subsequently monochromated. After being treated by the spectrometer,

monochromatic light will be cut by chopped as pulse light and then irradiated the sample which is placed in a sealed cell. When pulse light irradiates the sample, the photothermal conversion phenomenon will happen in the surface layer of the sample. The thermal energy produced on the sample's surface causes the gas within the photoacoustic (PA) cell to oscillate at a constant frequency, creating a photoacoustic effect. This effect is detected by a microphone installed within the PA cell and relayed to a pre-amplifier. A lock-in amplifier, synchronized with a reference signal from the chopper, filters out noise. Subsequently, the purified signal is recorded as PA data in the computer.

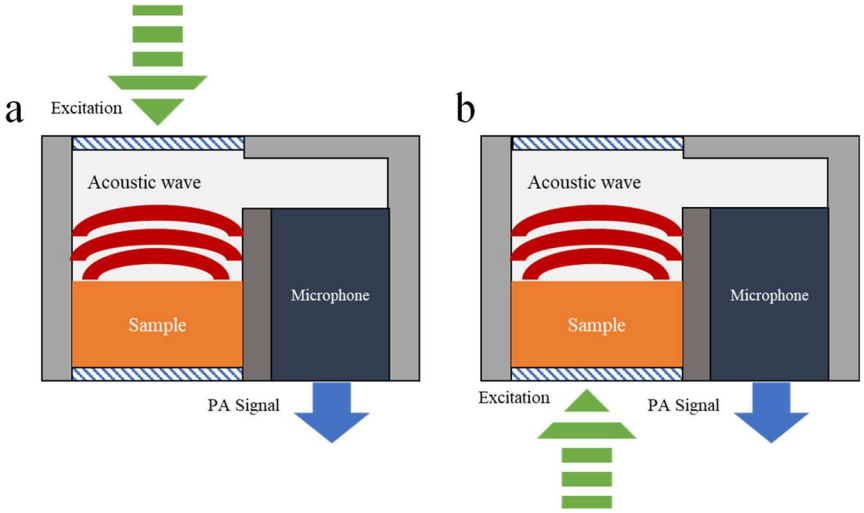

Figure 2-5. Experimental arrangement for PA detection in the (a) reflection detection configuration (RDC) and (b) transmission detection configuration (TDC).

Additionally, PA testing is divided into reflection detection configuration (RDC) and transmission detection configuration (TDC), depending on the placement of the sample. Fig.2-5 displays the cross-section diagrams for the two modes. In RDC mode (Fig.2-5a), incident light beams onto the front surface of the sample. The rear face of the sample makes contacted with glass holder. In this scenario, the intensity of pressure change on the surface of the sample is proportional to the production of thermal energy in one thermal diffusion length μ_s from the front surface in a period of excitation light [3]. The μ_s is calculated by modulation frequency with the

formula: $\mu_s=(2a/f)^{1/2}$, ($a=k/\rho C$), where k is thermal conductivity, ρ is the density of the sample, C is the heat capacity. With fixed frequency, the absorption at the specific depth in the sample can be probed. In TDC mode (Fig.2-5b), excitation light irradiates the rear surface of the sample. The front face is in contact with the gas in the cell. Different from RDC mode, the PA signal collected in TDC mode can be attributed to the mixing process of thermal and electrical diffusion. On the one hand, photo-generated carries around the rear face of the sample will diffuse to the front face according to their initial distribution. On the other hand, thermal energy produced by carrier relaxation processes will also diffuse across the sample by phonon that contributes to the PA signal. Up to these two diffusion processes, surface recombination velocity and transport properties of the sample can be evaluated.

2.6 Space charge limited current

Space charge limited current (SCLC) technique is a commonly-used method to estimate the trap state density and carrier mobility in single-carrier device. We will introduce the principles behind the SCLC measurement as follows. Ideally, in the case of insulator, the trap states and intrinsic carrier concentration can be overlooked. We can divide the current in the device into three parts, drift current, diffusion current and displacement current, as shown in the equation below:

$$J = ne\mu E - eD\frac{dn}{dx} + \varepsilon_0\varepsilon_r\frac{dE}{dt} \qquad (2-3)$$

where J is the current density, n is the electron concentration, e is the electric charge, μ is the mobility of electron, E is the applied electric field, D is the electron diffusion coefficient, ε_0 is the vacuum dielectric constant, ε_r is the relative dielectric constant. If the steady state is considered, Eq.2-3 can be simplified as:

$$J = ne\mu E - eD\frac{dn}{dx} \qquad (2-4)$$

According to the poisson equation, that dE/dx=ne/$\varepsilon_0\varepsilon_r$, the Eq.2-4 can be further rewrite into:

$$J = \varepsilon_0\varepsilon_r\mu E\frac{dE}{dx} - \varepsilon_0\varepsilon_r D\frac{d^2E}{dx^2} \quad (2-5)$$

It can be considered that the diffusion current is more obvious at the interface between the electrode and the material, which can be ignored here.

$$J \approx \varepsilon_0\varepsilon_r\mu E\frac{dE}{dx} \quad (2-6)$$

After rearrangement,

$$E = \left(\frac{2J}{\varepsilon_0\varepsilon_r\mu}(x+x_0)\right)^{\frac{1}{2}} \quad (2-7)$$

The J-V relation can be obtained by integrating the electric field after adding the boundary conditions,

$$J = \frac{9\varepsilon_0\varepsilon_r\mu V^2}{8s^2} \quad (2-8)$$

where s is the thickness of the sample. The Eq.2-8 is called as Mott-Gurney law. In general, the carriers in the medium can be divided into two types, one is the intrinsic carrier (n_0), which is determined by the temperature and the material itself, and the other is the electrically injected carrier (n_1). Thus, the current density can also be divided into two parts:

$$J = n_0 e\mu\frac{V}{s} + \frac{9\varepsilon_0\varepsilon_r\mu V^2}{8s^2} \quad (2-9)$$

The first part of the formula is the ohmic region, and the second part is the space charge limited region. If the applied voltage is small, the ohmic part dominates, so the slope of the J-V curve is 1 after taking the log. With the gradual increase of voltage, the influence of space charge limited current gradually increases, when the two are equal, the experimental curve will have a mutational site from slope 1 to slope 2, this voltage is called V_{trans}, and then the space charge limited current dominates. The reference diagram for the SCLC test results is shown in Fig.2-6.

Therefore, by fitting the space charge current region, we can get the mobility of the material, and then according to Einstein's equation, we can give the corresponding diffusion coefficient. In our experiment, the SCLC measurement was performed with a Keithley 2460 source in an ambient atmosphere for a dark J-V curve.

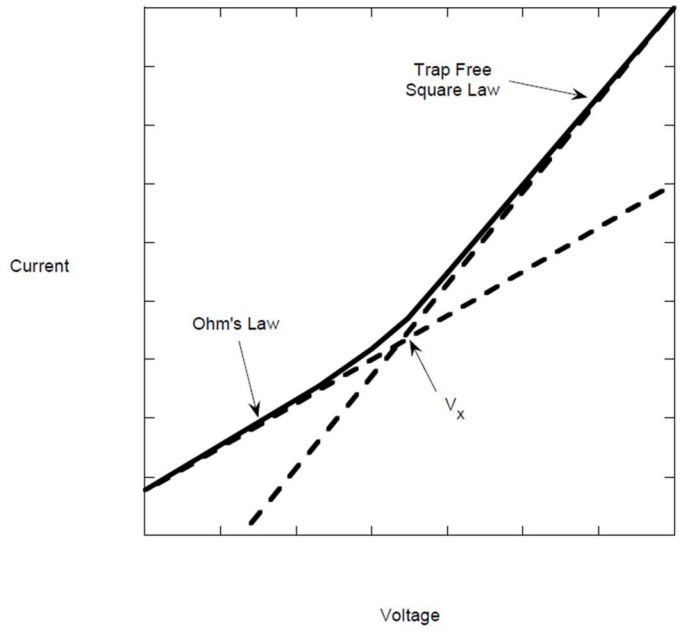

Figure 2-6. Space charge–limited current behavior with only ohmic and trap-free space charge–limited current regions.

2.7 Profilometer

DektakXT stylus profilometer was used to measure the thickness of samples. The crystal thickness is obtained by scanning the edges of the crystal with a probe, and within a range of about 1mm, the difference in height between the crystal and the glass substrate is measured. This method is used to calibrate the thickness parameter in the TDC mode in PA measurement by obtaining the thickness.

2.8 Impedance spectroscopy

An impedance spectroscopy (IS) measurement, similar to a resistance measurement, involves applying voltage to both sides of a cell device and observing the changes in current to determine the impedance spectrum. However, unlike ideal circuits with a single resistance element, real-world circuits are more complex. Therefore, the impedance method uses alternating current (AC) voltage. Assuming the voltage can be expressed as a sinusoidal function, the resulting current can also be analyzed using a sinusoidal function. By dividing the two, the impedance spectrum can be obtained. According to the transformation of Euler's formula, we can express the impedance in complex function.

$$Z(\omega) = \frac{E}{I} = Z_0 \exp(j\phi) = Z_0(cos\phi + jsin\phi) \qquad (2-10)$$

where ω is the angular frequency and ϕ is the phase angle. $Z(\omega)$, the impedance as a function of angular frequency, can be written as an expression with real and imaginary parts. If the real part is plotted on the x-axis and the imaginary part on the y-axis, an impedance spectrum at a fixed frequency can be plotted. In our experiment, the IS measurements were performed under dark air using an impedance analyzer (BioLogic, SP-300) by applying 10 mV rms perturbation at frequencies from 1 MHz to 1 Hz for different forward bias voltages.

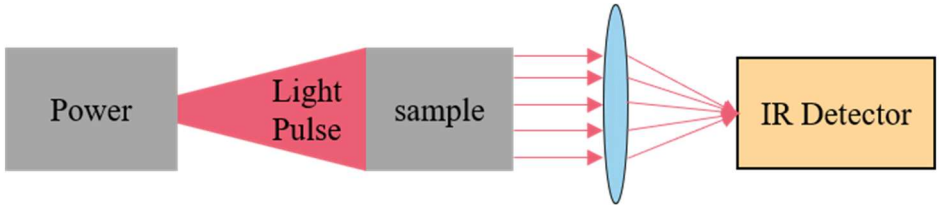

Figure 2-7. The Flash method scheme.

2.9 The Flash method

The Flash method is used to determine the thermal diffusivity of the material. The schematic setup of measurement is shown in Fig.2-7. The sample is subjected to a high-intensity short duration radiant energy pulse, and the energy will then be absorbed by the sample and emitted

again on the top face. This radiation results in a temperature rise on the surface of the sample which is recorded by an infrared (IR) detector.

Suppose that initial temperature distribution for a uniform thermally insulate sample with thickness L at time t can be expressed as

$$T(x,t) = \frac{1}{l}\int_0^l T(x,0)dx + \frac{2}{l}\sum_{n=1}^{\infty} \exp\left(\frac{-n^2\pi^2\alpha t}{l^2}\right) \times cos\frac{n\pi x}{l}\int_0^l T(x,0)cos\frac{n\pi x}{l}dx \quad (2-11)$$

where α is thermal diffusivity. In the case that sample is illuminated by pulse light with radiant energy Q, the equation at x=l can be simplified using initial condition to be:

$$T(l,t) = \frac{Q}{\rho C l}\left[1 + 2\sum_{n=1}^{\infty}(-1)^n \exp\left(\frac{-n^2\pi^2}{l^2}\right)\alpha t\right] \quad (2-12)$$

where ρ is density of sample and C is the heat capacity of sample. Here, two dimensionless parameters should be defined:

$$V(l,t) = \frac{T(l,t)}{\Delta T_{max}} \quad (2-13)$$

$$\omega = \frac{\pi^2}{l^2}\alpha t \quad (2-14)$$

where ΔT_{max} is the maximum temperature rise, combined with above equations, V (l, t) can be represented as:

$$V(l,t) = 1 + 2\sum_{n=1}^{\infty}(-1)^n \exp(-n^2\omega) \quad (2-15)$$

Thermal diffusivity α is deduced from that, when V=0.5, ω is equals to 1.388.

$$\alpha \approx \frac{1.388l^2}{\pi^2 t_{\frac{1}{2}}} \quad (2-16)$$

where $t_{1/2}$ is attributed to time when temperature rises to half of ΔT_{max}.

2.10 Bibliography

1. Swinehart, D. F., The Beer-Lambert Law. *J. Chem. Educ.* **1962,** *39* (7).

2. Tang, Z.; Bessho, T.; Awai, F.; Kinoshita, T.; Maitani, M. M.; Jono, R.; Murakami, T. N.; Wang, H.; Kubo, T.; Uchida, S.; Segawa, H., Hysteresis-free perovskite solar cells made of potassium-doped organometal halide perovskite. *Sci Rep* **2017,** *7* (1), 12183.

3. Dramicanin, M. D.; Nikolic, P. M.; Ristovski, Z. D.; Vasiljevic, D. G.; Todorovic, D. M., Photoacoustic investigation of transport in semiconductors: Theoretical and experimental study of a Ge single crystal. *Phys. Rev., B Condens. Matter* **1995,** *51* (20), 14226-14232.

4. Parker, W. J.; Jenkins, R. J.; Butler, C. P.; Abbott, G. L., Flash Method of Determining Thermal Diffusivity, Heat Capacity, and Thermal Conductivity. *J. Appl. Phys.* **1961,** *32* (9), 1679-1684.

Chapter 3. Simultaneous Characterization of Optical, Electronic, and Thermal Properties of Perovskite Single Crystals Using Photoacoustic Technique

3.1 Introduction

Recently, metal halide perovskite (MHP) has emerged as an attractive material for photovoltaic and thermoelectric applications, [1-4] typically showing a strong optical absorption, long carrier diffusion lengths, low trap densities, and low thermal conductivity.[5] Regarding optoelectronic devices based on MHPs, the key factors that determine the device performance include the carrier diffusion length and recombination rate in both the surface and the bulk of the material. To effectively improve the device performance, the characterization of these fundamental properties with accuracy and validity is essential. To date, many techniques have been utilized to acquire the values of these intrinsic physical properties, classified mainly as optical and electrical measurements. However, due to some inherent flaws of the techniques, it is still difficult to effectually gain the veritable properties of MHP materials.

To differentiate the carrier recombination mechanisms between the bulk and surface, the one/two-photon excitation technique has been used in most reports. [6, 7] However, high-energy beam irradiation in the local area of the sample may lead to photoinduced degradation or destruction of the material, giving rise to a misestimation of the experimental results. In the estimation of surface recombination, transient reflection spectroscopy (TRS) has been proven to be a powerful tool, but its instrumentation, sample requirements, and data interpretation can be daunting. [8-10]

The carrier diffusivity and photoexcited carrier lifetime are critical physical parameters needed to specifically determine the carrier diffusion length ($L = (D \times \tau)^{1/2}$, L: diffusion length; D: diffusivity; τ: lifetime), which offers a criterion for optimizing device thickness and morphology. [11] To date, the carrier diffusivity has been determined from spectroscopic techniques such as transient absorption (TA) decay dynamics and photoluminescence (PL) quenching techniques based on the diffusion model leading to an ambipolar diffusion coefficient. [12-14] Additionally, the carrier diffusivity can be speculated indirectly from mobility, which is primarily estimated by a transient terahertz conductivity measurement, space charge limited current, Hall effect, and time-of-flight methods. [5, 14-17] Concerning the photoexcited carrier lifetime, it is reported that a commonly used PL lifetime measurement may severely underrate the intrinsic lifetime in halide perovskite due to grievous surface recombination. [18] In addition, several device-based electronic measurements, for example, transient photovoltaic and impedance spectroscopy, have also been used to investigate the carrier lifetime. [17, 19, 20] However, the fabrication of the device and work conditions have an essential impact on the results of these measurements.

Compared with these electronic features, which are brought into focus, the thermal transport properties of MHPs have been little studied, despite being very important for feasible applications such as thermoelectric devices. [21] An ultralow thermal conductivity has been reported for many perovskite materials, such as $MAPbI_3$ and $CsPbBr_3$, [22, 23] suggesting practicability in thermoelectric materials. [24] To date, many techniques, for example, scanning near-field thermal microscopy (SThM) based on the 3ω-technique, frequency domain thermoreflectance (FDTR), and the laser flash technique (LFA), have been utilized to study thermal transport properties. [21, 25-27] Nevertheless, for air/moisture-sensitive materials such as MHP, degradation may affect the measurement even after a short time of exposure to air during sample preparation. Furthermore, some measurements based on high-energy beam irradiation may accelerate the degradation of

halide perovskite influencing the experimental result. [28] In this regard, a nondestructive route in an inert gas atmosphere is required for studying the thermal transport properties for MHPs.

The photoacoustic (PA) technique is a photothermal detection measurement, that has been proven to be a powerful tool used to study the optical, electronic, and thermal properties of semiconductor materials by probing the nonradiative recombination process after optical absorption. [29] The advantages of the PA technique include the following: (1) it is a nondestructive and noncontact method; (2) this technique can be applied to most semiconductors regardless of their shape or state; (3) the PA cell (sample holder) with a good airtight seal can prevent the degradation of the sample from air or moisture and can be measured in an inert gas atmosphere; and (4) optical absorption, surface recombination velocity, carrier diffusivity, photoexcited carrier lifetime, and thermal diffusivity can be obtained simultaneously. These advantages render the PA technique a vigoroso measurement for environment-sensitive MHP material. To date, the PA technique has been applied to many semiconductor materials such as polycrystal CdTe and single crystal Ge. [30, 31] However, as a common measurement, the PA technique was excluded in the field of MHP materials.

The MHP single crystals have a reduced defect state and are free of grain boundaries compared with their corresponding polycrystalline films, show better performance for device fabrication and offer a potential platform for studying the fundamental properties of MHP materials. [17, 32] Therefore, in this work, the PA technique was introduced to study the optical, electronic, and thermal properties of typical perovskite single crystals $CH_3NH_3PbBr_3$ ($MAPbBr_3$) and $CH_3NH_3PbI_3$ ($MAPbI_3$). In our experiment, the optical absorption of single crystals was measured under a reflection detection configuration (RDC) and the electronic and thermal transport parameters were acquired simultaneously under a transmission detection configuration (TDC). [31] Note that, the MHP single crystals were used in TDC mode because it is easier to adjust

in a large thickness range. By comparing the results with previous literature and other characterizations, we confirmed the feasibility of the PA technique in characterization of the optical, electronic and thermal properties of the perovskite single crystals.

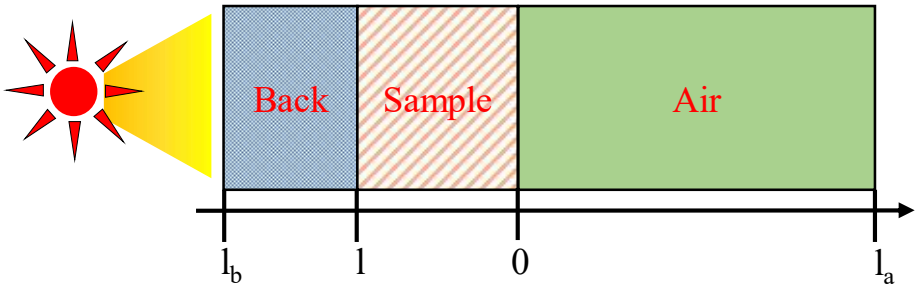

Figure 3-1. Geometry of PA cell: Backing/Single crystal/Air.

3.2 Theoretical analyses under TDC

In 1976, A. Rosencwaig and A. Gersho firstly put forward the theory of the PA effect with solids [33]. Dramicanin and coworkers applied the theory to semiconductor material and developed a model to analyze PA signals [31]. We used the theory to theoretically analyze the Glass/perovskite single crystal/air (Fig.3-1) system under TDC. A one-dimension model is exhibited here which can be divided into three parts: backing (glass), sample (perovskite single crystal), and gas (air). Under TDC mode, a beam of monochromatic light with angular frequency ω, penetration depth x, is used as excitation light. The flux of modified light is given by

$$I = \frac{I_0}{2} e^{-\alpha x} Re\left[1 + e^{j\omega t}\right] \qquad (3-1)$$

where I_0 is the intensity of incident light, and α is the optical absorption coefficient at the fixed excitation wavelength.

To evaluate the photoinduced excess carrier distribution, some assumptions should be made. The density of photoinduced excess electron is equal to that of the excess hole. And in this case, auger recombination could be neglected either [29, 31]. Additionally, in this work, the excitation energy is always greater than the bandgap of our samples. According to the hypnosis, the carrier

diffusion equation is linear in excess electron density n or excess hole density p. Therefore, carrier diffusion at an angular frequency ω could be expressed as

$$\frac{\partial^2 n(x)}{\partial x^2} - \frac{1}{L_D^2} n(x) = -\frac{\alpha I_0}{2ED} e^{-\alpha} \tag{3-2}$$

in consideration of surface recombination of front and rear face, the boundary conditions could be written as

$$\begin{aligned} D\frac{dn(x)}{dx}|x = 0 = s_g n(0) \\ D\frac{dn(x)}{dx}|x = l = s_b n(l) \end{aligned} \tag{3-3}$$

where $L_D = \sqrt{\frac{D\tau}{j\omega t+1}}$ denotes the diffusion length of a complex expression, τ is excess carrier lifetime in bulk, D is diffusion coefficient and E is excitation energy. s_g and s_b mean surface recombination velocity of front and rear face. Here, we assumed that the front and rear faces of perovskite single crystal are in the same state in our experiment, s_g=s_b=s. Then, periodic temperature variation could be estimated by the thermal diffusion equation which is given as follows

$$\frac{\partial^2 T_i(x,t)}{\partial x^2} - \frac{1}{D_{thi}} \frac{\partial T_i(x,t)}{\partial t} = \begin{cases} -\frac{Q(x,t)}{k_i}, & i = s \\ 0, & i = g, b \end{cases} \tag{3-4}$$

where D_{thi} and k_i are thermal diffusivity, and thermal conductivity respectively. Q (x, t) is supposed to thermal source in the sample which is generated by main three processes. The first one is intraband thermalization of photocarriers to bandgap within the conductive band. And the second and third one refers to nonradiative recombination of carriers produced in bulk or surface. The three sources could be calculated as follows

$$Q_1 = \frac{\alpha I_0}{2} \frac{E - E_g}{E} e^{-\alpha} \tag{3-5}$$

$$Q_2 = \frac{E_g}{\tau} n(x,t) \tag{3-6}$$

In the case of the thermal source of nonradiative surface recombination,

for rear face (x=0):

$$Q_3 = E_g n(0) s_b \tag{3-7}$$

for front face (x=l):

$$Q_3 = E_g n(l) s_g \tag{3-8}$$

where E_g is the bandgap of our sample. Q_1 and Q_2 are applied into thermal diffusion equations and Q_3 is used as boundary conditions. Thus, the thermal diffusion could be adapted as following

$$\frac{\partial^2 T_i(x)}{\partial x^2} - \sigma_i^2 T_i(x) = \begin{cases} -\frac{\alpha I_0}{2k_s}\frac{E - E_g}{E} e^{-\alpha x} - \frac{E_g}{k_s \tau} n(x), & i = s \\ 0, & i = g, b \end{cases} \tag{3-9}$$

with the boundary conditions

$$T_b(0) = T_s(0) \tag{3-10}$$

$$T_s(l) = T_g(l) \tag{3-11}$$

$$-k_b \frac{dT_g(x)}{dx}\bigg| x = 0 = -k_s \frac{dT_s(x)}{dx}\bigg| x = 0 + s_b n(0) E_g \tag{3-12}$$

$$-k_s \frac{dT_s(x)}{dx}\bigg| x = l = -k_g \frac{dT_g(x)}{dx}\bigg| x = l + s_g n(l) E_g \tag{3-13}$$

where $\sigma_i^2 = j\omega / D_{thi}$. Owing to short-wavelength excitation we used, it is assumed that $e^{-\alpha l} \approx 0$. In addition, heat is flowed only in the sample and does not affect the glass layer and air layer. Subsequently, thermal diffusion equation can be solved via dividing it into three parts. Thus, T(l) is formed as

$$T(l) = T_1(l) + T_2(l) + T_3(l) \tag{3-14}$$

$$T_1(l) = A \frac{E - E_g}{2D_{ths}} \frac{1}{\sin(\sigma_s l)} \tag{3-15}$$

$$T_2(l) = A \frac{E_g F}{\tau \sigma_s^2} \frac{1}{m^2 - 1} \left[\frac{m \frac{D}{L_D} \sin\frac{l}{L_D} - m s \cosh\frac{l}{L_D}}{\sinh(\sigma_s l)} + m s \coth(\sigma_s l) - \frac{D}{L_D} \right] \tag{3-16}$$

$$T_3(L) = A \frac{E_g F}{\sigma_s} \left[\frac{s}{sin(\sigma_s l)} \left(\frac{D}{L_D} \cosh\frac{l}{L_D} + s sinh\frac{l}{L_D} \right) + \frac{sD}{L_D} \coth(\sigma_s l) \right] \tag{3-17}$$

where $A = \frac{I_0}{k_s E}$, $F = \frac{1}{(\frac{D}{L_D}+s)^2 e^{\frac{l}{L_D}} - (\frac{D}{L_D}-s)^2 e^{-\frac{l}{L_D}}}$, $m = \frac{1}{L_D \sigma_s}$. Note that $T_1(l)$, $T_2(l)$, $T_3(l)$ is generated from Q_1, Q_2 and Q_3 respectively. In terms of thermal-piston model, the pressure fluctuation ΔP in PA cell can be given

$$\Delta P = \frac{BT(L)}{\sqrt{f} e^{j\omega t}} \qquad (3-18)$$

where B is a constant relating to ambient pressure, temperature, the length of gas volume and thermal diffusivity of gas in PA cell.

3.3 Experimental Section

3.3.1 Chemicals and reagents.

Lead bromide (≥98%), N, N-Dimethylformamide (anhydrous, 99.8%), γ-Butyrolactone (ReagentPlus®, ≥99%), hydrobromic acid (48wt.% in H_2O) and methylamine (40% solution in water) were purchased from Sigma Aldrich. 50% Phosphinic Acid and Methylammonium Iodide were purchased from Fujifilm Wako Pure Chemical Corporation. Lead iodide (99.99%) was purchased from High Purity Chemicals. All salts and solvents were used as received without any further purification.

3.3.2 Synthesis of MABr

Methylammonium bromide (MABr) was synthesized following a literature procedure. [34] First, a concentrated aqueous solution of hydrobromic acid (HBr) reacted with methylamine (CH_3NH_2) in an ice bath for 2 hours with constant stirring. The precipitate was yielded by evaporation at 70 °C. MABr was then dissolved in ethanol at 80 °C, recrystallized from the supersaturated solution in the refrigerator, and dried at 60 °C in a vacuum oven overnight.

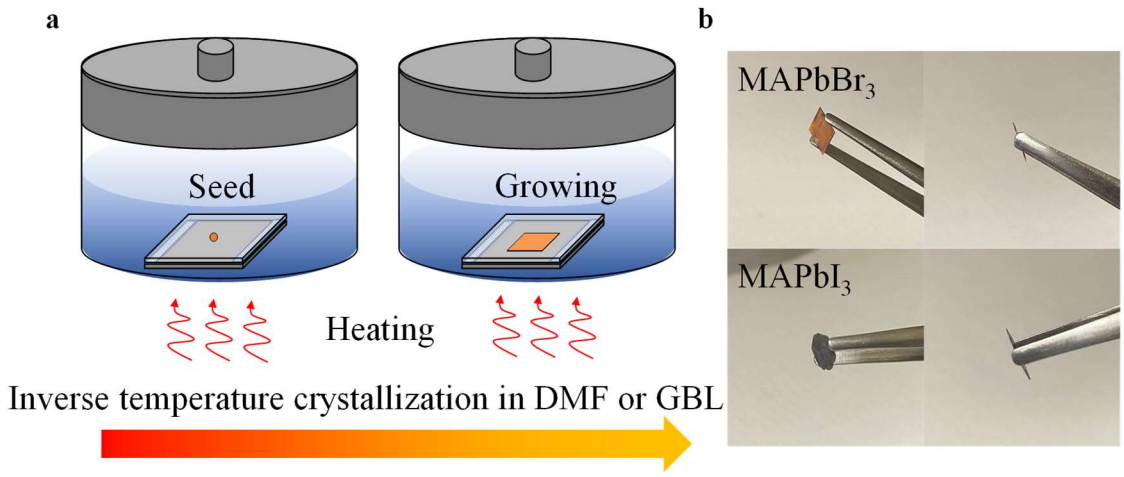

Figure 3-2. (a) Schematic representation of growth process of single crystal. (b) Pictures of single crystals of $MAPbBr_3$ and $MAPbI_3$.

3.3.3 Synthesis of $MAPbX_3$ (X=Br, I) single crystal

The diagram of synthesis of $MAPbX_3$ single crystals were shown in Fig.3-2a. The surface treatment was used for a pair of glasses. [35] The hydrophobic glasses were separated with two micro cover glasses to be placed in a container. 1.2M solution containing MABr and $PbBr_2$ was prepared in DMF for growing $MAPbBr_3$ single crystal. 1 M solution containing MAI and PbI_2 was prepared in GBL for growing $MAPbI_3$ single crystal. The bromide solution was prepared at room temperature, while the iodide solution was prepared at 65℃. After overnight stirring, the solutions were filtered using a 1.0 μm pore size PTFE filter. 10 ml filtrate was transferred into pre-prepared containers and the container was kept at 85 and 120℃ for growing Br- and I-based perovskite single crystals. The pictures of $MAPbX_3$ single crystals have been shown in Fig.3-2b.

3.3.4 Measurement and characterization

The XRD patterns were gained by the Rigaku Ultima III X-ray diffractometer with monochromatic Cu-Kα irradiation. DektakXT stylus profilometer was used to measure the thickness of samples. The thermal diffusion was characterized by NETZSCH LFA 447 nano flash with the LFA-reference sample Pyrex×7740. The space charge limited current (SCLC)

measurement was performed with a Keithley 2460 source in an ambient atmosphere for a dark J-V curve. The impedance spectroscopy (IS) measurements were performed under dark air using an impedance analyzer (BioLogic, SP-300) by applying 10 mV rms perturbation at frequencies from 1 MHz to 1 Hz for different forward bias voltages. In PA measurement, a 300W xenon lamp was used as a light source. A beam of monochromatic light was got by Nikon G250 Monochromator. A chopper connected with Model SR540 Chopper Controller is used to modify the frequency of light. The PA signal was detected by a microphone embedded in the PA cell and amplified by a pre-amplifier and NF electronic instruments 5610B two-phase lock-in amplifier. PA cell was produced by processing two pieces of aluminium plates. The plates were hollowed to form a cylinder space where a rubber ring was set to prevent air leakage.

3.4 Results and discussion

It has been reported that the thickness of specimen (l) has a significant impact on PA measurement under the TDC mode. [33] As the effective thermal diffusion length in the sample (μ_s) defined in PA theory is dependent on the modulation frequency, the value relationship between l and μ_s is an important contributory factor to the PA signal. To completely evaluate the thermal and electronic properties, it has been verified that the appropriate thickness of the MHP is hundreds of micrometers in this study. Thus, $MAPbBr_3$ and $MAPbI_3$ single crystals were synthesized using the space-confined inverse temperature crystallization method to obtain the thickness. [36] Two pieces of glass were treated as hydrophobic and separated face-to-face by two glass spacers with a designed distance to confine the crystal growth within the gap in a flat container. Based on the inverse temperature crystallization [16], 85 ℃ and 120 ℃ were employed for growing the $MAPbBr_3$ and $MAPbI_3$ thin single crystals respectively. Powder X-ray diffraction (XRD) patterns of the MHP crystals are shown in Fig. 3-3b, which illustrate the pure perovskite phase for the $MAPbBr_3$ and $MAPbI_3$ single crystals. Cubic and tetragonal structures have been

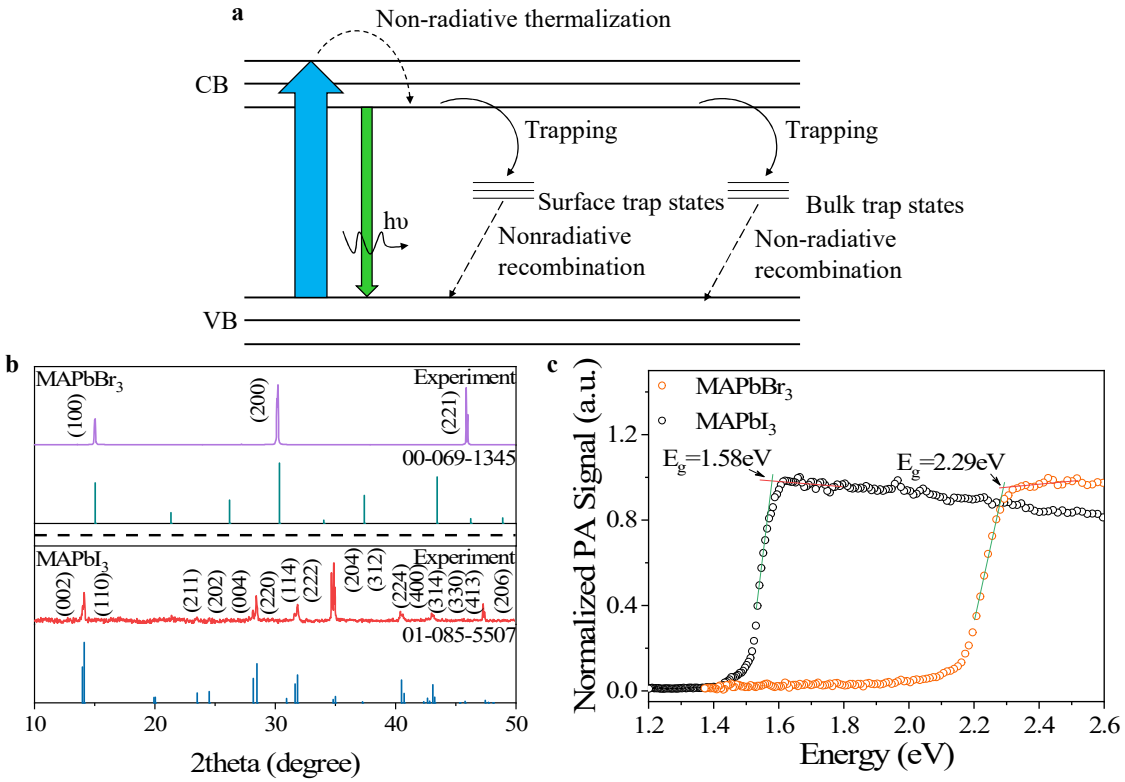

Figure 3-3. (a) Possible thermal sources contributing to the PA signal after optical absorption. (b) Powder X-ray diffraction of $MAPbBr_3$ and $MAPbI_3$ crystals. (c) PA spectra of $MAPbBr_3$ (orange circle) and $MAPbI_3$ (black circle) single crystal measured under the RDC mode. Insets: pictures of single crystals.

confirmed for $MAPbBr_3$ and $MAPbI_3$ single crystals, respectively. The PA measurements under RDC were carried out from 400 nm to 1200 nm (Fig.3-3c) at a fixed frequency of 33 Hz. A sharp absorption edge was clearly observed for each sample, and the bandgap value extracted from the PA spectrum was 2.29 eV for $MAPbBr_3$ and 1.58 eV for $MAPbI_3$, which is consistent with literature reports. [16, 37]

To obtain the electronic and thermal properties, we measured the PA signal dependence of the modulation frequency *f* in TDC mode under light wavelengths of 450 nm for $MAPbBr_3$ and 775 nm for $MAPbI_3$ single crystals. As shown in Fig.3-4, the PA signal intensity for $MAPbBr_3$

and $MAPbI_3$ single crystals decreased with increasing *f* and dropped to a minimum at a specific

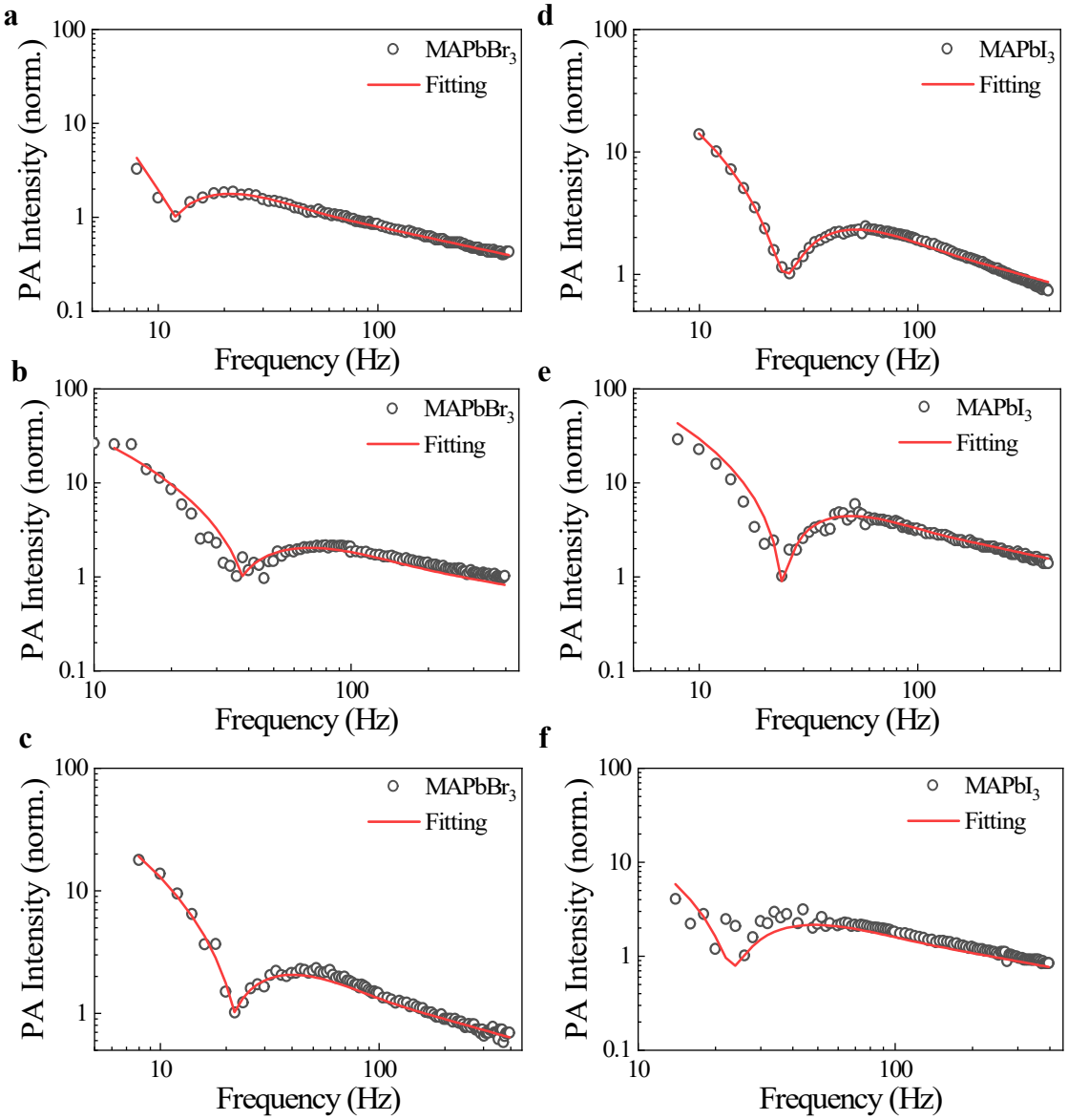

Figure 3-4. Dependence of the PA signal intensity of (a)(b)(c) $MAPbBr_3$ and (d)(e)(f) $MAPbI_3$ single crystal on modulation frequency measured under TDC mode. The wavelength of excitation light is 450 nm for $MAPbBr_3$ and 775 nm for $MAPbI_3$.

frequency (f_{min}), then increased again to an arc shape, and finally decreased with a further increase in the modulation frequency. Here, a program was developed to fit the experimental results of the PA intensity versus *f* with Eq (1). Thickness (l), surface recombination velocity (S), excess carrier lifetime (t), carrier diffusivity (D), and thermal diffusivity (D_{th}) were set as variable

parameters in the fitting process. To achieve an effective fitting, the choice of starting point in the

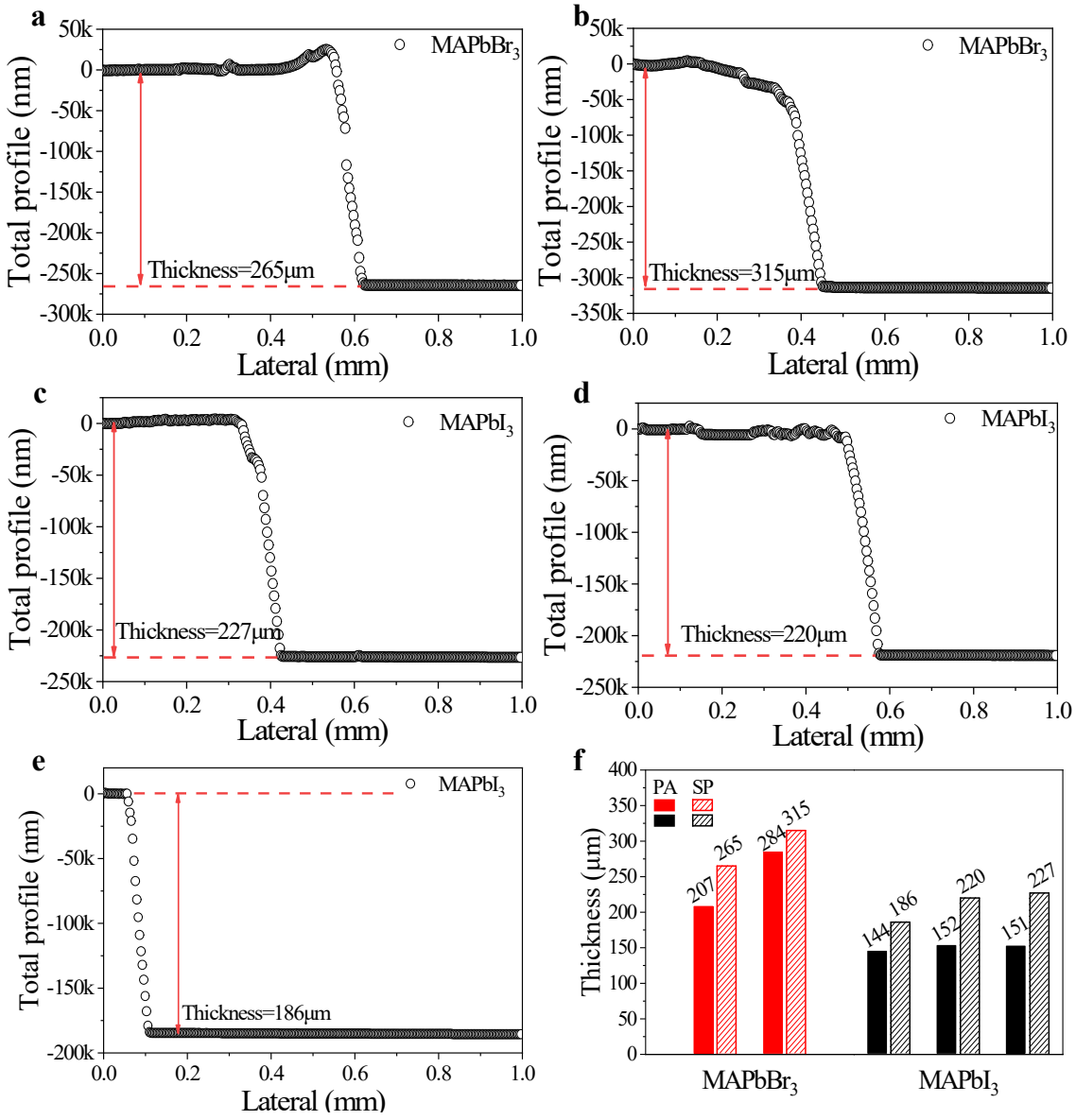

Figure 3-5. (a-e). Step profiler diagram for $MAPbBr_3$ and $MAPbI_3$ single crystal thin films. (f) comparison of thickness deduced from the PA technique with that measured from the step profiler.

fitting process is important. We found that it is better to carry out the fitting program based on the f_{min} point compared with the data starting point or the terminal point because the vicinity of f_{min} is sensitive to all five parameters. According to previous reports, [29, 31] in the lower frequency range compared to f_{min}, the PA signal is governed by thermal behaviors (thermal properties), i.e.,

T_1 and T_3 generated at the irradiated surface since the material is thermally thin in this frequency

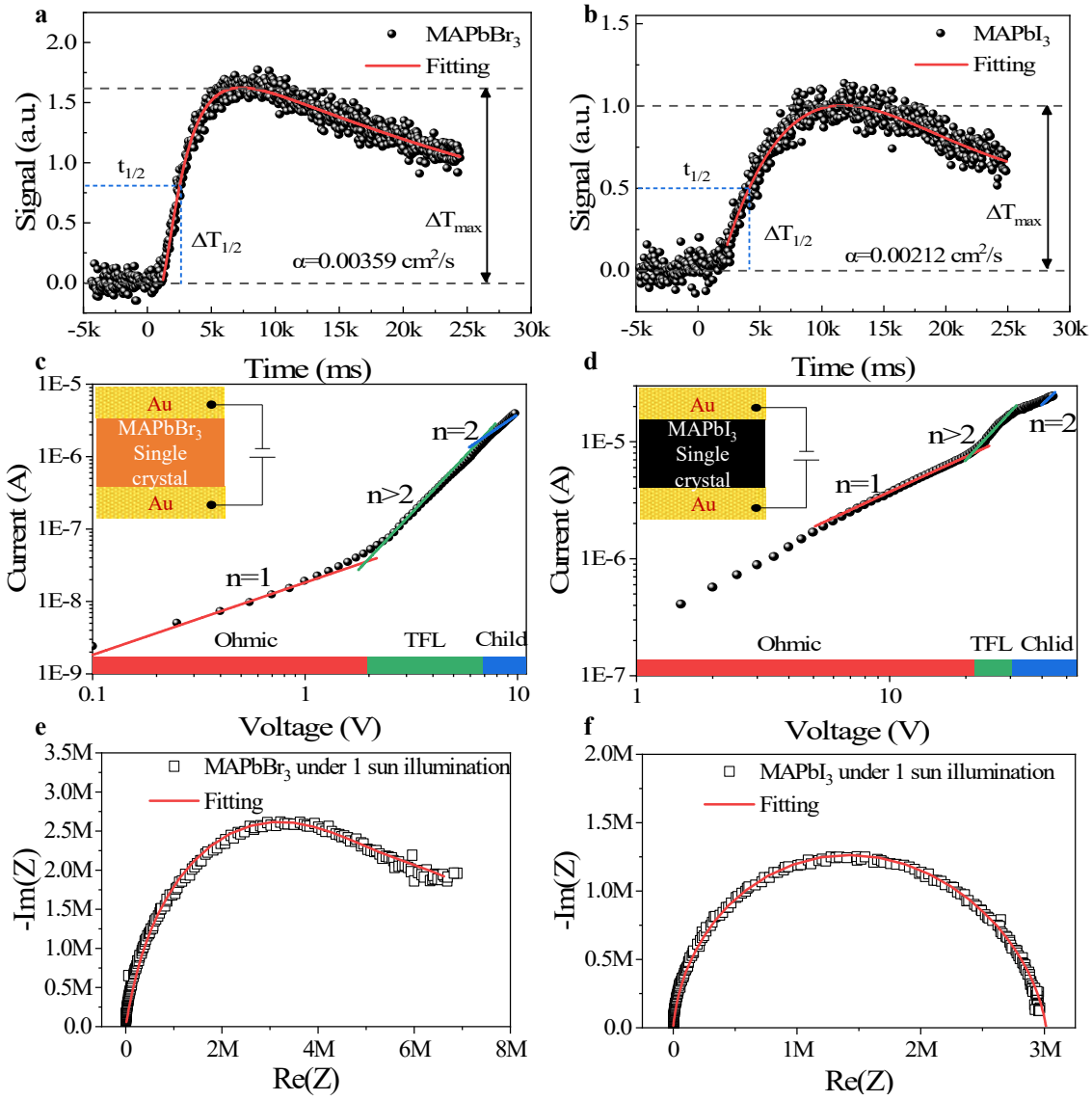

Figure 3-6. (a, b) Thermal diffusivity calculated for (a) $MAPbBr_3$ and (b) $MAPbI_3$ single crystal with Flash method, (c, d) I-V curve of perovskite single crystals exhibiting different regimes got from the l-V curve of perovskite single crystals exhibiting different regimes got from the l-V curve of perovskite single crystals exhibiting different regimes got from the log(V) vs log (I) plots. The regimes divided to three parts: Ohmic(n=1), TFL(n>2) and Child(n=2). (Insets show the device structure of Au/Single crystal/Au), (e, f) IS spectra for $MAPbBr_3$ and $MAPbI_3$ measured under 1 sun illumination fitted with equivalent circuit.

region. In this case, the PA signal can be attributed to the formula $\exp(-l/\mu_s)/f$, ($\mu_s=(\pi f/D_{th})^{1/2}$), where D_{th} is the thermal diffusivity and μ_s is the effective thermal diffusion length for the

corresponding frequency. At f_{min}, $\exp(-l/\mu_s) \approx 0$, where the sample thickness is considered to be approximately five times larger than the thermal diffusion length μ_s. For f larger than f_{min}, the material becomes thermally thick, and the photoexcited carrier diffusion contribution (T_2 resulting from bulk recombination and T_3 resulting from rear face recombination) is dominant. [31] By fitting the whole PA intensity-f curve, L, S, t, D, and D_{th} were determined. To clarify the repeatability of the experiment, we performed PA fitting on three different $MAPbBr_3$ and $MAPbI_3$ single crystals. The thickness of each sample is shown in Fig.3-5, and the other parameters are summarized in Table 1. The optimum values of the fitted parameters were determined when the fitting error was approximately 5% in this study.

Table 1. Electronic and thermal properties of $MAPbBr_3$ and $MAPbI_3$ single crystals (3 samples) derived from the PA technique. (5% error)

Single Crystal	$MAPbBr_3$			$MAPbI_3$		
Surface recombination velocity (cm/s)	2300	1800	2500	3500	4500	3900
Carrier diffusivity (cm^2/s)	6.7	8.0	5.7	7.0	7.0	7.5
Lifetime (μs)	37	50	20	150	100	140
Thermal diffusivity (cm^2/s)	0.0030	0.0030	0.0030	0.0018	0.0018	0.0018

To demonstrate the validity of the results obtained by the PA technique, we used other characterization methods to examine the thickness, and electronic and thermal properties of the same $MAPbBr_3$ and $MAPbI_3$ single crystals. First, the thickness of each sample was investigated by a step profiler, as shown in Fig. S5. We observed a relatively smooth surface of each sample in the stylus scanning process. In comparison to the results obtained from the PA technique, a thicker value was obtained from the step profiler. D_{th} was determined by the flash method (Fig. 3-6 a, b). In this measurement, the sample is subjected to a high-intensity short-duration radiant energy pulse, and the energy is then absorbed by the sample and emitted again on the top face. This

radiation results in a temperature rise on the surface of the sample, which is recorded by an infrared (IR) detector. The thermal diffusivity value is extracted using a half-time method, which is given by Parker et al. as follows [38]:

$$a \approx 1.388 \frac{l^2}{\pi^2 t_{\frac{1}{2}}} \qquad (3-19)$$

where a is the thermal diffusivity, l is the thickness of the sample, and $t_{1/2}$ is attributed to the time point at half of the maximum temperature intensity. Then, the values of thermal diffusivity were determined to be 0.0036 cm^2/s and 0.0021 cm^2/s for $MAPbBr_3$ and $MAPbI_3$ crystals, respectively.

D based on photoluminescence measurement should be an ambipolar diffusion coefficient. [14] We calculated the parameter D via Einstein's relation:

$$D = \frac{\mu k_B T}{q} \qquad (3-20)$$

where μ is the carrier mobility, k_B is Boltzmann's constant, T is the absolute temperature, and q is the electrical charge. To deduce the mobility at room temperature, space charge limited current (SCLC) measurements were performed on $MAPbBr_3$ and $MAPbI_3$ single crystals. As shown in Fig 3-6 c, d, the dependence of SCLC on voltage (i.e., the I-V curve) can be divided into three parts: Ohmic, Trap filled limit (TFL), and Child regimes. In the Ohmic regime, the space charge effect is so weak that the current is linear to the applied voltage. As the voltage increases, a transition from Ohmic to TFL (slope more than 2) is observed where defect traps are being filled. Under high applied voltage, in the trap-free regime, a quadratic dependence I-V relation is shown in the Child regime which follows the Mott-Gurney law [39]:

$$I \propto \frac{9\varepsilon_0 \varepsilon \mu V_b^2}{8d^3} \qquad (3-21)$$

where V_b is the applied voltage, d is the sample thickness, ε_0 is the vacuum permittivity and ε is the relative dielectric constant (25.5 for $MAPbBr_3$ [40] and 32 for $MAPbI_3$ [17]). As a result, the carrier diffusivities were determined to be 7.3 cm^2/s and 8.4 cm^2/s for $MAPbBr_3$ and $MAPbI_3$ single crystals, respectively.

The photoexcited carrier lifetime τ of each sample was determined by impedance spectroscopy (IS) based on the Au/single crystal/PCBM/Ga device. Illumination was set equivalent to that of the one sun to simulate the real working condition of the device. According to Fig. 3-6 e, f, τ was obtained as 70μs and 133μs for $MAPbBr_3$ and $MAPbI_3$ crystals by fitting the IS with the equivalent circuit, as shown in Fig.3-7.

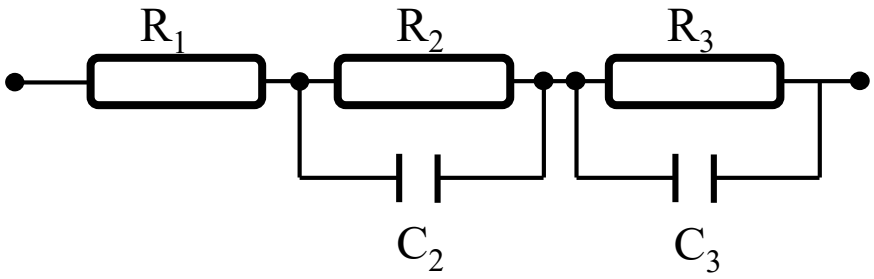

Figure 3-7. Equivalent circuit for IS measurement. R_1 is the series resistance; the high frequency arc is composed of R_2 (recombination resistance) and C_2 (capacitance); the low frequency arc is composed of R_3 (recombination resistance) and C_3 (capacitance).

We summarized the experimental data (SCLC, IS, flash) in Table 2. The determined D, τ, and D_{th} values from the PA technique for $MAPbBr_3$ and $MAPbI_3$ single crystals are greatly consistent with those results measured by the SCLC technique, impedance spectroscopy, and the flash method, which indicates that the PA technique is a feasible and convenient tool that can be used to simultaneously characterize the electronic and thermal properties in perovskite single crystals.

To further affirm the rationality of the results obtained from the PA technique, we compared them with those from previous reports. Fig.3-8 provides the literature values of the electronic and

thermal properties of the MHP single crystals as shown in Table 2. Note that, the purple points were marked as reference experimental data in our work. Most research on D and τ to date is based on the one-photon excitation technique, which, due to the short optical penetration depth,

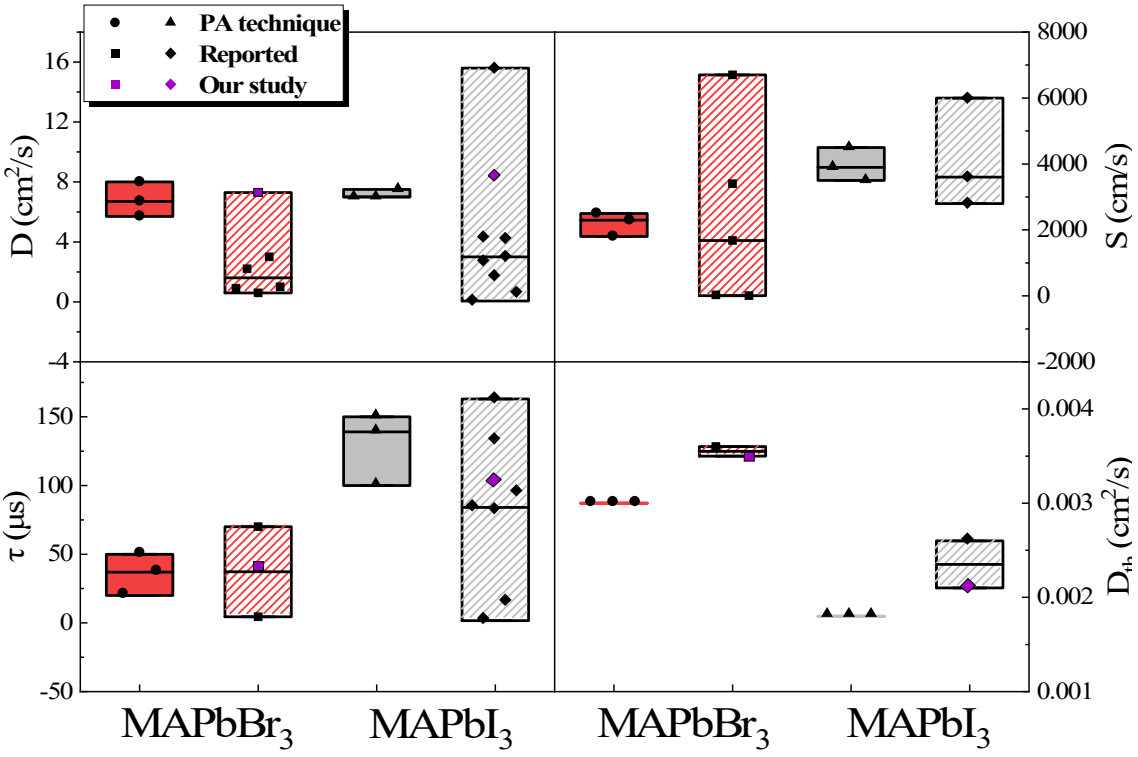

Figure 3-8. Comparison of carrier diffusivity (D), surface recombination velocity (S), carrier lifetime (τ) and thermal diffusivity (D_{th}) of $MAPbBr_3$ and $MAPbI_3$ single crystals obtained from PA technique with the experimental results in our study and literature reports. The red and gray filling parts represent the results obtained from PA technique; and the red and gray slash parts show the reported results from previous literatures. The solid circle and square points signify the data from $MAPbBr_3$; and the solid triangle and rhombus points denote the data from $MAPbI_3$. The purple points mark experimental results (SCLC, IS, Flash method) in our study to verifying the results from PA technique.

typically probes the surface layer of perovskite materials. [47] Thus, electronic parameters obtained by the two-photon excitation technique and electronic characterization, such as transient photovoltaic (TPV) and IS measurements, were adopted here for comparison. It was observed that the D and τ of $MAPbBr_3$ and $MAPbI_3$ obtained from the PA technique were comparable to those of previous reports and the experimental results in our work. Regarding the value of S, average values of 2200 cm/s and 4000 cm/s were estimated from the PA technique for $MAPbBr_3$

and $MAPbI_3$ single crystals without any surface passivation, respectively. Taking the individuality of single crystals into consideration, we have demonstrated the accuracy of our experimental results based on the values reported in other studies. Simultaneously, the D_{th} measured by the PA technique was consistent with those values produced using the flash method and frequency domain thermoreflectance measurement. [27]

Table 2. The reported values of the electronic and thermal properties of $MAPbBr_3$ and $MAPbI_3$ single crystals derived from different methods. (The data marked with asterisk denote the experimental results from SCLC, IS and Flash method in our study.)

Single crystal	Method	D (cm^2/s)	Method	S (cm/s)	Method	τ (μs)	Method	D_{th} (cm^2/s)
$MAPbBr_3$	SCLC	7.3*	TRS	3400 [8]	IS	70*	Flash	0.0036*
		0.9 [5]	1p/2p	4 [7]	2p	4.5 [7]	FDTR	0.0035 [27]
		0.6 [16]		30 [41]				
		2.2 [42]		6700 [6]				
	Hall	1 [5]	PC	1680 [43]				
	ToF	3 [5]						
$MAPbI_3$	SCLC	8.4*	1p/2p	6000 [41]	IS	133*	Flash	0.0021*
		1.7 [16]		3600 [6]		84 [44]	FDTR	0.0026 [27]
		4.2 [17]	TRS	2800 [9]		163 [20]		
		0.065 [5]				95 [17]		
		4.3 [19]			TPV	82 [17]		
	TRMC	3 [45]			TRMC	15 [18]		
	THz	15.6 [46]						
	ToF	0.6 [17]						
	Hall	2.7 [17]						

Method columns list the techniques used to determine the transport parameters. (SCLC, space charge limit current; Hall, hall effect measurement; ToF, time-of-flight; TRMC, time-resolved microwave conductivity; THz, multi-THz; TRS, transient reflection spectroscopy; 1p, one-photon excitation technique; 2p, two-photon excitation technique; PC, photoconductivity method; IS, impedance spectroscopy; TPV, transient photovoltaic; Flash, the flash method; FDTR, frequency domain thermoreflectance measurement.)

3.5 Conclusion

In summary, we have simultaneously obtained the fundamental characteristics of $MAPbBr_3$ and $MAPbI_3$ single crystals using PA measurements under RDC mode and TDC mode. The thermal and carrier transport contributions to the PA signal can be controlled by the frequency modulation of the excitation light. Using the fitting program we developed, the sample thickness, surface recombination velocity, photoexcited carrier lifetime, carrier diffusivity, and thermal diffusivity can be obtained. We confirmed that these results measured from the PA technique are consistent with those obtained using other techniques, such as the step profiler, SCLC, IS, and flash methods. This demonstrates that the PA technique is a powerful method that can simultaneously and nondestructively evaluate the optical, thermal, and electronic properties of MHP materials. Thus, it can be applied to the evaluation of such properties of different kinds of MHP materials and supply important information for achieving the high performance of MHP-based solar cells.

3.6 Bibliography

1. Snaith, H. J., Perovskites: The Emergence of a New Era for Low-Cost, High-Efficiency Solar Cells. *J. Phys. Chem. Lett.* **2013,** *4* (21), 3623-3630.

2. Zhu, H.; Fu, Y.; Meng, F.; Wu, X.; Gong, Z.; Ding, Q.; Gustafsson, M. V.; Trinh, M. T.; Jin, S.; Zhu, X. Y., Lead halide perovskite nanowire lasers with low lasing thresholds and high quality factors. *Nat. Mater.* **2015,** *14* (6), 636-42.

3. Haeger, T.; Heiderhoff, R.; Riedl, T., Thermal properties of metal-halide perovskites. *J. Mater. Chem. C* **2020,** *8* (41), 14289-14311.

4. He, Y.; Galli, G., Perovskites for Solar Thermoelectric Applications: A First Principle Study of CH3NH3AI3 (A = Pb and Sn). *Chem. Mater.* **2014,** *26* (18), 5394-5400.

5. Shi, D.; Adinolfi, V.; Comin, R.; Yuan, M.; Alarousu, E.; Buin, A.; Chen, Y.; Hoogland, S.; Rothenberger, A.; Katsiev, K.; Losovyj, Y.; Zhang, X.; Dowben, P. A.; Mohammed, O. F.; Sargent, E. H.; Bakr, O. M., Low trap-state density and long carrier diffusion in organolead trihalide perovskite single crystals. *Science* **2015,** *347* (6221), 519-22.

6. Wu, B.; Nguyen, H. T.; Ku, Z.; Han, G.; Giovanni, D.; Mathews, N.; Fan, H. J.; Sum, T. C., Discerning the Surface and Bulk Recombination Kinetics of Organic-Inorganic Halide Perovskite Single Crystals. *Adv. Energy Mater.* **2016,** *6* (14).

7. Fang, H. H.; Adjokatse, S.; Wei, H.; Yang, J.; Blake, G. R.; Huang, J.; Even, J.; Loi, M. A., Ultrahigh sensitivity of methylammonium lead tribromide perovskite single crystals to environmental gases. *Sci. Adv.* **2016,** *2* (7), e1600534.

8. Yang, Y.; Yan, Y.; Yang, M.; Choi, S.; Zhu, K.; Luther, J. M.; Beard, M. C., Low surface recombination velocity in solution-grown CH3NH3PbBr3 perovskite single crystal. *Nat. Commun.* **2015,** *6*, 7961.

9. Yang, Y.; Yang, M.; Moore, David T.; Yan, Y.; Miller, Elisa M.; Zhu, K.; Beard, Matthew C., Top and bottom surfaces limit carrier lifetime in lead iodide perovskite films. *Nat. Energy* **2017,** *2* (2).

10. Sum, T. C.; Mathews, N.; Xing, G.; Lim, S. S.; Chong, W. K.; Giovanni, D.; Dewi, H. A., Spectral Features and Charge Dynamics of Lead Halide Perovskites: Origins and Interpretations. *Acc. Chem. Res.* **2016,** *49* (2), 294-302.

11. Guo, Z.; Manser, J. S.; Wan, Y.; Kamat, P. V.; Huang, L., Spatial and temporal imaging of long-range charge transport in perovskite thin films by ultrafast microscopy. *Nat. Commun.* **2015,** *6*, 7471.

12. Stranks, S. D.; Eperon, G. E.; Grancini, G.; Menelaou, C.; Alcocer, M. J.; Leijtens, T.; Herz, L. M.; Petrozza, A.; Snaith, H. J., Electron-hole diffusion lengths exceeding 1 micrometer in an organometal trihalide perovskite absorber. *Science* **2013,** *342* (6156), 341-4.

13. Xing, G.; Mathews, N.; Sun, S.; Lim, S. S.; Lam, Y. M.; Gratzel, M.; Mhaisalkar, S.; Sum, T. C., Long-range balanced electron- and hole-transport lengths in organic-inorganic CH3NH3PbI3. *Science* **2013,** *342* (6156), 344-7.

14. Tian, W.; Zhao, C.; Leng, J.; Cui, R.; Jin, S., Visualizing Carrier Diffusion in Individual Single-Crystal Organolead Halide Perovskite Nanowires and Nanoplates. *J. Am. Chem. Soc.* **2015,** *137* (39), 12458-61.

15. Wehrenfennig, C.; Liu, M.; Snaith, H. J.; Johnston, M. B.; Herz, L. M., Charge-carrier dynamics in vapour-deposited films of the organolead halide perovskite CH3NH3PbI3−xClx. *Energy Environ. Sci.* **2014,** *7* (7), 2269-2275.

16. Saidaminov, M. I.; Abdelhady, A. L.; Murali, B.; Alarousu, E.; Burlakov, V. M.; Peng, W.; Dursun, I.; Wang, L.; He, Y.; Maculan, G.; Goriely, A.; Wu, T.; Mohammed, O. F.; Bakr, O. M., High-quality bulk hybrid perovskite single crystals within minutes by inverse temperature crystallization. *Nat. Commun.* **2015,** *6*, 7586.

17. Dong, Q.; Fang, Y.; Shao, Y.; Mulligan, P.; Qiu, J.; Cao, L.; Huang, J., Electron-hole diffusion lengths > 175 mum in solution-grown CH3NH3PbI3 single crystals. *Science* **2015,** *347* (6225), 967-70.

18. Bi, Y.; Hutter, E. M.; Fang, Y.; Dong, Q.; Huang, J.; Savenije, T. J., Charge Carrier Lifetimes Exceeding 15 mus in Methylammonium Lead Iodide Single Crystals. *J. Phys. Chem. Lett.* **2016,** *7* (5), 923-8.

19. Lian, Z.; Yan, Q.; Gao, T.; Ding, J.; Lv, Q.; Ning, C.; Li, Q.; Sun, J. L., Perovskite CH3NH3PbI3(Cl) Single Crystals: Rapid Solution Growth, Unparalleled Crystalline Quality, and Low Trap Density toward 10(8) cm(-3). *J. Am. Chem. Soc.* **2016,** *138* (30), 9409-12.

20. Zhang, F.; Yang, B.; Mao, X.; Yang, R.; Jiang, L.; Li, Y.; Xiong, J.; Yang, Y.; He, R.; Deng, W.; Han, K., Perovskite CH3NH3PbI3-xBrx Single Crystals with Charge-Carrier Lifetimes Exceeding 260 mus. *ACS Appl. Mater. Interfaces* **2017,** *9* (17), 14827-14832.

21. Xie, H.; Hao, S.; Bao, J.; Slade, T. J.; Snyder, G. J.; Wolverton, C.; Kanatzidis, M. G., All-Inorganic Halide Perovskites as Potential Thermoelectric Materials: Dynamic Cation off-Centering Induces Ultralow Thermal Conductivity. *J. Am. Chem. Soc.* **2020,** *142* (20), 9553-9563.

22. Pisoni, A.; Jacimovic, J.; Barisic, O. S.; Spina, M.; Gaal, R.; Forro, L.; Horvath, E., Ultra-Low Thermal Conductivity in Organic-Inorganic Hybrid Perovskite CH3NH3PbI3. *J. Phys. Chem. Lett.* **2014,** *5* (14), 2488-92.

23. Lee, W.; Li, H.; Wong, A. B.; Zhang, D.; Lai, M.; Yu, Y.; Kong, Q.; Lin, E.; Urban, J. J.; Grossman, J. C.; Yang, P., Ultralow thermal conductivity in all-inorganic halide perovskites. *Proc. Natl. Acad. Sci. U.S.A.* **2017,** *114* (33), 8693-8697.

24. Xie, H.; Su, X.; Zhang, X.; Hao, S.; Bailey, T. P.; Stoumpos, C. C.; Douvalis, A. P.; Hu, X.; Wolverton, C.; Dravid, V. P.; Uher, C.; Tang, X.; Kanatzidis, M. G., Origin of

Intrinsically Low Thermal Conductivity in Talnakhite Cu17.6Fe17.6S32 Thermoelectric Material: Correlations between Lattice Dynamics and Thermal Transport. *J. Am. Chem. Soc.* **2019,** *141* (27), 10905-10914.

25. Heiderhoff, R.; Haeger, T.; Pourdavoud, N.; Hu, T.; Al-Khafaji, M.; Mayer, A.; Chen, Y.; Scheer, H.-C.; Riedl, T., Thermal Conductivity of Methylammonium Lead Halide Perovskite Single Crystals and Thin Films: A Comparative Study. *J. Phys. Chem. C* **2017,** *121* (51), 28306-28311.

26. Altes, A.; Heiderhoff, R.; Balk, L. J., Quantitative dynamic near-field microscopy of thermal conductivity. *J. Phys. D* **2004,** *37* (6), 952-963.

27. Elbaz, G. A.; Ong, W. L.; Doud, E. A.; Kim, P.; Paley, D. W.; Roy, X.; Malen, J. A., Phonon Speed, Not Scattering, Differentiates Thermal Transport in Lead Halide Perovskites. *Nano Lett.* **2017,** *17* (9), 5734-5739.

28. Yi, N.; Wang, S.; Duan, Z.; Wang, K.; Song, Q.; Xiao, S., Tailoring the Performances of Lead Halide Perovskite Devices with Electron-Beam Irradiation. *Adv. Mater.* **2017,** *29* (34).

29. Shen, Q.; Toyoda, T., Photoacoustic characterization of thermal and electronic transport properties of CdInGaS4 in a transmission detection configuration. *Jpn. J. Appl.* **2000,** *39* (5b), 3164-3168.

30. Bernal-Alvarado, J.; Vargas, M.; Alvarado-Gil, J. J.; Delgadillo, I.; Cruz-Orea, A.; Vargas, H.; Tufiño-Velázquez, M.; Albor-Aguilera, M. L.; González-Trujillo, M. A., Photoacoustic determination of recombination parameters in CdTe/glass system. *J. Appl. Phys.* **1998,** *83* (7), 3807-3810.

31. Dramicanin, M. D.; Nikolic, P. M.; Ristovski, Z. D.; Vasiljevic, D. G.; Todorovic, D. M., Photoacoustic investigation of transport in semiconductors: Theoretical and experimental study of a Ge single crystal. *Phys. Rev., B Condens. Matter* **1995,** *51* (20), 14226-14232.

32. Yamada, Y.; Yamada, T.; Phuong le, Q.; Maruyama, N.; Nishimura, H.; Wakamiya, A.; Murata, Y.; Kanemitsu, Y., Dynamic Optical Properties of CH(3)NH(3)PbI(3) Single Crystals As Revealed by One- and Two-Photon Excited Photoluminescence Measurements. *J. Am. Chem. Soc.* **2015,** *137* (33), 10456-9.

33. Rosencwaig, A.; Gersho, A., Theory of the photoacoustic effect with solids. *J. Appl. Phys.* **1976,** *47* (1), 64-69.

34. Zhang, F.; Song, J.; Zhang, L.; Niu, F.; Hao, Y.; Zeng, P.; Niu, H.; Huang, J.; Lian, J., Film-through large perovskite grains formation via a combination of sequential thermal and solvent treatment. *J. Mater. Chem. A* **2016,** *4* (22), 8554-8561.

35. Deng, Y. H.; Yang, Z. Q.; Ma, R. M., Growth of centimeter-scale perovskite single-crystalline thin film via surface engineering. *Nano Converg.* **2020,** *7* (1), 25.

36. Liu, Y.; Zhang, Y.; Yang, Z.; Yang, D.; Ren, X.; Pang, L.; Liu, S. F., Thinness- and Shape-Controlled Growth for Ultrathin Single-Crystalline Perovskite Wafers for Mass Production of Superior Photoelectronic Devices. *Adv. Mater.* **2016,** *28* (41), 9204-9209.

37. Mannino, G.; Deretzis, I.; Smecca, E.; La Magna, A.; Alberti, A.; Ceratti, D.; Cahen, D., Temperature-Dependent Optical Band Gap in CsPbBr3, MAPbBr3, and FAPbBr3 Single Crystals. *J. Phys. Chem. Lett.* **2020,** *11* (7), 2490-2496.

38. Parker, W. J.; Jenkins, R. J.; Butler, C. P.; Abbott, G. L., Flash Method of Determining Thermal Diffusivity, Heat Capacity, and Thermal Conductivity. *J. Appl. Phys.* **1961,** *32* (9), 1679-1684.

39. Leighton, P. A., Electronic Processes in Ionic Crystals (Mott, N. F.; Gurney, R. W.). *J. Chem. Educ.* **1941,** *18* (5), 249.

40. Poglitsch, A.; Weber, D., Dynamic disorder in methylammoniumtrihalogenoplumbates (II) observed by millimeter-wave spectroscopy. *J. Chem. Phys.* **1987,** *87* (11), 6373-6378.

41. Ščajev, P.; Miasojedovas, S.; Juršėnas, S., A carrier density dependent diffusion coefficient, recombination rate and diffusion length in MAPbI3 and MAPbBr3 crystals measured under one- and two-photon excitations. *J. Mater. Chem. C* **2020,** *8* (30), 10290-10301.

42. Liu, Y.; Zhang, Y.; Yang, Z.; Feng, J.; Xu, Z.; Li, Q.; Hu, M.; Ye, H.; Zhang, X.; Liu, M.; Zhao, K.; Liu, S., Low-temperature-gradient crystallization for multi-inch high-quality perovskite single crystals for record performance photodetectors. *Mater. Today* **2019,** *22*, 67-75.

43. Wei, H.; Fang, Y.; Mulligan, P.; Chuirazzi, W.; Fang, H.-H.; Wang, C.; Ecker, B. R.; Gao, Y.; Loi, M. A.; Cao, L.; Huang, J., Sensitive X-ray detectors made of methylammonium lead tribromide perovskite single crystals. *Nat. Photonics* **2016,** *10* (5), 333-339.

44. Chen, Y. X.; Ge, Q. Q.; Shi, Y.; Liu, J.; Xue, D. J.; Ma, J. Y.; Ding, J.; Yan, H. J.; Hu, J. S.; Wan, L. J., General Space-Confined On-Substrate Fabrication of Thickness-Adjustable Hybrid Perovskite Single-Crystalline Thin Films. *J. Am. Chem. Soc.* **2016,** *138* (50), 16196-16199.

45. Semonin, O. E.; Elbaz, G. A.; Straus, D. B.; Hull, T. D.; Paley, D. W.; van der Zande, A. M.; Hone, J. C.; Kymissis, I.; Kagan, C. R.; Roy, X.; Owen, J. S., Limits of Carrier Diffusion in n-Type and p-Type CH3NH3PbI3 Perovskite Single Crystals. *J. Phys. Chem. Lett.* **2016,** *7* (17), 3510-8.

46. Valverde-Chávez, D. A.; Ponseca, C. S.; Stoumpos, C. C.; Yartsev, A.; Kanatzidis, M. G.; Sundström, V.; Cooke, D. G., Intrinsic femtosecond charge generation dynamics in single crystal CH3NH3PbI3. *Energy Environ. Sci.* **2015,** *8* (12), 3700-3707.

47. Stavrakas, C.; Delport, G.; Zhumekenov, A. A.; Anaya, M.; Chahbazian, R.; Bakr, O. M.; Barnard, E. S.; Stranks, S. D., Visualizing Buried Local Carrier Diffusion in Halide Perovskite Crystals via Two-Photon Microscopy. *ACS Energy Lett.* **2020,** *5* (1), 117-123.

Chapter 4. Photoexcited Carrier Dynamics in Iodine-Doped $CH_3NH_3PbBr_3$ Single Crystals

4.1 Introduction

In recent years, there has been increasing interest in metal halide perovskite (MHP) material ABX_3 (A= formamidinium (FA^+), methylammonium (MA^+), Cs^+; B=Pb^{2+}, Sn^{2+}; X=Cl^-, Br^-, I^-) [1, 2]. The family of MHP exhibits an attractive feature of bandgap tunability, which makes it widely applicable in the field of optoelectronic devices such as light-emitting diodes (LED) [3] and multijunction solar cells [4]. Although the X site (such as I and Br) alloyed MHP can achieve an optimal bandgap of top-cell in a tandem device with silicon about 1.7 eV-1.8 eV [5], the versatility of the halide composition can lead to the notorious phase segregation phenomenon [6], causing severe open-circuit voltage (V_{oc}) losses in the photovoltaic applications [7]. To date, substantial research attention has been devoted to understanding the mechanism of phase segregation. Michael D. McGehee., et al. proposed that the phase segregation originated from halide migration, resulting in a formation of low-bandgap iodine-rich domain [8]. Wright, Adam D., et al. reported the temperature and excitation intensity-dependent phase segregation process [9]. Meanwhile, the mitigating techniques were also explored to stabilize the phase. On one hand, some researchers noted that the enhanced crystallinity and reduced trap states density can profoundly help to reduce the halide segregation [7, 10, 11]. On the other hand, modifying the stoichiometry of A-site cations in perovskite structure is also deemed as an effective approach[11]. Despite extensive studies were conducted on the X-site alloyed MHP materials, the majority of them were focused on the halide segregation dynamics and device optimization [12, 13]. Compared with these features, the studies on the photoexcited carrier dynamics were considerably limited, despite being very critical to

understand the intrinsic properties of MHP. Rehman, Waqaas, et al. studied the charge carrier dynamics of $FAPb(Br_yI_{1-y})_3$ film, and obtained the correlation between the recombination rate constant (bimolecular and Auger recombination) and Br/I fraction [14]. Xiao, Zijie, et al. investigated the carrier recombination dynamics of $MAPb(Br_{1-y}I_y)_3$ single crystals by time-resolved photoluminescence (TRPL) and time-resolved microwave photoconductivity (TRMC) measurement, disclosing the relationship between the Br/I fraction and the electron and hole trapping density [15].

Most of the aforementioned studies were based on the bromide incorporated $APbI_3$, due to the suitable bandgap for optoelectronic devices, while the partial substitution of iodine into the bromine sites in $APbBr_3$ system were less mentioned. Sujith, P. and coworkers elaborated the decrease of defect density with iodine doping in $CsPbBr_3$ single crystals [16]. Atourki, Lahoucine, et al. illustrated a great thermal and atmospheric stability in $CsPbBr_{3-x}I_x$ ($0 \leq x \leq 1$) thin film [17]. These studies indicated that the $APbBr_3$ system incorporated with iodine is highly worth investigating.

The MHP single crystals exhibit diminished defect states, absence of grain boundaries in comparison to their counterpart polycrystalline films, provide a promising platform for investigating the fundamental characteristics of MHP materials [18, 19]. In this article, the photoexcited carrier dynamics of the typical MHP system, iodine-doped $MAPbBr_3$ single crystals have been studied using the excitation intensity-dependent steady state photoluminescence (PL) and TRPL measurements. From X-ray diffraction (XRD), optical absorption and steady state PL spectra, we confirmed the incorporation of iodine content and focused our study on the mixed phase (Br/I). In TRPL measurements, we observed the PL kinetics of these crystals first became faster, then slower, and then faster again, with the increase of iodine component. Interestingly, the PL effective lifetime of the crystal initially shortens upon the addition of iodine and then prolongs,

matching well with the results of estimated trap state density which was conducted by monitoring the PL intensity as a function of excitation intensity. Further, we have clarified the free carrier recombination was dominant in the emission process based on the excitation intensity-dependent PL. According to the excitation intensity-dependent TRPL, we observed a trap filling process followed by free carrier relaxation process in each crystal. Additionally, combined with 2-demensional (2D) contour PL map measurements, we confirmed that both the carrier diffusion and relaxation processes existed in our MHP single crystals. Quantitatively, we obtained the diffusion coefficient and carrier recombination constants (electron, hole monomolecular, bimolecular recombination) by means of numerical simulations. Subsequently, we have obtained the conclusion that the introduction of iodine into $MAPbBr_3$ single crystals increased the trap state density, and with further iodine doping, the trap states gradually reduced. Furthermore, we speculate that the electron detrap process caused by shallow trap states has a significant impact on PL decays. Our results can help to understand the carrier recombination process in iodine-doped $MAPbBr_3$ single crystals and offer a fundamental knowledge for the application of MHP materials.

4.2 Experimental Section

4.2.1 Chemicals and Reagents

Lead bromide ($PbBr_2$) (≥98%), N, N-dimethylformamide (DMF) (anhydrous, 99.8%), and γ-butyrolactone (GBL) (ReagentPlus, ≥99%) were purchased from Sigma Aldrich. Lead iodide (PbI_2) (99.99%) was purchased from High Purity Chemicals. Phosphinic acid (50%) (H_3PO_2) and methylammonium iodide (MAI) were purchased from Fujifilm Wako Pure Chemical Corporation. Methylammonium bromide (MABr) was synthesized following a literature procedure [20]. All salts and solvents were used as received without any further purification.

4.2.2 Synthesis of $MAPb(Br_{1-x}I_x)_3$ Single Crystals

As shown in Fig.4-1, equimolar MABr and $PbBr_2$ was dissolved in DMF to prepare a 1M $MAPbBr_3$ precursor solution. Equimolar MAI and PbI_2 was dissolved in GBL to prepare a 1M $MAPbI_3$ precursor ions. The bromide solution was prepared at room temperature, while the iodide solution was prepared at 65 °C. $MAPb(Br_{1-x}I_x)_3$ (x=0, 0.10, 0.20, 0.33) single crystals were grown by mixing the $MAPbBr_3$ and $MAPbI_3$ precursor solution in a ratio of 3/0, 9/1, 4/1, 2/1, respectively. The mixed precursor solutions were set on the hot plate for growing solution. 1%. wt H_3PO_2 was added into $MAPbI_3$ precursor solution to prevent the oxidation of iodide.

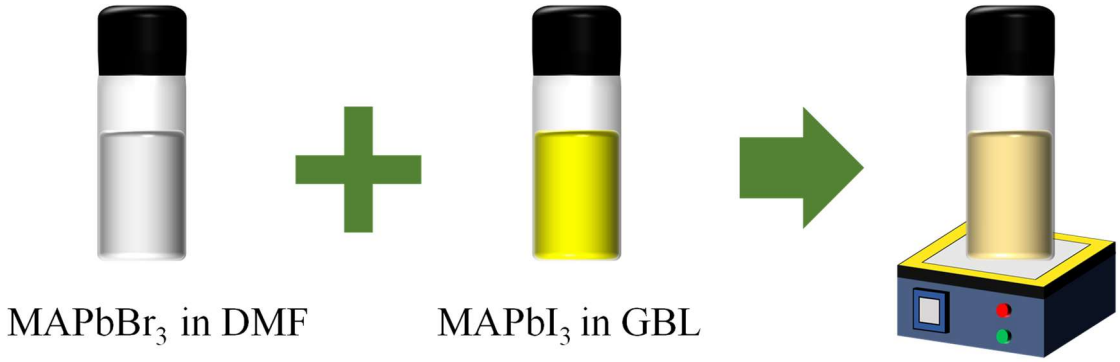

Figure 2-1. The inverse temperature crystallization method to grow $MAPb(Br_{1-x}I_x)_3$ single crystals.

4.2.3 Measurement and Characterization

The XRD and XRC patterns were acquired by the Rigaku Ultima III X-ray diffractometer with monochromatic Cu-Kα irradiation. UV–vis absorption spectra were recorded by a spectrophotometer (V670 JASCO) with an integral sphere mode. Steady state PL, TRPL, and excitation intensity-dependent PL, TRPL were all conducted using the PL system from TOKYO INSTRUMENT, INC. A 473 nm pulsed diode laser (pulse width 90 ps, repetition up to 100MHz, peak power is 4mW) was employed as the excitation source. Excitation intensity was tuned with a circle adjustable neutral density filter. A PMT in conjunction with a TCSPC module was used for PL detection.

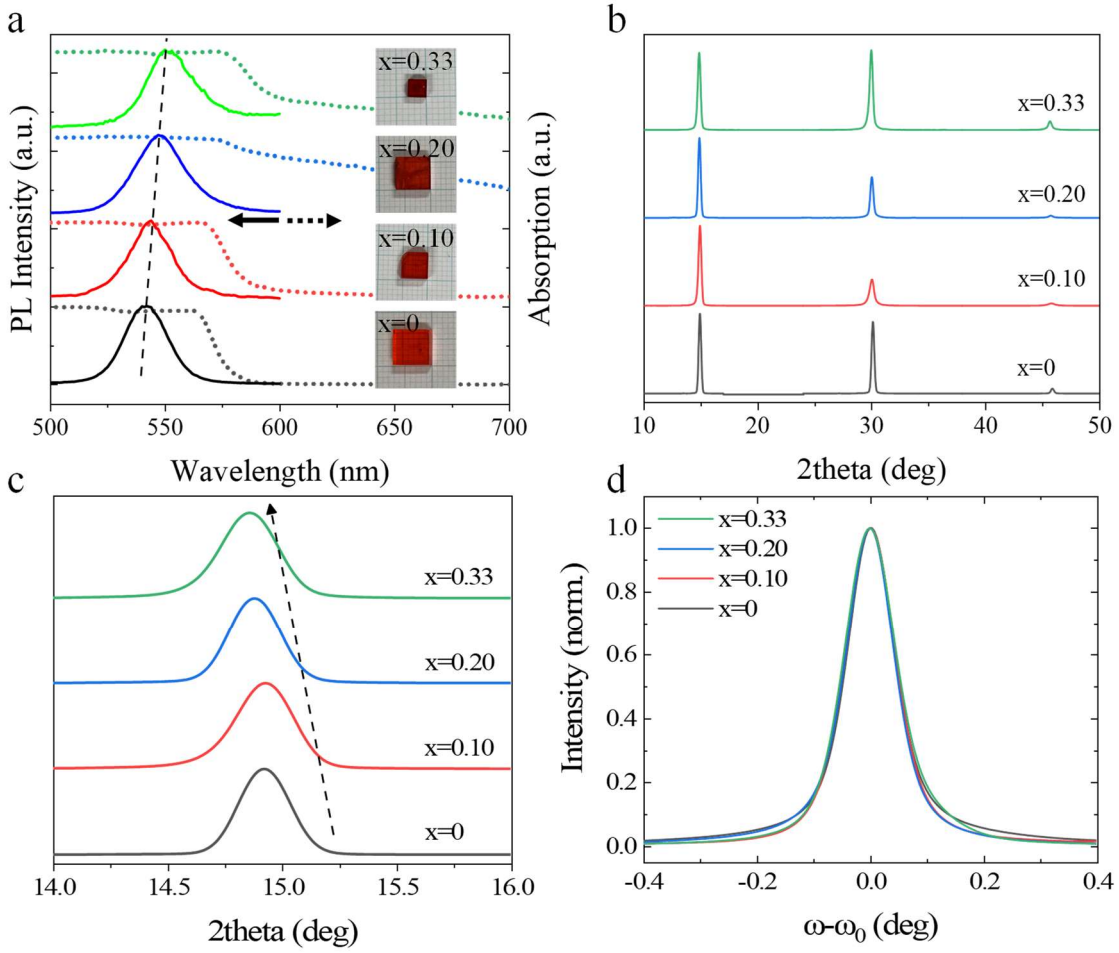

Figure 4-2 (a) UV-vis absorption and PL spectra of four kinds of $MAPb(Br_{1-x}I_x)_3$ single crystals. The inset shows the related pictures of these crystals, (b) X-Ray Diffraction (XRD) pattern of the four kinds of crystals, (c) Enlarged XRD pattern around 15 degrees, (d) X-Ray rocking curve of the crystals.

4.3 Results and discussion

The $MAPb(Br_{1-x}I_x)_3$ single crystals have been synthesized using the inverse temperature crystallization method [21]. By directly mixing the $MAPbBr_3$ and $MAPbI_3$ precursor solution, four kinds of mixed halide perovskite single crystals $MAPb(Br_{1-x}I_x)_3$ (x=0, 0.10, 0.20, 0.33) have been grown. UV-vis absorption and steady-state PL spectra of these single crystals are presented in Fig4-1a, which show a gradual redshift of absorption edges and PL peaks with increasing iodine components. Note that despite many reports observing a small Stokes shift in $MAPbX_3$ (X = Br,

I) single crystals [19], our experimental results still show that all PL peaks are located inside the

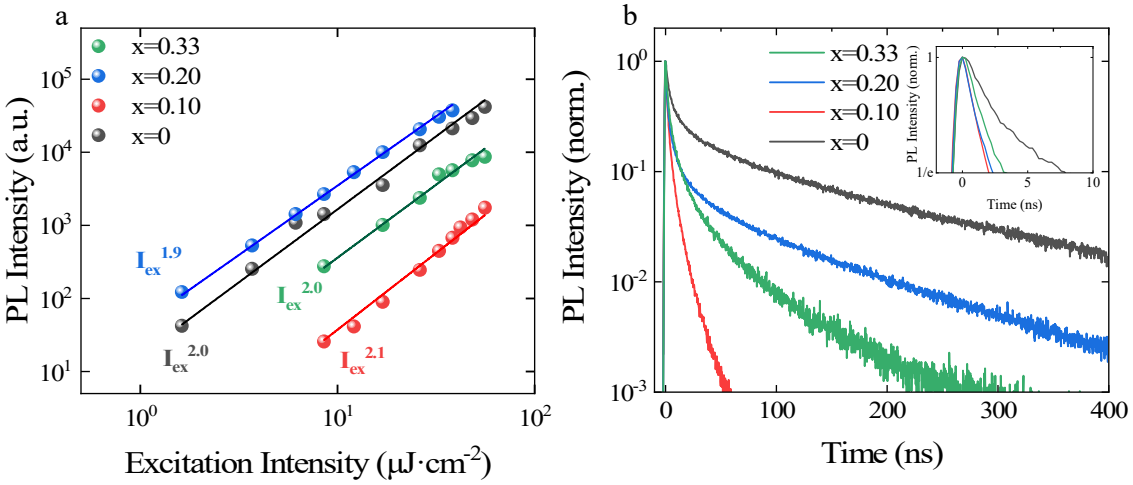

Figure 4-3. (a) PL intensity as a function of excitation intensity for $MAPb(Br_{1-x}I_x)_3$ single crystals. (b) PL decay for these crystals. Inset: enlarged (b) in the range between $I_{PL}(0)$ to $I_{PL}(0)/e$.

corresponding absorption edges. We attributed the phenomenon to the saturation of absorption at short wavelengths due to the large thicknesses of the single crystals [22]. Powder X-Ray diffraction (XRD) patterns of the $MAPb(Br_{1-x}I_x)_3$ crystals are shown in Fig.4-2b, which showed three characteristic diffraction peaks of (100), (200), (300) for the four kinds of crystals, suggesting the similar crystalline structures [23]. As shown in Fig.4-2c, i.e., the enlarged picture of Fig.1b from 14° to 16°, as the x value grows, the (100) diffraction peaks shift to lower angles, which confirmed that the iodine component increased in the crystals as expected. Then, the crystals were further analyzed by X-Ray rocking curve around 14.93° of (100) facet as displayed in Fig.4-2d. The full width of at half maximum (FWHM) of all samples is about 0.10 degree, which is comparable with previous studies [24]. Fig.4-3a summarized the PL intensity (I_{PL}) as a function of the excitation intensity (I_{ex}) of these single crystals. In general, I_{PL} is proportional to the I_{ex}^k, where exponent k is related to the radiative recombination mechanism, with k being approximately equal to 1 for monomolecular recombination and close to 2 for bimolecular

recombination [25]. In our experiment, a square dependence was observed in all four samples, which

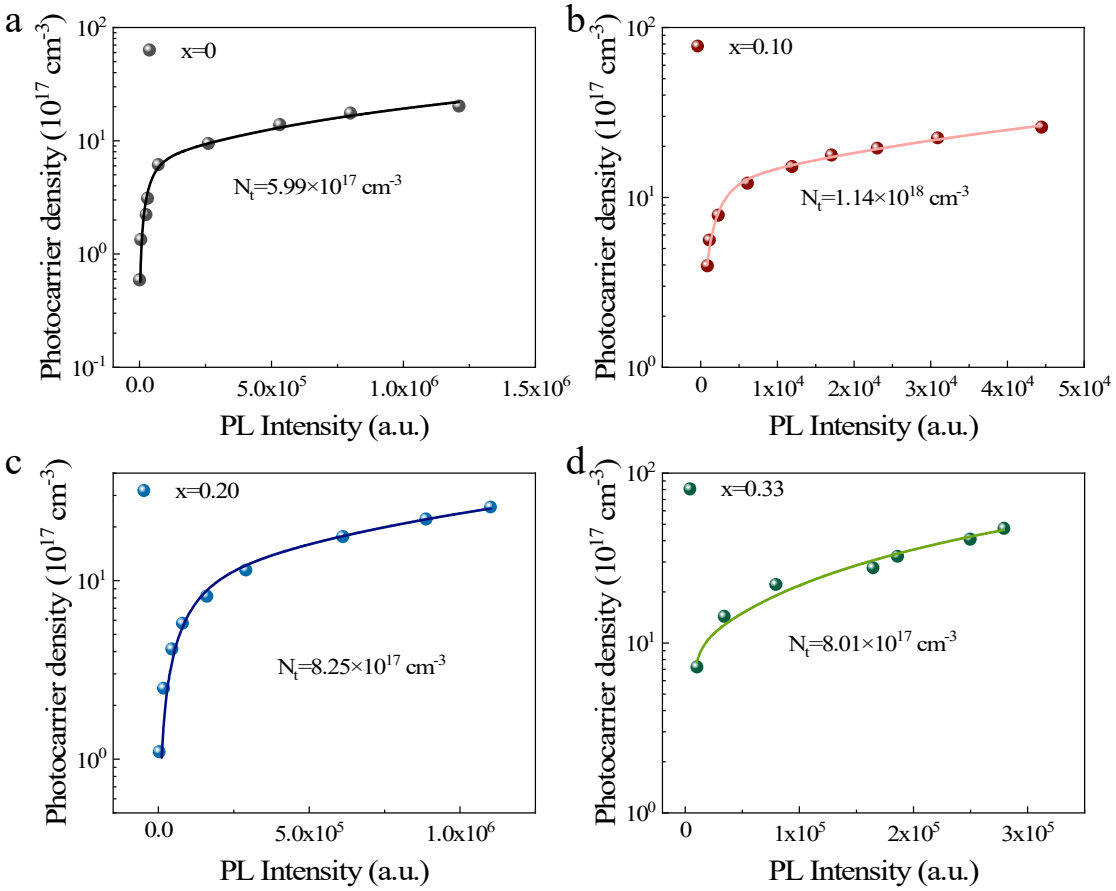

Figure 4-4. Experimental result (dot) of the relationship between the excitation intensity-dependent integrated PL intensity I_{PL} and the initial photocarrier density n(0) for the single crystal with (a)x=0, (b)x=0.10, (c)x=0.20, (d)x=0.33 and the fitting result (line) of the experimental data to Eq.4-1.

can be attributed to the band-to-band radiative recombination originated from the free electrons and holes [26]. TRPL measurements have been conducted for further understanding the carrier recombination process. As shown in Fig.4-3b, we noticed the decay of PL kinetics became faster once adding the iodine content. Diverging from other researches, we observed that the PL decay kinetics didn't vary monotonically with the increase of iodine [15]. Instead, the PL kinetics becomes faster at x=0.10, slows down at x=0.20, and then becomes faster again at x=0.33. We summarized the effective lifetime τ_e extracted from the inset of Fig.4-3b of these crystals in

Fig.4-5. Interestingly, we observed that the addition of iodine leads to a reduction of τ_e.

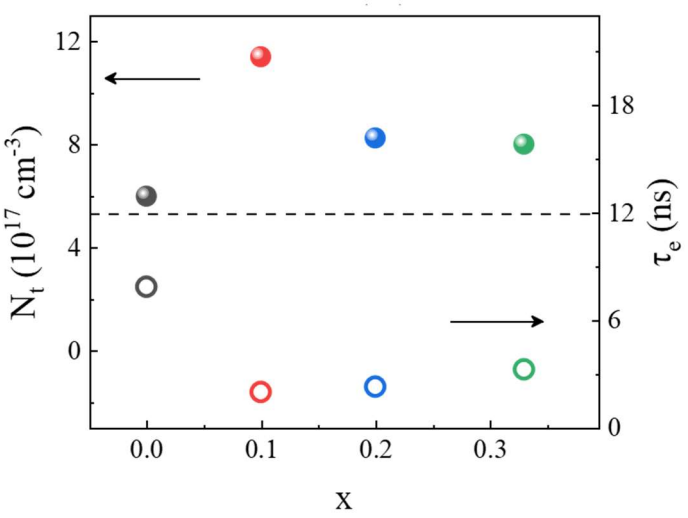

Figure 4-5. Summary of trap state density and effective lifetime for the $MAPb(Br_{1-x}I_x)_3$ single crystals for different x.

However, incorporating additional iodine doping enhanced the τ_e. Due to the early-stage fast decay being attributed to trap-assisted non-radiative recombination [27], the few iodine doping (x=0.10) causes intense trap-assisted non-radiative recombination, and as iodine increases (x=0.20, 0.33), this recombination gradually gets suppressed. To verify this statement, we estimated the trap state density of each sample using excitation intensity-dependent PL measurements. Based on the semiconductor band-edge recombination model [28, 29], the trap density N_t can be determined with the formula:

$$n(0) = N_t\left(1 - e^{-\frac{\alpha\tau_0 I_{PL}}{k}}\right) + \frac{I_{PL}}{k} \qquad (4-1)$$

where $n(0)$ is the initial photoexcited carrier density which can be calculated from the excitation light intensity, τ_0 is the effective PL lifetime, k is a constant, α is the product of the trap capture cross section and the carrier velocity, and I_{PL} is the integrated PL intensity. Fig. 4-4 shows the relationship of $n(0)$ and I_{PL} at a wavelength of 473 nm for the samples. Then, we can obtain the trap state density N_t by fitting the experimental result with Eq. 4-1. The values of the trap state density N_t of our samples were around 10^{17} cm^{-3}, which is in agreement with the literature

reports [29, 30]. We summarized the results of trap state density into Fig.4-5 and found that the trend of the change of the trap state density as x matched well with the changes of effective lifetimes extracted from the inset of Fig.4-3b as mentioned above, indicating that the iodine doping in bromine-based single crystal will form a state with more trap states, which can be gradually alleviated as iodine continues to increase.

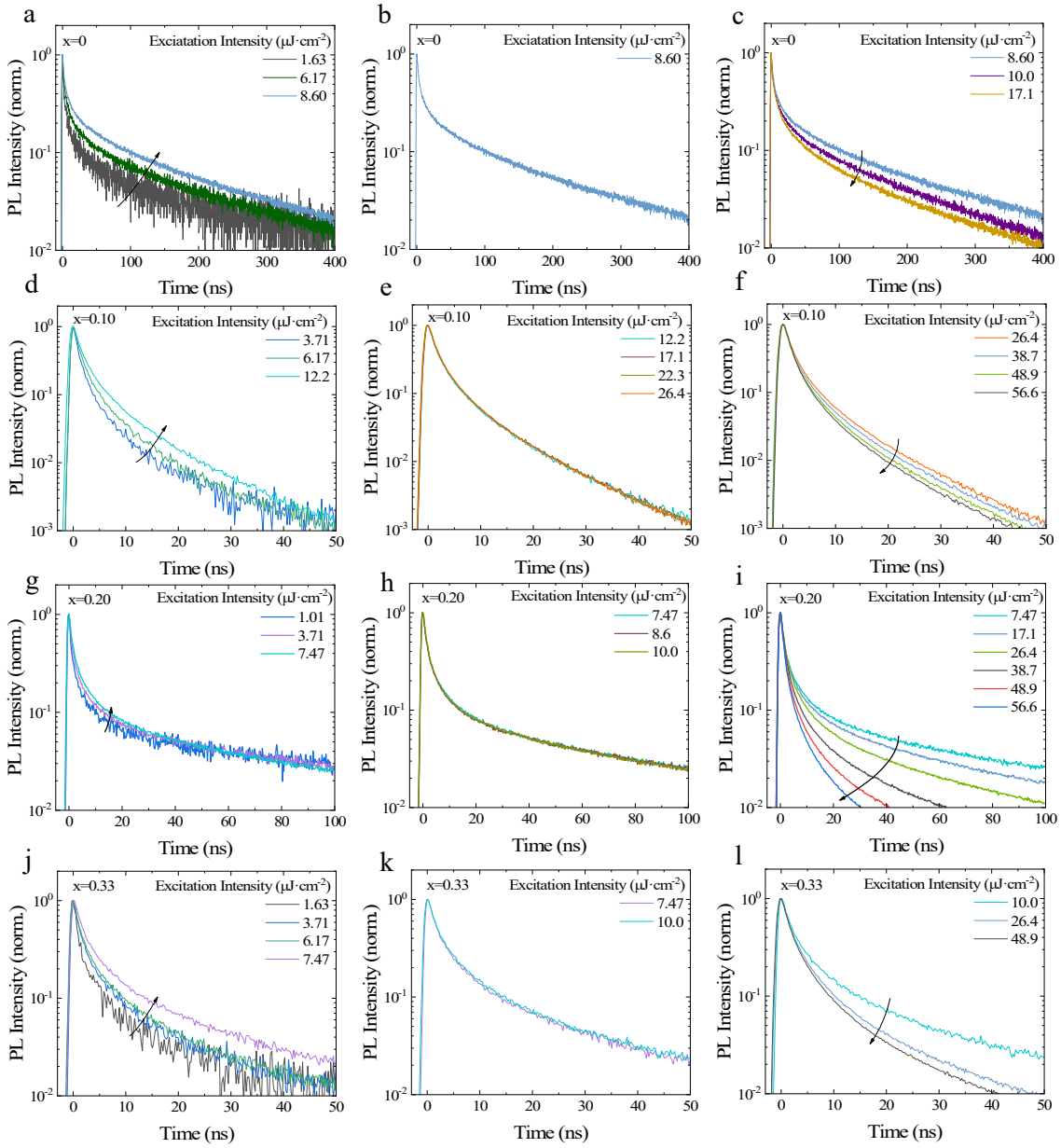

Figure 4-6. Excitation intensity-dependent PL decay curves of (a)(b)(c) x=0, (d)(e)(f) x=0.10, (g)(h)(i) x=0.20, (j)(k)(l) x=0.33 single crystals.

To achieve a deeper understanding of carrier dynamics of $MAPb(Br_{1-x}I_x)_3$ crystals, we implemented the TRPL measurements under different excitation intensity. The results were presented in Fig.4-6. The PL kinetics became slower first, then remained unchanged, and then finally turned faster with the increased excitation intensity. We remarked the evolutionary trend occurred at all samples. Generally, the excitation intensity-dependent PL kinetics can be explained using a rate equation [26]:

$$\frac{dn}{dt} = -An - Bn^2 \qquad (4-2)$$

$$I_{PL} \propto Bn^2 + BnN \qquad (4-3)$$

where n is the photoexcited carrier (electron and hole) density, A is the carrier trapping rate covering the electron and hole trapping rate, B represents the electron-hole radiative recombination rate, and N is the intrinsic carrier density. According to the carrier recombination mechanism, PL kinetics were independent of the excitation intensity under weak excitation conditions, where monomolecular recombination is dominant, while radiative bimolecular recombination is dominant at high excitation intensities, resulting in a fast PL decay as the excitation intensity increase [26]. Take x=0.20 as an example, evidently, the free carrier relaxation theory is consistent with our experiment results above 7.47μJ·cm^{-2}, as shown in Fig.4-6h, i. Below the 7.47μJ·cm^{-2} in Fig.4-6g, the PL kinetics was still sensitive to the excitation intensity here. This was deemed to be a filling process of a fraction of trap states as increased excitation intensity, which prompted the prolonged PL lifetimes [31, 32]. However, the rate Eq. 4-2 can't fit our data very well. Then, we paid attention to our PL decay curves and found that contrasted with the reports of the polycrystalline thin film [25, 31], the fast decay at early time in our samples didn't follow the monoexponential law. It demonstrated that the fast decays may also involve other carrier relaxation processes besides trap-assisted recombination [22]. Meanwhile, we found that beginning part of the fast decays (less than 5 ns) was almost the same and independent of the excitation

intensity as shown in Fig.4-6c,f,i,l. In our experiment, the PL kinetics were excited at 473nm, the light can only penetrate into the sample less than 1 μm, but our sample is very thick (~1mm). Therefore, not only can photoinduced carriers be captured and relaxed by trap states, but they can also diffuse into the interior of the crystal [33]. Relying on this fact, it is reasonable to speculate that there existed a diffusion process in our samples, which can affect the PL kinetics at early-time.

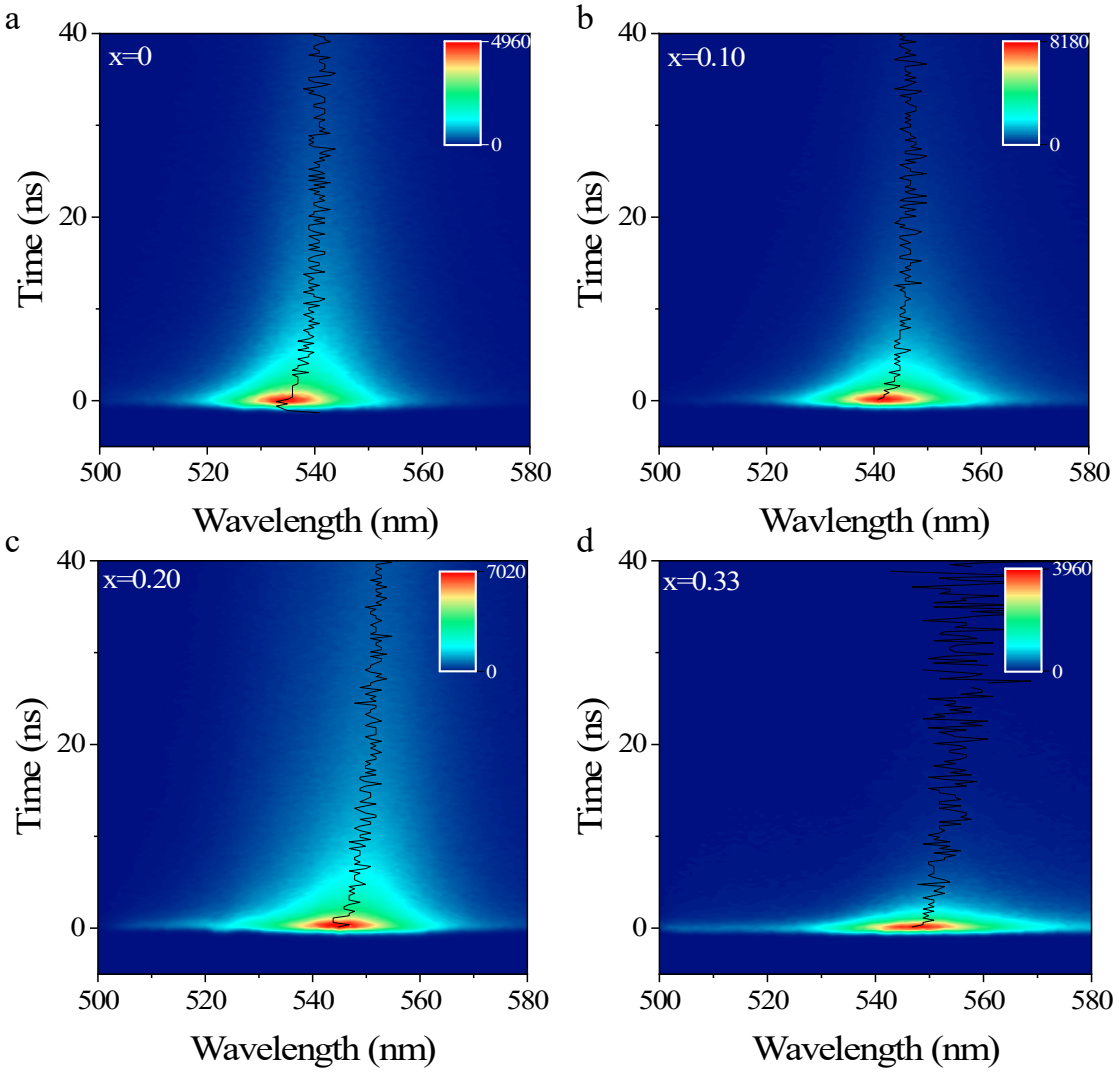

Figure 4-7. 2D contour PL plots of for (a) x=0, (b) x=0.10, (c) x=0.20, (d) x=0.33 single crystal, the black curve represents the shift of peak center position.

Besides, the 2D pseudo-color plot of TRPL of these single crystals was shown in Fig.4-7 to confirm the existence of the carrier diffusion process at the early time. We can clearly observe a

distinct redshift of emission peak in first 10 ns from approximately 543nm to 548nm, which is consistent with the literature reports of carrier diffusion from surface to bulk in single crystals [22, 34]. Since the photocarriers moved into the crystals, a portion of the emitted light with short wavelength will be absorbed by the thick crystals due to the reabsorption effect [35]. Stemming from the above analysis, to understand the meaning of different recombination processes, we were attempting to obtain the recombination constants in different crystals. Under the conditions of neglecting the auger recombination [17], we adopted the rate equations proposed by Wenger and coworkers to conduct a simulation with our experiment data [22] as follows,

$$\frac{\partial n(x,t)}{dt} = G - D_n \frac{\partial^2 n(x,t)}{x^2} - k_e n(x,t) - k_{eh} n^2(x,t) \qquad (4-4)$$

$$\frac{\partial p(x,t)}{dt} = G - D_p \frac{\partial^2 p(x,t)}{x^2} - k_h p(x,t) - k_{eh} p^2(x,t) \qquad (4-5)$$

$$I_{PL}(t) \propto \int n(x,t) \cdot p(x,t) dx \qquad (4-6)$$

Here, G is the photocarrier generation rate, D_n, D_p represent the diffusion coefficient of electron and hole respectively, k_e, k_h the monomolecular non-radiative recombination rate of electron and hole, respectively, and k_{eh} is the bimolecular radiative recombination rate. Regarding the setting of initial conditions in the simulation process, we defined n_0 as the initial photocarrier density at the sample surface (x=0), and δ as the optical penetration depth. The initial photocarrier density can be expressed as the following equation:

$$n(x,0) = p(x,0) = n_0 e^{-\frac{x}{\delta}} \qquad (4-7)$$

Furthermore, the optical penetration depths δ of these crystals at the wavelength of 473nm were estimated from the absorption coefficient referred to the literature reports [6]. Note that, despite the Eq. 4-4, 4-5, 4-6 addressing the impact of both electrons and holes on PL kinetics, the difference between electrons and holes was hard to elaborate. In $MAPbBr_3$ single crystals, the electron trapping is considered to be greater than that of holes, as reported by Wenger, Bernard,

et al. [22]. Taking this prerequisite condition into consideration, we adjusted the electron monomolecular recombination constant to be larger than that of holes for the simulation. And because diffusing charge carriers were affected by trap states [36], diffusion coefficient of electrons was expected to be smaller than that of holes. Under the assumptions mentioned above, we simulated the PL kinetics. As we anticipated, the simulated curves matched well with the

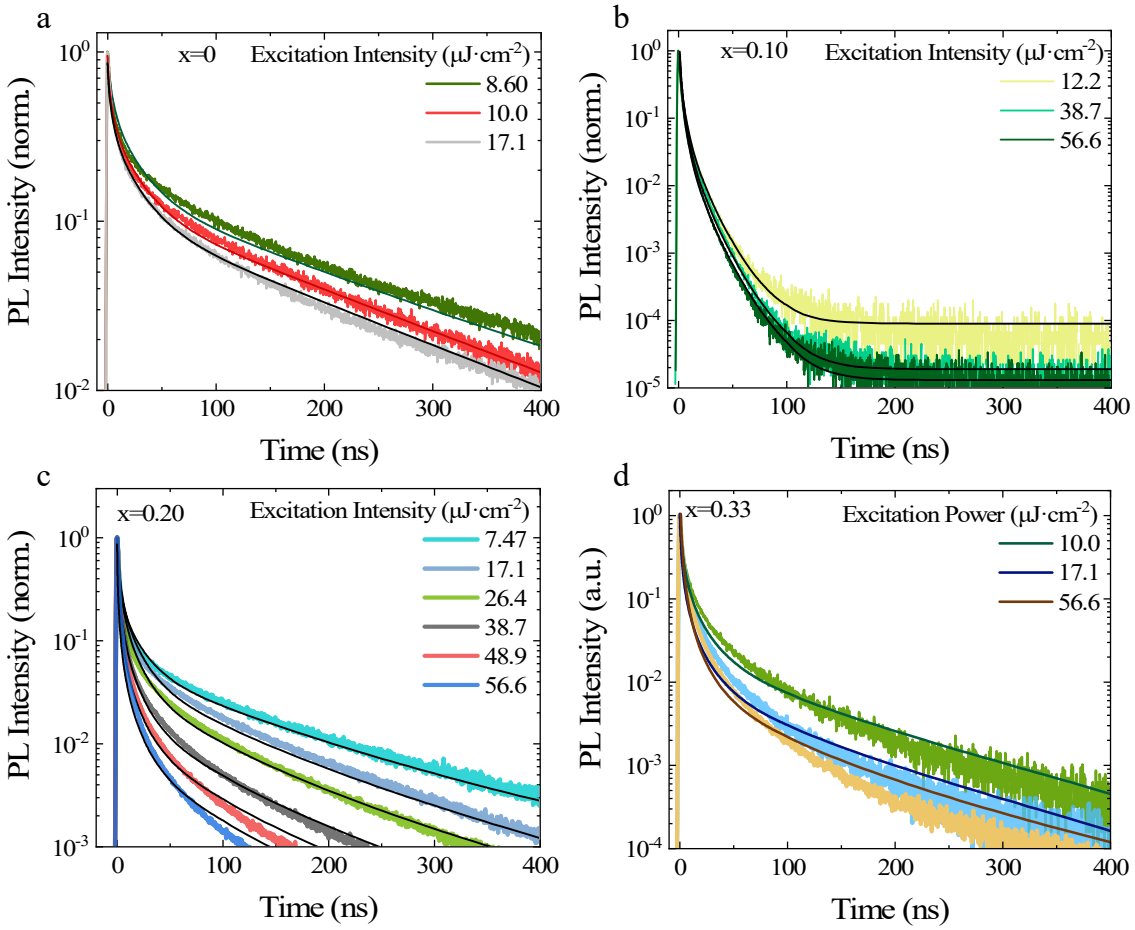

Figure 4-8. Numerical simulations for PL decays extracted from Fig. 4-6. (a) show the x=0, (b) show the x=0.10, (c) show the x=0.20, (d) show the x=0.33 single crystals.

experiment results as shown in Fig.4-8. The simulation parameters including electron, hole diffusion coefficient D_n, D_p, electron, hole monomolecular recombination constant k_e, k_h, and bimolecular recombination constant k_{eh}, were summarized in Table. 1. It is evident that the k_e obtained from these crystals correlated closely with the previously estimated trend of changes in

trap state density, while the k_h was hardly changed with the doped iodine. D_n and D_p also show relatively small changes, possibly due to the limited amount of iodine incorporated, resulting in a minor impact on the overall diffusion of photoexcited carriers. Different from the change of k_e or k_h, the parameter k_{eh} was firstly increase (x=0.10), followed by a decrease (x=0.20), and then increased again (x=0.33), which matched well with the change of PL decays in Fig.4-3b. The bimolecular radiative recombination coefficient typically governs the slow component in the decay process, and we speculate that the anomalous phenomenon is caused by the detrap process of shallow trap states, resulting in an emission on longer timescales [37].

Table 1. The numerical simulation parameters for MAPb($Br_{1-x}I_x$)$_3$ single crystals det (Fig.4-8).

	D_n/cm^2·s^{-1}	D_p/cm^2·s^{-1}	$k_e\times10^6$/s^{-1}	$k_h\times10^6$/s^{-1}	$k_{eh}\times10^{-9}$/cm^3·s^{-1}
x=0	1.03	2.57	2.6	0.1	0.35
x=0.10	1.03	2.31	22	0.1	45
x=0.20	1.54	2.95	2.5	0.1	3.5
x=0.33	1.03	2.57	2.2	0.1	9.0

It is commonly acknowledged that the formation of trap state has a significant impact on carrier recombination in perovskite. Understanding the formation of trap states can offer guidance in elucidating the PL kinetics in our experiment. Generally, most trap states can be termed as shallow or deep states depending on the energy difference between trap states and band-edge states, both of which were harmful to carrier transport. However, there was also a small fraction of trap states that were harmless, for example, the trap state levels were situated above the conduction band (CB) or below the valence band (VB) edge [38]. According to Shi, Dong, et al., a high formation energy of the deep trap state of $MAPbBr_3$ was predicted from the Density Functional Theory (DFT) calculation under Br-rich environment [39]. Consequently, in our experiment, the formation of shallow trap states in the $MAPbBr_3$ crystals exerted a considerable impact on the PL kinetics. Referring to the study of the formation of trap states in the $MAPbBr_3$, shallow trap states like V_{Pb}, Pb_{MA}, and V_{Br} were more likely to form [40], where V_{Pb} acts as the hole

trap, and Pb_{MA}, V_{Br} functions as electron traps. In the case of the iodine alloyed $MAPbBr_3$ system, when a small amount of iodine content was added into the $MAPbBr_3$ crystal, new trap states (e.g., V_I) were introduced, leading to enhanced electron capture. From the acquired simulation parameters, the hole trap was attributed to the V_{Pb} trap level in our experiment, due to the slight fluctuation of the trap energy level with the incorporation of iodine [40]. Regarding the electron trapping process, Pb_{MA}, V_{Br}, and V_I contributed significantly to the k_e. According to the literature from Mannodi-Kanakkithodi, Arun and coworkers [40], it can be inferred that in the $MAPb(Br_{1-x}I_x)_3$ system, as x changes from 0.25 to 0.5, the shallow trap states of V_{Br} and V_I became closer to the bottom of the conduction band, leading to a short-lived lifetime [41]. We regarded that the changes in the shallow trap states mentioned above influence the electronic detrap processes, which can explain the phenomenon observed in the PL decays in Fig.4-3.

4.4 Conclusion

In conclusion, we synthesized the $MAPb(Br_{1-x}I_x)_3$ (x=0, 0.10, 0.20, 0.33) perovskite single crystals, and investigated their carrier recombination dynamics using the TRPL technique. We determined that the free carrier recombination is dominant in our crystals from excitation intensity-dependent PL measurement. Based on the TRPL measurements, we found that the PL kinetics became rapid, then slowed down, and finally get rapid again with the iodine doping. Interestingly, we have also observed that the PL effective lifetime of the crystal get shorter when iodine is introduced, but gradually becomes longer with further doping, which is attributed to the impact of trap-assisted recombination. To validate this, we measured the trap state density of these crystals and found the changes of trap state density matched well with the variation of PL effective lifetimes. Then, excitation intensity-dependent TRPL measurements have been conducted for further investigating the carrier dynamics, where we confirmed the diffusion processes existed in our PL kinetics. 2D contour PL plot measurement provided additional evidence supporting our

assumption of carrier diffusion. After, we obtained the diffusion coefficient and carrier recombination constants by numerical simulations, from which we have confirmed that when a few iodine is doped, the trap state density in crystal increases rapidly, while further doping gradually reduces the trap state density. Additionally, according to the change trend in the bimolecular recombination constant, we speculated that the electron detrap process induced by shallow trap states influences the slow component in PL decays, explaining the phenomenon where PL kinetics altered from slow to fast upon iodine doping (x from 0.20 to 0.33). Our results have deepened the understanding of MHP materials and provided guidance for their practical applications.

4.5 Bibliography

1. Green, M. A.; Ho-Baillie, A.; Snaith, H. J., The emergence of perovskite solar cells. *Nat. Photonics* **2014,** *8* (7), 506-514.

2. Brenner, T. M.; Egger, D. A.; Kronik, L.; Hodes, G.; Cahen, D., Hybrid organic—inorganic perovskites: low-cost semiconductors with intriguing charge-transport properties. *Nature Reviews Materials* **2016,** *1* (1).

3. Tan, Z. K.; Moghaddam, R. S.; Lai, M. L.; Docampo, P.; Higler, R.; Deschler, F.; Price, M.; Sadhanala, A.; Pazos, L. M.; Credgington, D.; Hanusch, F.; Bein, T.; Snaith, H. J.; Friend, R. H., Bright light-emitting diodes based on organometal halide perovskite. *Nat Nanotechnol* **2014,** *9* (9), 687-92.

4. Beal, R. E.; Slotcavage, D. J.; Leijtens, T.; Bowring, A. R.; Belisle, R. A.; Nguyen, W. H.; Burkhard, G. F.; Hoke, E. T.; McGehee, M. D., Cesium Lead Halide Perovskites with Improved Stability for Tandem Solar Cells. *J Phys Chem Lett* **2016,** *7* (5), 746-51.

5. Longo, G.; Momblona, C.; La-Placa, M.-G.; Gil-Escrig, L.; Sessolo, M.; Bolink, H. J., Fully Vacuum-Processed Wide Band Gap Mixed-Halide Perovskite Solar Cells. *ACS Energy Lett.* **2017,** *3* (1), 214-219.

6. Hoke, E. T.; Slotcavage, D. J.; Dohner, E. R.; Bowring, A. R.; Karunadasa, H. I.; McGehee, M. D., Reversible photo-induced trap formation in mixed-halide hybrid perovskites for photovoltaics. *Chem Sci* **2015,** *6* (1), 613-617.

7. Mahesh, S.; Ball, J. M.; Oliver, R. D. J.; McMeekin, D. P.; Nayak, P. K.; Johnston, M. B.; Snaith, H. J., Revealing the origin of voltage loss in mixed-halide perovskite solar cells. *Energy & Environmental Science* **2020,** *13* (1), 258-267.

8. Brennan, M. C.; Draguta, S.; Kamat, P. V.; Kuno, M., Light-Induced Anion Phase Segregation in Mixed Halide Perovskites. *ACS Energy Lett.* **2017,** *3* (1), 204-213.

9. Wright, A. D.; Patel, J. B.; Johnston, M. B.; Herz, L. M., Temperature-Dependent Reversal of Phase Segregation in Mixed-Halide Perovskites. *Adv Mater* **2023,** *35* (19), e2210834.

10. Zhou, Y.; Jia, Y. H.; Fang, H. H.; Loi, M. A.; Xie, F. Y.; Gong, L.; Qin, M. C.; Lu, X. H.; Wong, C. P.; Zhao, N., Composition-Tuned Wide Bandgap Perovskites: From Grain Engineering to Stability and Performance Improvement. *Adv. Funct. Mater.* **2018,** *28* (35).

11. Herz, A. J. K. a. L. M., Preventing phase segregation in mixed-halide perovskites: a perspective. *Energy Environ. Sci.* **2020,** *13*, 2024-2046.

12. Colella, S.; Mosconi, E.; Fedeli, P.; Listorti, A.; Gazza, F.; Orlandi, F.; Ferro, P.; Besagni, T.; Rizzo, A.; Calestani, G.; Gigli, G.; De Angelis, F.; Mosca, R., MAPbI3-xClx Mixed Halide Perovskite for Hybrid Solar Cells: The Role of Chloride as Dopant on the Transport and Structural Properties. *Chem. Mater.* **2013,** *25* (22), 4613-4618.

13. David P. McMeekin, G. S., Waqaas Rehman, Giles E. Eperon, Michael Saliba, Maximilian T. Hörantner, Amir Haghighirad, Nobuya Sakai, Lars Korte, Bernd Rech, Michael B. Johnston, Laura M. Herz, Henry J. Snaith, A mixed-cation lead mixed-halide perovskite absorber for tandem solar cells. *Science* **2016,** *351* (6269), 151-155.

14. Rehman, W.; Milot, R. L.; Eperon, G. E.; Wehrenfennig, C.; Boland, J. L.; Snaith, H. J.; Johnston, M. B.; Herz, L. M., Charge-Carrier Dynamics and Mobilities in Formamidinium Lead Mixed-Halide Perovskites. *Adv Mater* **2015,** *27* (48), 7938-44.

15. Xiao, Z.; Tao, T.; Shu, J.; Dang, W.; Pan, S.; Zhang, W., Charge Carrier Recombination Dynamics in MAPb(Br1−yIy)3 Single Crystals. *Crystals* **2022,** *12* (10).

16. Sujith, P.; Parne, S. R.; Predeep, P., Iodine doping of CsPbBr3: toward highly stable and clean perovskite single crystals for optoelectronic applications. *Philosophical Magazine* **2023,** *103* (13), 1213-1231.

17. Johnston, M. B.; Herz, L. M., Hybrid Perovskites for Photovoltaics: Charge-Carrier Recombination, Diffusion, and Radiative Efficiencies. *Acc Chem Res* **2016,** *49* (1), 146-54.

18. Dong, Q.; Fang, Y.; Shao, Y.; Mulligan, P.; Qiu, J.; Cao, L.; Huang, J., Electron-hole diffusion lengths > 175 mum in solution-grown CH3NH3PbI3 single crystals. *Science* **2015,** *347* (6225), 967-70.

19. Yamada, Y.; Yamada, T.; Phuong le, Q.; Maruyama, N.; Nishimura, H.; Wakamiya, A.; Murata, Y.; Kanemitsu, Y., Dynamic Optical Properties of CH(3)NH(3)PbI(3) Single Crystals As Revealed by One- and Two-Photon Excited Photoluminescence Measurements. *J. Am. Chem. Soc.* **2015,** *137* (33), 10456-9.

20. Zhang, F.; Song, J.; Zhang, L.; Niu, F.; Hao, Y.; Zeng, P.; Niu, H.; Huang, J.; Lian, J., Film-through large perovskite grains formation via a combination of sequential thermal and solvent treatment. *J. Mater. Chem. A* **2016,** *4* (22), 8554-8561.

21. Saidaminov, M. I.; Abdelhady, A. L.; Maculan, G.; Bakr, O. M., Retrograde solubility of formamidinium and methylammonium lead halide perovskites enabling rapid single crystal growth. *Chem Commun (Camb)* **2015,** *51* (100), 17658-61.

22. Wenger, B.; Nayak, P. K.; Wen, X.; Kesava, S. V.; Noel, N. K.; Snaith, H. J., Consolidation of the optoelectronic properties of CH(3)NH(3)PbBr(3) perovskite single crystals. *Nat Commun* **2017,** *8* (1), 590.

23. Zhang, F.; Yang, B.; Mao, X.; Yang, R.; Jiang, L.; Li, Y.; Xiong, J.; Yang, Y.; He, R.; Deng, W.; Han, K., Perovskite CH3NH3PbI3-xBrx Single Crystals with Charge-Carrier Lifetimes Exceeding 260 mus. *ACS Appl. Mater. Interfaces* **2017,** *9* (17), 14827-14832.

24. Liu, Y.; Zhang, Y.; Yang, Z.; Feng, J.; Xu, Z.; Li, Q.; Hu, M.; Ye, H.; Zhang, X.; Liu, M.; Zhao, K.; Liu, S., Low-temperature-gradient crystallization for multi-inch high-

quality perovskite single crystals for record performance photodetectors. *Mater. Today* **2019,** *22*, 67-75.

25. Fang, H. H.; Protesescu, L.; Balazs, D. M.; Adjokatse, S.; Kovalenko, M. V.; Loi, M. A., Exciton Recombination in Formamidinium Lead Triiodide: Nanocrystals versus Thin Films. *Small* **2017,** *13* (32).

26. Yamada, Y.; Nakamura, T.; Endo, M.; Wakamiya, A.; Kanemitsu, Y., Photocarrier recombination dynamics in perovskite CH3NH3PbI3 for solar cell applications. *J Am Chem Soc* **2014,** *136* (33), 11610-3.

27. Wu, Z.; Jiang, M.; Liu, Z.; Jamshaid, A.; Ono, L. K.; Qi, Y., Highly Efficient Perovskite Solar Cells Enabled by Multiple Ligand Passivation. *Adv. Energy Mater.* **2020,** *10* (10).

28. Xing, G.; Mathews, N.; Lim, S. S.; Yantara, N.; Liu, X.; Sabba, D.; Gratzel, M.; Mhaisalkar, S.; Sum, T. C., Low-temperature solution-processed wavelength-tunable perovskites for lasing. *Nat Mater* **2014,** *13* (5), 476-80.

29. Shi, J.; Zhang, H.; Li, Y.; Jasieniak, J. J.; Li, Y.; Wu, H.; Luo, Y.; Li, D.; Meng, Q., Identification of high-temperature exciton states and their phase-dependent trapping behaviour in lead halide perovskites. *Energy & Environmental Science* **2018,** *11* (6), 1460-1469.

30. Wu, B.; Nguyen, H. T.; Ku, Z.; Han, G.; Giovanni, D.; Mathews, N.; Fan, H. J.; Sum, T. C., Discerning the Surface and Bulk Recombination Kinetics of Organic-Inorganic Halide Perovskite Single Crystals. *Adv. Energy Mater.* **2016,** *6* (14).

31. Yamada, Y.; Endo, M.; Wakamiya, A.; Kanemitsu, Y., Spontaneous Defect Annihilation in CH3NH3PbI3 Thin Films at Room Temperature Revealed by Time-Resolved Photoluminescence Spectroscopy. *J Phys Chem Lett* **2015,** *6* (3), 482-6.

32. Yamada, T.; Yamada, Y.; Nishimura, H.; Nakaike, Y.; Wakamiya, A.; Murata, Y.; Kanemitsu, Y., Fast Free-Carrier Diffusion in CH3NH3PbBr3 Single Crystals Revealed by Time-Resolved One- and Two-Photon Excitation Photoluminescence Spectroscopy. *Adv. Electron. Mater.* **2016,** *2* (3).

33. Yang, Y.; Yan, Y.; Yang, M.; Choi, S.; Zhu, K.; Luther, J. M.; Beard, M. C., Low surface recombination velocity in solution-grown CH3NH3PbBr3 perovskite single crystal. *Nat. Commun.* **2015,** *6*, 7961.

34. Fang, H. H.; Adjokatse, S.; Wei, H.; Yang, J.; Blake, G. R.; Huang, J.; Even, J.; Loi, M. A., Ultrahigh sensitivity of methylammonium lead tribromide perovskite single crystals to environmental gases. *Sci. Adv.* **2016,** *2* (7), e1600534.

35. Fang, Y.; Wei, H.; Dong, Q.; Huang, J., Quantification of re-absorption and re-emission processes to determine photon recycling efficiency in perovskite single crystals. *Nat Commun* **2017,** *8*, 14417.

36. Gutierrez Alvarez, S.; Lin, W.; Abdellah, M.; Meng, J.; Zidek, K.; Pullerits, T.; Zheng, K., Charge Carrier Diffusion Dynamics in Multisized Quaternary Alkylammonium-Capped CsPbBr(3) Perovskite Nanocrystal Solids. *ACS Appl Mater Interfaces* **2021,** *13* (37), 44742-44750.

37. Vonk, S. J. W.; Fridriksson, M. B.; Hinterding, S. O. M.; Mangnus, M. J. J.; van Swieten, T. P.; Grozema, F. C.; Rabouw, F. T.; van der Stam, W., Trapping and Detrapping in Colloidal Perovskite Nanoplatelets: Elucidation and Prevention of Nonradiative Processes through Chemical Treatment. *J Phys Chem C Nanomater Interfaces* **2020,** *124* (14), 8047-8054.

38. Jin, H.; Debroye, E.; Keshavarz, M.; Scheblykin, I. G.; Roeffaers, M. B. J.; Hofkens, J.; Steele, J. A., It's a trap! On the nature of localised states and charge trapping in lead halide perovskites. *Materials Horizons* **2020,** *7* (2), 397-410.

39. Shi, D.; Adinolfi, V.; Comin, R.; Yuan, M.; Alarousu, E.; Buin, A.; Chen, Y.; Hoogland, S.; Rothenberger, A.; Katsiev, K.; Losovyj, Y.; Zhang, X.; Dowben, P. A.; Mohammed, O. F.; Sargent, E. H.; Bakr, O. M., Low trap-state density and long carrier diffusion in organolead trihalide perovskite single crystals. *Science* **2015,** *347* (6221), 519-22.

40. Mannodi-Kanakkithodi, A.; Park, J.-S.; Martinson, A. B. F.; Chan, M. K. Y., Defect Energetics in Pseudo-Cubic Mixed Halide Lead Perovskites from First-Principles. *The Journal of Physical Chemistry C* **2020,** *124* (31), 16729-16738.

41. Viswanath, A. K., SURFACE AND INTERFACIAL RECOMBINATION IN SEMICONDUCTORS. *Handbook of Surfaces and Interfaces of Materials* **2001,** *1*, 217-284.

Chapter 5. Conclusion and Prospective

5.1 Summary

In this thesis, we synthesized single crystals related to $MAPbX_3$ (X=Br, I) and systematically studied their intrinsic physical properties and method techniques, including optical, electronic, thermal, and carrier dynamics, in Chapter 3-4. With typical $MAPbBr_3$ and $MAPbI_3$ single crystals as the research subjects, we innovated in the method techniques of perovskites and used them to characterize the fundamental properties of perovskites. In iodine-doped $MAPbBr_3$ single crystals, the carrier dynamics of their mixed phases were studied, and new phenomena were discovered in the carrier relaxation process with the addition of iodine. Specifically, the new findings of this thesis are listed as following:

In Chapter 3:

1. We attempted to use photoacoustic spectroscopy (PAS) to characterize the optical, electronic, and thermal properties of perovskite single crystals. By comparing with other characterization methods, we found that the PA method can simultaneously and accurately obtain parameters such as the material's optical absorption, surface recombination velocity, carrier diffusion coefficient, carrier lifetime, and thermal diffusivity. Our findings expand the testing techniques for perovskite materials, and we hope this method can be applied to other perovskites, providing fundamental parameters for the fabrication of their devices.

In Chapter 4:

1. From the excitation-intensity dependent PL experiments, we concluded that in iodine-doped $MAPbBr_3$ single crystals, the free carrier recombination is dominant, because the excitation light intensity has a quadratic relationship with the PL intensity.

2. From the excitation-intensity dependent PL and TRPL experiments, we observed that in $MAPb(Br_{1-x}I_x)_3$ single crystals, with the doping of iodine, the effective lifetime of the single crystal first decreases and then increases, matching well with the trap state density values obtained from fitting data. From this, we can infer that a few iodine doping (x=0.10) deteriorates the quality of $MAPbBr_3$ single crystals. Through numerical simulation, we found that the change in the electron trap-assisted recombination is related to the above phenomenon, thereby verifying the above conjecture, and concluding that electron traps play a major role in this system.

3. From the TRPL measurements, we observed that the overall lifetime of the crystal initially decreases, then increases, and finally decreases again with the increase of iodine. Based on these experimental conclusions, we speculate that the detrap process of shallow electron traps affects the slow component of the decay process. The increase of iodine affects the energy level position of shallow traps, and consequently, the lifetime of the detrapped electrons also changes.

5.2 Prospective

Although we have studied the fundamental properties of perovskite single crystals and proposed improvements to their testing techniques, the development of perovskite single crystals still faces many challenges. In our first work, using the PA technique, we successfully obtained various properties simultaneously. This method is based on the study of carrier diffusion and thermal diffusion processes. We anticipate that this method can be applied to other perovskite materials to efficiently obtain these parameters. Although the PA method can obtain surface

recombination parameters of materials, when it comes to already fabricated devices, interfaces, just like the surfaces of materials, have many carrier recombination centers, where the PA technique is hard to measure. For issues like these, the testing techniques for perovskites still need to be continually updated to facilitate more convenient research on their materials and devices. In the case of iodine-doped bromine-based perovskite single crystals, while we have systematically studied their fundamental properties such as carrier dynamics, there are still some aspects that are under-researched. For example, in the bromine-iodine mixed system, phase separation phenomena are difficult to avoid. Although in our research, through methods like PL, optical absorption, and XRD, we found that phase separation is relatively weak, allowing us to focus entirely on the study of the mixed phase. However, our doping ratio only goes up to 0.33. If doping continues, the phase separation phenomena will intensify, making it difficult to study the mixed phase. How to effectively suppress phase separation still requires a lot of research. The resolution of the aforementioned issues can reveal the intrinsic properties of perovskite single crystals. In the future, perovskite single crystals will continue to play an active role in the field of photovoltaics.

List of Publications

Papers

(1) **Dong Liu**, Hua Li, Yusheng Li, Taro Toyoda, Koji Miyazaki, Shuzi Hayase, Chao Ding, and Qing Shen, "Simultaneous Characterization of Optical, Electronic, and Thermal Properties of Perovskite Single Crystals Using a Photoacoustic Technique." *ACS Photonics,* 2023, 10(1), 265-273. (**Chapter 3**)

(2) **Dong Liu**, Chao Ding, Yao Guo, Hua Li, Yusheng Li, Dandan Wang, Yongge Yang, Yuyao Wei, Shikai Chen, Guozheng Shi, Taro Toyoda, Shuzi Hayase and Qing Shen, "Photoexcited Carrier Dynamics in Iodine-Doped $CH_3NH_3PbBr_3$ Single Crystals" [Unpublished] (**Chapter 4**)

(3) Hua Li, Qing Wang, Yusuke Oteki, Chao Ding, **Dong Liu**, Yao Guo, Yusheng Li, Yuyao Wei, Dandan Wang, Yongge Yang, Taizo Masuda, Mengmeng Chen, Zheng Zhang, Tomah Sogabe, Shuzi Hayase, Yoshitaka Okada, Satoshi Iikubo, and Qing Shen, "Enhanced Hot-Phonon Bottleneck Effect on Slowing Hot Carrier Cooling in Metal Halide Perovskite Quantum Dots With Alloyed A-Site.", *Advanced Materials,* 2023, 35, 2301834

(4) Hua Li, Chao Ding, **Dong Liu**, Shota Yajima, Kei Takahashi, Shuzi Hayase and Qing Shen, "Efficient Charge Transfer in MAPbI3 QDs/TiO_2 Heterojunctions for High-Performance Solar Cells." *Nanomaterials,* 2023, 13(7), 1292.

(5) Yuyao Wei, Mako Nakamura, Chao Ding, **Dong Liu**, Hua Li, Yusheng Li, Yongge Yang, Dandan Wang, Ruixiang Wang, Shuzi Hayase, Taizo Masuda, Qing Shen, "Unraveling the Organic and Inorganic Passivation Mechanism of ZnO Nanowires for Construction of Efficient Bulk Heterojunction Quantum Dot Solar Cells", *ACS Applied Materials & Interfaces,* 2022, 14 (31), 36268-36276.

(6) Chao Ding, Dandan Wang, **Dong Liu**, Hua Li, Yusheng Li, Shuzi Hayase, Tomah Sogabe, Taizo Masuda, Yong Zhou, Yingfang Yao, Zhigang Zou, Ruixiang Wang, Qing Shen, "Over 15% Efficiency PbS Quantum-Dot Solar Cells Synergistic Effects of Three Interface Engineering: Reducing Nonradiative Recombination and Balancing Charge Carrier

Extraction", *Advanced Energy Materials*, 2022, 12 (35), 2201676.

(7) Gaurav Kapil, Takeru Bessho, Yoshitaka Sanehira, Shahrir R. Sahamir, Mengmeng Chen, Ajay Kumar Baranwal, **Dong Liu**, Yuya Sono, Daisuke Hirotani, Daishiro Nomura, Kohei Nishimura, Muhammad Akmal Kamarudin, Qing Shen, Hiroshi Segawa, and Shuzi Hayase, "Tin－Lead Perovskite Solar Cells Fabricated on Hole Selective Monolayers." *ACS Energy Letters,* 2022, 7, 3, 966−974.

(8) Ajay Kumar Baranwal, Kohei Nishimura, **Dong Liu**, Muhammad Akmal Kamarudin, Gaurav Kapil, Shrikant Saini, Tomohide Yabuki, Satoshi Iikubo, Takashi Minemoto, Kenji Yoshino, Koji Miyazaki, Qing Shen, and Shuzi Hayase "Relationship between carrier density and precursor solution stirring for lead-free tin halide perovskite solar cells performance." *ACS Applied Energy Materials,* 5(4), 4002-4007.

(9) Liang Wang, Mengmeng Chen, Shuzhang Yang, Namiki Uezono, Qingqing Miao, Gaurav Kapil, Ajay Kumar Baranwal, Yoshitaka Sanehira, Dandan Wang, **Dong Liu**, Tingli Ma, Kenichi Ozawa, Takeaki Sakurai, Zheng Zhang, Qing Shen, and Shuzi Hayase, "SnO_x as Bottom Hole Extraction Layer and Top In Situ Protection Layer Yields over 14% Efficiency in Sn-Based Perovskite Solar Cells." *ACS Energy Letters.* 2022, 7, 10, 3703−3708.

(10) Zheng Zhang, Liang Wang, Ajay Kumar Baranwal, Shahrir Razey Sahamir, Gaurav Kapil, Yoshitaka Sanehira, Muhammad Akmal Kamarudin, Kohei Nishimura, Chao Ding, **Dong Liu**, Yusheng Li, Hua Li, Mengmeng Chen, Qing Shen, Teresa S Ripolles, Juan Bisquert, Shuzi Hayase, "Enhanced efficiency and stability in Sn-based perovskite solar cells by trimethylsilyl halide surface passivation", *Journal of Energy Chemistry*, 2022, 12, 035005.

(11) Zheng Zhang, Ajay Kumar Baranwal, Shahrir Razey Sahamir, Gaurav Kapil, Yoshitaka Sanehira, Mengmeng Chen, Kohei Nishimura, Chao Ding, **Dong Liu**, Hua Li, Yusheng Li, Muhammad Akmal Kamarudin, Qing Shen, Teresa S Ripolles, Juan Bisquert, Shuzi Hayase, "Large Grain Growth and Energy Alignment Optimization by Diethylammonium Iodide Substitution at A Site in Lead-Free Tin Halide Perovskite Solar Cells", *Solar RRL*, 2021, 2, 2100633.

(12) Fei Li, Yang Liu, Guozheng Shi, Wei Chen, Renjun Guo, **Dong Liu**, Yaohong Zhang, Yongjie Wang, Xing Meng, Xuliang Zhang, You Lv, Wei Deng, Qing Zhang, Yao Shi, Yifan Chen, Kai Wang, Qing Shen, Zeke Liu, Peter Müller-Buschbaum, and Wanli Ma, "Matrix Manipulation of Directly-Synthesized PbS Quantum Dot Inks Enabled by Coordination Engineering." *Advanced Functional Materials,* 2021, 31(45), 2104457.

Conference Presentations

(1) **Poster: D. Liu**, C. Ding, Y. Zhang, F. Liu, F. Zhang, T. Toyoda, S. Hayase, Q. Shen, Optical Properties and Photoexcited Carrier Dynamics of Mixed-Halide Perovskite Single Crystals, MRM2021 Materials Research Meeting, 13-17 Dec., 2021, Yokohama, Japan.

(2) **Poster: 劉 東**, 李 花, 李 玉勝, 丁 超, 豊田 太郎, 宮崎 康次, 早瀬 修二, 沈 青, 光音響法によるペロブスカイト単結晶の表面再結合と熱物性の研究, 第69回応用物理学会春季学術講演会, 22-26 Mar., 2022, 青山学院大学, 相模原キャンパス

(3) **Poster: 劉 東**, 李 花, 李 玉勝, 丁 超, 豊田 太郎, 宮崎 康次, 早瀬 修二, 沈 青, 光音響法によるペロブスカイト単結晶の電子物性と熱物性の測定, 第19回「次世代

の太陽光発電システム」シンポジウム（第2回日本太陽光発電学会学術講演会）28-29 Jun., 2022, 金沢市文化ホール

(4) **Oral: 劉 東**, 李 花, 李 玉勝, 丁 超, 豊田 太郎, 宮崎 康次, 早瀬 修二, 沈 青, 光音響法による$MAPbX_3$ (X= Br, I) 単結晶の電子物性と熱物性の研究, 第83回応用物理学会秋季学術講演会, 20-23 Sep., 2022, 東北大学, 川内北キャンパス

(5) **Poster: D. Liu,** H. Li, Y. Li, T. Toyoda, K. Miyazaki, S. Hayase, C. Ding, Q. Shen, Study of Electronic and Thermal Properties of $CH_3NH_3PbX_3$ (X = Br, I) Single Crystals Using Photoacoustic Methods, The 43rd Symposium on UltraSonic Electronics, 7-9 Nov., 2022, 同志社大学 今出川校地, 室町キャンパス寒梅館

(6) **Poster: D. Liu**, H. Li, Y. Li, C. Ding, T. Toyoda, K. Miyazaki, S. Hayase, Q. Shen, Characterization of carrier and thermal transport properties of $CH_3NH_3PbX_3$ (X=Br, I) single crystal using photoacoustic technique, PVSEC-33, International Photovoltaic Science and Engineering Conference, 13-17 Nov, 2022, Nagoya, Japan.

(7) **Poster: 劉 東**, 李 花, 李 玉勝, 豊田 太郎, 早瀬 修二, 丁 超, 沈 青, 鉛錫ペロブスカイト単結晶の光学特性に関する研究, 第70回応用物理学会春季学術講演会, 15-18, Mar., 2023, 上智大学, 四谷キャンパス

Acknowledgements

First of all, I am very grateful to Prof. Shen for giving me the opportunity to study in Japan. Starting from my master's program, it has been almost 5 years now. During this time, Prof. Shen has provided me with a lot of help in both my research and daily life. In terms of research, we often discuss and identify current problems. In daily life, as my "guardian", Prof. Shen helped me apply for scholarships and takes the students from the lab out for meals. The premise of having a very happy and meaningful study abroad experience is due to the opportunity and various kinds of support provided by Prof. Shen, so I am very grateful for this opportunity and the help I have received.

I am also very grateful to the four seniors who were there when I first came to Japan: Professor Zhang Yaohong, Professor Ding Chao, Professor Liu Feng, and Mr. Huang Qingxun. They helped me adapt to life in the lab. Prof. Zhang and Liu, who were postdoctors when I joined the lab. They taught me how to use various instruments during my master's program and offered many valuable suggestions for my research. Mr. Huang, who was a master's student at that time, can speak fluent Japanese, and helped me become more familiar with the Japanese students in the lab. Although Prof. Zhang and Liu, and Mr. Huang, had returned to China before I started my Ph.D. course, I am still grateful for all the things they did to take care of me. When I arrived, Prof. Ding had just completed his Ph.D. program and became a teaching assistant in the lab. Among these seniors, I spent the most time and had the most interactions with him. He guided me through experiments and explained the specific steps in detail. In the publications I completed, besides Prof. Shen, he also made significant contributions. In daily life, he would go out to eat and take walks with me and a few other classmates. He returned to China this January and successfully found a job in a university. While I am happy for his success, I am also very grateful for the contributions he has made to me and the entire laboratory.

I would like to thank Prof. Hayase, Dr. Chen Mengmeng, Dr. Zhang Zheng, Mr. Bi Huan, and Dr. Wang Liang for their help and support on my experiments. I am also thankful for the classmates who studied with me in the lab. Dr. Li Yusheng often proposed interesting ideas and was rigorous in research. Dr. Li Hua was diligent and earnest, continuously exploring unfamiliar fields until becoming an expert in those areas. I am grateful for the example you set, helping me understand the qualities an outstanding researcher should possess. Mr. Yang Yongge, who joined our lab a year later due to the COVID-19 pandemic, has made significant efforts in research. In just a year and a half, he achieved many interesting results. I hope that both of us will have a smooth job finding process. Miss. Wang Dandan and Wei Yuyao, thank you for your contributions in managing lab equipment and guiding students, making the lab more organized and well-regulated. I extend my gratitude to Mr. Chen Shikai, Mr. Zhang Boyu, Miss. Ji Sujun for your support as well as their companionship and assistance in my daily life.

At the same time, I would like to thank the Japanese students I met. This includes my seniors, peers, and juniors during my master's and doctor's degree. Mr. Yasuda, Mr. Yoshida, Miss. Yoshihara, you guided me in familiarizing myself with the equipment and laboratory rules when I first joined the lab. Mr. Asakura, Mr. Oguri, Mr. Matsumoto, Mr. Takahashi, Mr. Houji, thank you for managing the laboratory and providing assistance for my experiments. I would also like to thank a few friends here. Kawabata. Kentaro, you are a reliable friend who helped me with classes and school matters when I was still not proficient in Japanese. You not only took me to participate in basketball club activities but also to watch an NBA game. It was my first time watching a game live, and it was amazing. Nakamura Mako is very serious about experiments, often staying late at school to work on them. She is also patient in chatting with me in Japanese, gradually improving my Japanese language skills. Yajima Shota, as a junior, is very easy to communicate with and enthusiastic. He almost knows everything about the laboratory, so I often

received his help in this regard. Mr. Fuchimoto and Mr. Tosa, very interesting juniors, were also willing to communicate and helped me a lot with laboratory affairs and experimental equipment. I would also like to thank Dr. Zhang Fan, Dr. Shi Guozheng, Prof. Wei Huiyun, and Prof. Guo Yao. I have learned a lot from all of you.

I feel very fortunate to have met all of the above-mentioned people during my study abroad period. I believe this is also a kind of fate.

I would like to express my gratitude to my parents for their support, both spiritually and financially, during my studies abroad. Thank you for your care and encouragement. Additionally, I am very thankful to my brother and sister. It is a luxury to see one's family in a foreign land, so thank you for your care and attention to my life.

Finally, I would like to thank the TONEN INTERNATIONAL SCHOLARSHIP FOUNDATION for financial support of my Ph.D. studies.